UNIVERSIDADE DA BEIRA INTERIOR
Engenharia

# Induced Drag Reduction with a Wing Tip Tail Configuration

(versão corrigida após defesa)

**Henrique Miguel de Almeida**

Dissertação para obtenção do Grau de Mestre em
**Engenharia Aeronáutica**
(Ciclo de estudos integrado)

Orientador: Prof. Doutor Miguel Ângelo Rodrigues Silvestre

**Covilhã, julho de 2018**

# Acknowledgments

I want to express my sincere gratitude to several people that contributed to my work on this thesis.

First, I would like to thank my thesis supervisor, Professor Miguel Ângelo Silvestre, not only for his support during this work but also for all the inspiration and knowledge sharing through my Aeronautical Engineering degree.

To all my friends, colleagues and professors that accompanied me during this journey in the University of Beira Interior.

To my girlfriend, Ana Paiva, for supporting me and encouraging me in my decisions.

To my family for all the support, especially, I have to thank to my parents, José Luís and Sandra, they were the ones who made possible my education, this work and inspired me to seek higher achievements.

# Resumo

Os ensaios em voo são uma das etapas mais delicadas e importantes do desenvolvimento de uma aeronave, é a melhor maneira de provar que uma aeronave, bem como os conceitos de projeto nela implementados, são funcionais. Os UAVs, geralmente mais baratos de construir do que os aviões tripulados, são uma maneira económica e mais segura de desenvolver uma aeronave experimental para testar novos conceitos e validá-los. Na presente dissertação, um novo conceito de configuração de cauda para reduzir o arrasto induzido, onde as superfícies da cauda são colocadas na esteira, nos vórtices de ponta da asa, é experimentalmente testado através de ensaios em voo. A nova configuração é comparada com uma configuração de base convencional, primeiro numericamente com um método de vortex lattice method e, em seguida, através de ensaios em voo da configuração do novo conceito e da convencional. O equipamento de aquisição de dados foi desenvolvido para este trabalho. A metodologia de testes de voo para obter o desempenho da aeronave, baseia-se nas trocas de energia potencial e cinética da aeronave e é também comparada com outras metodologias. Com esta metodologia e após 6.5 horas de dados obtidos com ensaios em voo, o conceito para a redução do arrasto induzido é validado, bem como a metodologia de ensaios em voo baseada nas trocas de energia. Alterações para aumentar o potencial da configuração atual são também sugeridas com base nos resultados do estudo numérico.

# Palavras-chave

UAV, Arrasto Induzido, Wing Tip Tail, Ensaios em Voo, Vórtice de Ponta de Asa

# Abstract

Flight testing is one of the most delicate and important stages of an aircraft development, it is the ultimate way to prove that an aircraft, as well as the design concepts implemented in it are functional. UAVs, being usually cheaper to build than manned aircraft, are a cost effective and safer way to develop an experimental aircraft, in particular to test new concepts and validate them. In the present dissertation, a new tail configuration concept to reduce the induced drag, where the tail surfaces are placed in the wing tip vortices wake, is experimentally tested through flight testing. The new concept configuration is compared with a conventional baseline configuration, first numerically with a vortex lattice method and then through the flight testing of both the new concept configuration and the conventional baseline. The data acquisition equipment was developed for this work. The flight testing methodology to obtain the aircraft performance, is based in the potential and kinetic energy changes of the aircraft and it is also compared with other methodologies. With this methodology and after 6.5 hours of flight testing data, the concept to reduce the induced drag is validated as well as the energy based flight testing methodology. Changes to increase the potential of the present configuration are also suggested based on the results of the numerical study.

# Keywords

UAV, Induced Drag, Wing Tip Tail, Flight Testing, Wing Tip Vortex

# Contents

# List of Figures

# List of Tables

# Nomenclature

| | |
|---|---|
| $AR$ | (Wing) Aspect Ratio |
| $b$ | Wingspan $[m]$ |
| $b'$ | Spanwise Wing Tip Vortex Spacing $[m]$ |
| $\bar{c}$ | Mean Geometric Chord $[m]$ |
| $CAS$ | Calibrated Airspeed $[m/s]$ |
| $C_D$ | Drag Coefficient |
| $c_d$ | Profile Drag Coefficient |
| $C_{D,0}$ | Zero Lift Drag Coefficient |
| $C_{D,e}$ | Parasite Drag Coefficient |
| $C_{Di}$ | Induced Drag Coefficient |
| $C_{D_{min}}$ | Minimum Drag Coefficient |
| $C_L$ | Lift Coefficient |
| $C_{L_{CDmin}}$ | Lift Coefficient for Minimum Drag Coefficient |
| $CG$ | Center of Gravity |
| $D$ | Drag Force $[N]$ |
| $D_i$ | Induced Drag Force $[N]$ |
| $dt$ | Infinitesimal Time $[s]$ |
| $E$ | Total Airplane Energy $[J]$ |
| $e$ | Oswald Factor |
| $e_0$ | Span Efficiency |
| $E_s$ | Specific Energy $[m]$ |
| $F$ | Generic Force $[N]$ |
| $g$ | Gravitational Acceleration $[m/s^2]$ |
| $h$ | Altitude $[m]$ |
| $\dot{h}$ | Altitude Derivative $[m/s]$ |
| $\ddot{h}$ | Altitude Second Derivative $[m/s^2]$ |
| $h_e$ | Energy Height $[m]$ |
| $h_{rel}$ | Relative Altitude $[m]$ |
| $I_{bat}$ | Battery Current Drain $[A]$ |
| $KE$ | Kinetic Energy $[J]$ |

| | |
|---|---|
| $k_i$ | Elliptical induced drag factor |
| $K$ | Induced Drag Factor |
| $L'$ | Lift Force per Unit Span $[N/m]$ |
| $L$ | Lift Force $[N]$ |
| $l_0$ | Integral Scale of Wake Vorticity $[m]$ |
| $L/D$ | Glide Ratio |
| $l_h$ | Horizontal Tail Moment Arm $[m]$ |
| $l_v$ | Vertical Tail Moment Arm $[m]$ |
| $m$ | (Airplane) Mass $[kg]$ |
| $p$ | Static Pressure $[Pa]$ |
| $p_0$ | ISA Mean Sea Level Reference Pressure $[Pa]$ |
| $P_a$ | Available Power $[W]$ |
| $PE$ | Potential Energy $[J]$ |
| $P_e$ | Electrical Power $[W]$ |
| $P_f$ | Field Static Pressure $[Pa]$ |
| $P_r$ | Required Power $[W]$ |
| $P_s$ | Specific Excess Power $[W/N]$ |
| $q$ | Dynamic Pressure $[Pa]$ |
| $R^2$ | Coefficient of Determination |
| $r$ | Parasite Drag Due to Lift Coefficient |
| $RC$ | Rate of Climb $[m/s]$ |
| $r_k$ | Vortex-core Radius $[m]$ |
| $S$ | Reference Wing Area $[m^2]$ |
| $S_h$ | Reference Horizontal Tail Area $[m^2]$ |
| $S_v$ | Reference Vertical Tail Area $[m^2]$ |
| $T$ | Thrust Force $[N]$ |
| $t$ | Time $[s]$ |
| $T_0$ | ISA Mean Sea Level Reference Temperature $[K]$ |
| $T_a$ | Available Thrust $[N]$ |
| $TAS$ | True Airspeed $[m/s]$ |
| $T_f$ | Flying Field Temperature $[K]$ |
| $T_k$ | Temperature (in Kelvin) $[K]$ |

| | |
|---|---|
| $T_r$ | Required Thrust Force $[N]$ |
| $U_{bat}$ | Battery Voltage $[V]$ |
| $V$ | Velocity $[m/s]$ |
| $\dot{V}$ | Velocity Derivative $[m/s^2]$ |
| $V_{AIR}$ | Airspeed $[m/s]$ |
| $V_{GND}$ | Groundspeed $[m/s]$ |
| $V_\infty$ | Relative Wind $[m/s]$ |
| $\bar{V}_h$ | Horizontal Tail Volume Coefficient |
| $\bar{V}_v$ | Vertical Tail Volume Coefficient |
| $W$ | Aircraft Weight Force $[N]$ |

Greek letters:

| | |
|---|---|
| $\alpha_{Tr}$ | Thrust Angle $[rad]$ |
| $\Delta P$ | Differential Pressure $[Pa]$ |
| $\eta_p$ | Propulsive Efficiency |
| $\Gamma$ | Airfoil Circulation $[m^2/s]$ |
| $\Gamma_{wing}$ | Wing Circulation $[m^3/s]$ |
| $\gamma$ | Glide Angle $[rad]$ |
| $\gamma_x$ | Trailing Vortex Strength (Vorticity) in the Longitudinal Axis $[m^2/s]$ |
| $\omega$ | Downwash Velocity $[m/s]$ |
| $\rho$ | Air Density $[kg/m^3]$ |
| $\rho_0$ | ISA Mean Sea Level Reference Air Density $[kg/m^3]$ |
| $\sigma$ | Standard Deviation |
| $\pi$ | Pi Number |
| $\phi$ | Diameter $[mm]$ |

# Acronyms

| | |
|---|---|
| BEC | Battery Eliminator Circuit |
| CFD | Computational Fluid Dynamics |
| CFRP | Carbon Fiber Reinforced Polymer |
| CSV | Comma Separated Values |
| DDL | Drag Due to Lift |
| DLG | Discus Launch Glider |
| ESC | Electronic Speed controller |
| GPS | Global Positioning System |
| ISA | International Standard Atmosphere |
| LiPo | Lithium Polymer |
| LLT | Lifting Line Theory |
| MAC | Mean Aerodynamic Chord |
| NASA | National Aeronautics and Space Administration |
| OHS | Outboard Horizontal Stabilizers |
| PCB | Printed Circuit Board |
| PLA | Polylactic Acid |
| R/C | Radio Controlled |
| UAV | Unmanned Aerial vehicle |
| VLM | Vortex Lattice Method |
| WTT | Wing Tip Tail Configuration |

# Chapter 1

# Introduction

## 1.1 Motivation

The airplane design is in constant development since its creation, the conventional designs are reaching their maximum potential and new concepts for the optimization of flying vehicles are studied. The motivation for the present work comes from the necessity of validating a new airplane configuration concept. Since the aircraft was already developed, improved and built, estimating its performance mainly through flight testing was the chosen solution. There is also a motivation for studying a flight testing methodology, the development and documentation of the currently proposed energy based methodology, will allow the estimation of the performance of present and future projects from the University of Beira Interior (UBI) Aerospace Sciences department and refine the design methodologies created hereon.

Beyond the objectives of this dissertation, the Unmanned Aerial Vehicles represent now a great importance in the aerospace research and industry, this industry is the one in the aeronautical field that in the last years has grown the most. These aircraft have many applications, they are being used as a final product for example for dangerous applications, aerial mapping, or as a test rig to test new concepts and ideas before building a full scale manned aircraft. Being able to contribute with new concepts and testing approaches to the aircraft design field of study, was an important motivation too.

## 1.2 The New Configuration: Wing Tip Tail

The new proposed configuration, called wing tip tail configuration (WTT), to reduce the wing tip vortex generated drag is implemented in a fixed-wing remotely piloted airplane with tail surfaces, a fuselage and an electric motor with a tractor propeller. Apart from the tail surfaces and relatively low aspect ratio wing, which is a result from the limited span requirement for this aircraft design, everything is similar to a conventional fixed-wing airplane of the same size. In this new non-conventional tail configuration two tail surfaces are positioned behind the wing near each of the wingtips, they have a dihedral angle so they are directed upward and inboard. Their spanwise location, vertical position, dihedral angle and distance from wing are design variables. The aircraft is extensively described in Chapter 3.

The concept of the tested aircraft appears in the 2003 design-build-fly Portuguese competition, Figure 1.1, the Air Cargo Challenge (ACC) . Briefly, the Air Cargo Challenge is a design-build-fly type competition for the engineering and science students with the main objective of developing a remotely piloted aircraft that can carry the maximum possible payload within certain specifications, that can be changed each edition held every two years. The University of Beira Interior (UBI) team won this first edition with the present new aircraft configuration.

Despite the first place, this aircraft had a dynamic stability problem, where at a certain airspeed interval, a dutch roll like movement with constant amplitude took place, this problem resulted from the interference of the tail surfaces with the wingtip vortex, when during a sideslip one of the tail surfaces would leave the vortex wake creating an asymmetrical force that forced the aircraft to yaw the other direction creating again the same effect in the other direction repeatedly.

Figure 1.1: UBI's 2003 ACC edition winning airplane.

The aircraft configuration was further studied and improved, in the 2007 ACC edition, Figure 1.2, when the competition became European, with 21 teams from 7 countries, a new aircraft with the same configuration concept reached the 5th place. In this aircraft, the tail surfaces were not at the wingtips but slightly inboard, this way, the aircraft did not show the dynamic stability problem that characterized the previous 2003 ACC airplane. However, due to the wing construction method and materials, the wing was not torsionally stiff. Being the tail surfaces mounted behind the wing at the wingtips, when acting in the long arm elevons tail surfaces to roll the aircraft, the wing twists resulting in an increasing of the angle of incidence at the tips as the dynamic pressure increases, producing a roll control reversal beyond a given airspeed, that can result in a crash.

Figure 1.2: UBI's 2007 ACC edition second team airplane.

The aerodynamic concept behind this non-conventional configuration shares the same principles inherent to winglets and other vortex drag reduction devices. By positioning the tail surfaces behind the wing wake near the wingtips, they will be emerged in the tip vortex. This way, the flow at these surfaces comes with a relative angle, when creating lift, due to this angle, the resultant force points in the direction of flight transforming the otherwise induced drag in induced thrust.

## 1.3 Objectives

The main objective of this dissertation is to measure the aerodynamic efficiency increase in an aircraft with the described new configuration mainly through flight tests. To increase the knowledge in flight testing UAVs and in the energy based methodology itself is also an objective of the present work. During this work, and to achieve the described objectives, the following points are also objectives:

- Create a baseline conventional tail airplane configuration to compare with the new configuration;
- Estimate the drag polar and compare the efficiency of both configurations;
- Estimate the characteristics of the propulsive system;
- Develop and document the flight testing procedures;
- Increase the knowledge in the energy flight testing methodology;
- Develop and validate the instrumentation needed to perform the flight tests;
- Increase the knowledge in aircraft with this new configuration and propose changes to the concept to increase its efficiency.

## 1.4 Thesis Outline

After this first introductory chapter, in which the studied new concept, motivation and objectives of this master thesis are described, the present dissertation is divided in five more chapters. A brief description of each chapter is presented bellow:

- **Chapter 2** presents the literature review. It starts with the fundamentals of the induced drag, following with the review of the existing devices and configurations to reduce this drag, including novel devices, aircraft configurations and even lift distributions. The fundamentals of aircraft performance and flight testing techniques are also presented; to conclude this chapter, the state of the art of flight testing model aircraft is presented, as it is the case of UAVs.
- **Chapter 3** presents the methodology followed to achieve the objectives of the present work. It starts with the description of the numerical studies. The new configuration aircraft is presented, as well as the propulsive system. The design philosophy of the baseline

conventional configuration aircraft is then presented. The energy based flight testing methodology is formulated together with the flying procedures to execute the flight tests. The necessary data to gather during flight and a presentation of the developed data acquisition equipment is made. This chapter ends with the explanation of the methodology used to analyze the flight data.

- **Chapter 4** presents the results of the flight testing and their discussion. It starts with an overview of the flight testing campaign, a review of the handling of the aircraft and an uncertainty analysis is made. The results of the Pitot tube calibration are also presented. The rest of the chapter presents the drag polar and glide ratio of both: new and baseline conventional configurations tested aircraft, before and after excluding outliers data points. These results are curve fitted and compared with similar works in the literature, and also compared with the numerical results and with those of the described alternative data analysis methodologies. This chapter also includes the results for the characteristics of the propulsive system, and they are compared with other wind tunnel and numerical results. The influence of some particularities of this data analysis methodology are evaluated through the resultant dispersion in the experimentally obtained drag and lift coefficients.
- **Chapter 5** presents the numerical parametric study of the tail position of the present new configuration to better understand this concept and obtain a future improved configuration for this aircraft.
- **Chapter 6** presents the main conclusions and discusses how the objectives were achieved. Future work concerning the performance flight testing of UAVs as well as the improvement of the new configuration are also presented.

# Chapter 2

# Literature Review

## 2.1 Drag Due to Lift Fundamentals

### 2.1.1 Viscous Drag

The drag force is the sum of the drag produced by each component in the aircraft. Each component has a resultant drag force with different and independent origins. As the scope of this study is only at subsonic speeds, the drag caused by flying at transonic and supersonic speeds, wave drag, will not be discussed. Apart from wave drag, there are two principal forms of drag at subsonic speeds, viscous and inviscid. The viscous drag appears from a body being immersed in an airflow and depending on the direction of the resultant force of this form of drag, it can be skin friction drag if the forces are tangent to the body surface and pressure drag if the forces are perpendicular to the body surface. These drag forms are explained in detail at [1]. The viscous drag, in a 2D airfoil, can be measured with the momentum loss at the body wake from the undisturbed flow upstream, Figure 2.1.

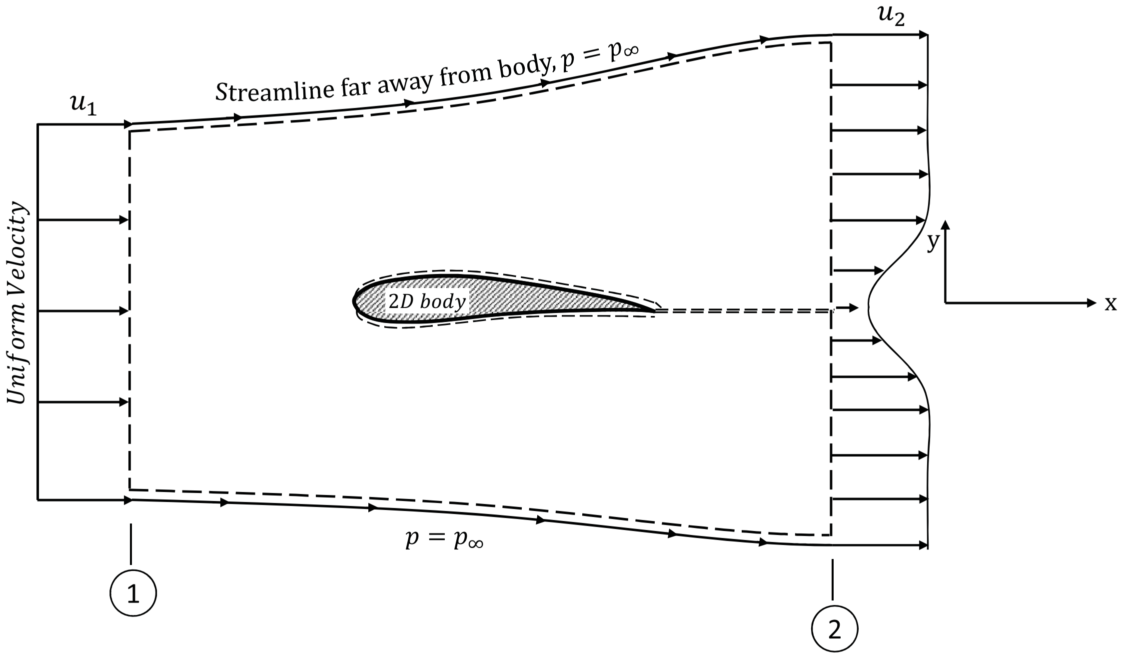

Figure 2.1: Wake momentum loss from airfoil drag, adapted from [2].

### 2.1.2 Lift

Any body exposed to a relative wind is subjected to a resultant aerodynamic force. This aerodynamic force can be considered as the sum of two components: lift and drag. Drag has the same direction of the relative wind while lift is perpendicular to the relative wind. The ratio of lift to drag magnitude is the aerodynamic efficiency of the body. Lift and drag are the aerodynamic forces generated by an airplane during flight and they are the most important ones to the airplane performance. There are two more, the weight of the aircraft and thrust provided by the propulsion system. In Figure 2.2 these 4 forces are represented during steady level flight and they are applied in the aircraft's center of gravity (CG).

- Weight ($W$), force that the Earth applies to the aircraft due to his mass, it is always directed toward the center of the Earth;
- Lift ($L$), aerodynamic force which balances the weight of the aircraft, produced mainly by the wing and it is perpendicular to the relative wind ($V_\infty$);
- Drag ($D$), aerodynamic force that resists to the movement of the aircraft it is also a drawback of producing lift, opposed to the flight direction;
- Thrust ($T$), resultant force generated by the propulsive system, counteracts drag allowing a level flight.

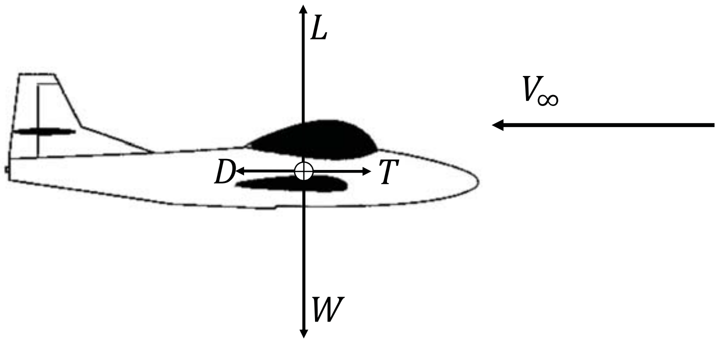

Figure 2.2: Forces applied to the airplane during level flight.

The main contribution for lift comes from the wing, and to generate lift efficiently one of the most important characteristics is the wing cross section shape: the airfoil.

The airfoil generates lift by accelerating the air passing over the top (upper surface) and decelerating the air passing under the wing (lower surface). This can be achieved by deflecting the plane with relation to the relative wind (called angle of attack) and/or with curvature in the airfoil mean line (camber), which consequently deflects the air flow around the airfoil. The deflected elements of air create a pressure difference, in the upper surface this difference is negative and the air is accelerated, in the lower surface the difference is positive and the air is decelerated. The pressure in accelerated air is lower than in the undisturbed flow and the opposite for the decelerated air, where the pressure is higher. This pressure difference generates an upward force called lift in the airfoil and a downward force in the airflow that is deflected past the airfoil as downwash.

Figure 2.3, adapted from Raymer [3], shows the flowfield around an airfoil. In a) the flowfield around the airfoil is represented, from the undisturbed uniform relative wind (freestream) in the left to the downwash on the right, downstream of the airfoil. In b) the velocity vectors represented are the local ones subtracted by the freestream, resultant vectors are only the velocity change due to the airfoil presence. With this representation it is clear that the airfoil introduces a change in airflow that circulates around the airfoil. In c) the circulation around the airfoil is represented. For an airfoil that is generating lift, the line integral of the velocity field is finite and it is the circulation [4], Equation 2.1, where $V$ is the velocity, and $ds$ is the infinitesimal chord length of the airfoil.

$$\Gamma \equiv \oint V \cdot ds \quad (2.1)$$

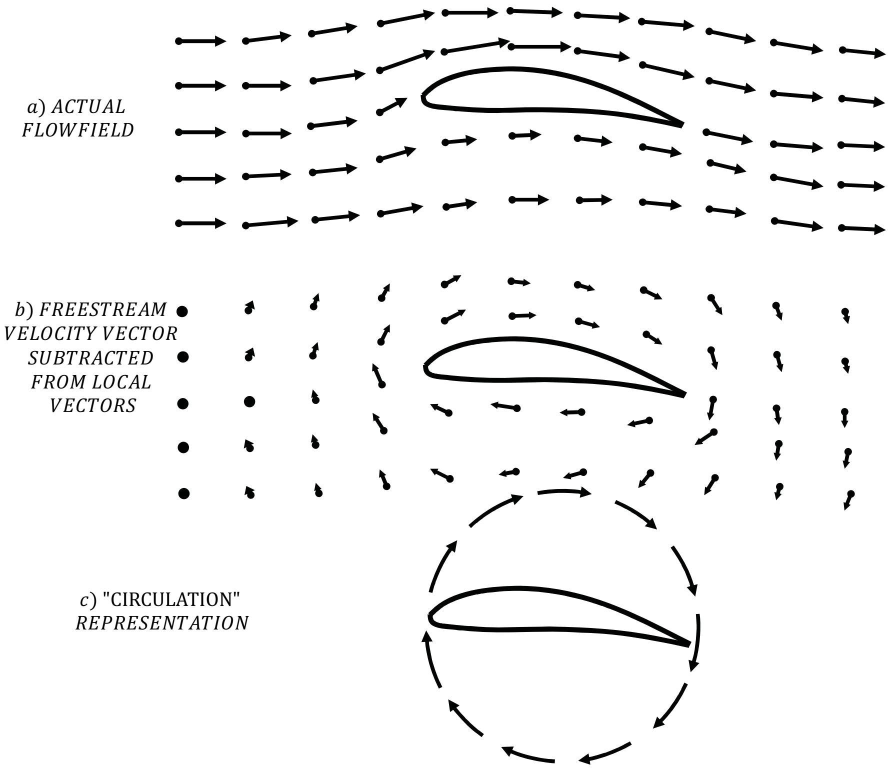

Figure 2.3: Airfoil flowfield and circulation, adapted from Raymer [3].

This circulation around the airfoil allows the calculation of lift. The Kutta-Joukowski theorem says that the lift produced by an airfoil, per unit span, is directly proportional to the circulation around itself, equation 2.2 [4].

$$L' = V_\infty \cdot \rho \cdot \Gamma \quad (2.2)$$

### 2.1.3 Drag Due to Lift

Drag due to lift (DDL) is inviscid drag and it is also known as "Induced Drag" or "Vortex Drag". As explained in 2.1.1, this is one form of the total drag produced by the aircraft and only exists due to the generation of lift, either by wings, tail or fuselage. DDL does not exist in a two-dimensional (infinite) wing. It is called vortex drag because of the appearance of a vortex downstream the wingtip of the three-dimensional (finite) wing. These wingtip vortices are the source of vortex drag which result from the lift needed to maintain flight.

In a practical way, the wingtip vortex is created because of the pressure difference between the upper and lower surfaces of the wings. The pressure on the upper surface of the wing is lower than on the lower surface, so, as air moves from higher to lower pressures zones, the air leaves the bottom of the airfoil and moves around the wingtip to the upper surface creating the wingtip vortex.

The Lifting Line Theory (LLT), published in 1918-1919 by Prandtl, is a simple theory to compute the lift and induced drag of a finite span wing which leads to a better understanding of the formation of induced drag and inherent concepts. Although an extensive explication and formulation of this theory, as well as the assumptions and its limitations are described in [5], in the work of Mineck et al. for induced drag minimization [6], there is a summary of the Prandtl theory.

#### Lifting-Line Theory (Prandtl-Lanchester):

The following explanation for the LLT, completes the Mineck's summary, with some missing details that are explained in [5] and with the simple and practical explanation from Hoerner [1].

The lifting line theory analyzes the flow as a potential field where the wing is modeled as a line vortex of varying strength located at the wing's quarter-chord line along the span. The wingspan is divided in segments (stations) and at any station, the chordwise circulation is placed along the single spanwise line $\Gamma(y)$. This way, the circulation of this straight vortex is the same as that of the physical wing. The lift is obtained through Kutta-Joukowski theorem with the circulation (Equation 2.3), and as the lift cannot end abruptly at the end of the wing, both lift and circulation have to reduce from wing root towards the tip. Because of Helmholtz theorem, a vortex line cannot start or end abruptly in a fluid, therefore, any change of the vortex line strength, which corresponds to a change in circulation, must be followed by introducing a similar vorticity component in the other direction, this requires that the spanwise change in vorticity be shed into a sheet of distributed trailing vorticity. The trailing vorticity is assumed to be aligned with the free-stream velocity and to extend downstream to infinity. The strength of the trailing vortex sheet at any spanwise location is equal to the spanwise change in vortex strength at the corresponding point on the lifting line, Equation 2.4. The velocity that the trailing vortex sheet induces on the lifting line is used to calculate the induced drag of the wing.

$$L = V_\infty \cdot \rho \cdot \Gamma_{wing} \quad (2.3)$$

$$\gamma_x = d\Gamma(y)/dy \quad (2.4)$$

The vortex sheet that leaves the trailing edge of the wing has a more or less constant downwash velocity. After leaving the wing, this vortex sheet transforms itself, "rolls up", into a pair of wing tips vortices, the downwash distribution along wingspan and flow pattern can be observed in Figure 2.4.

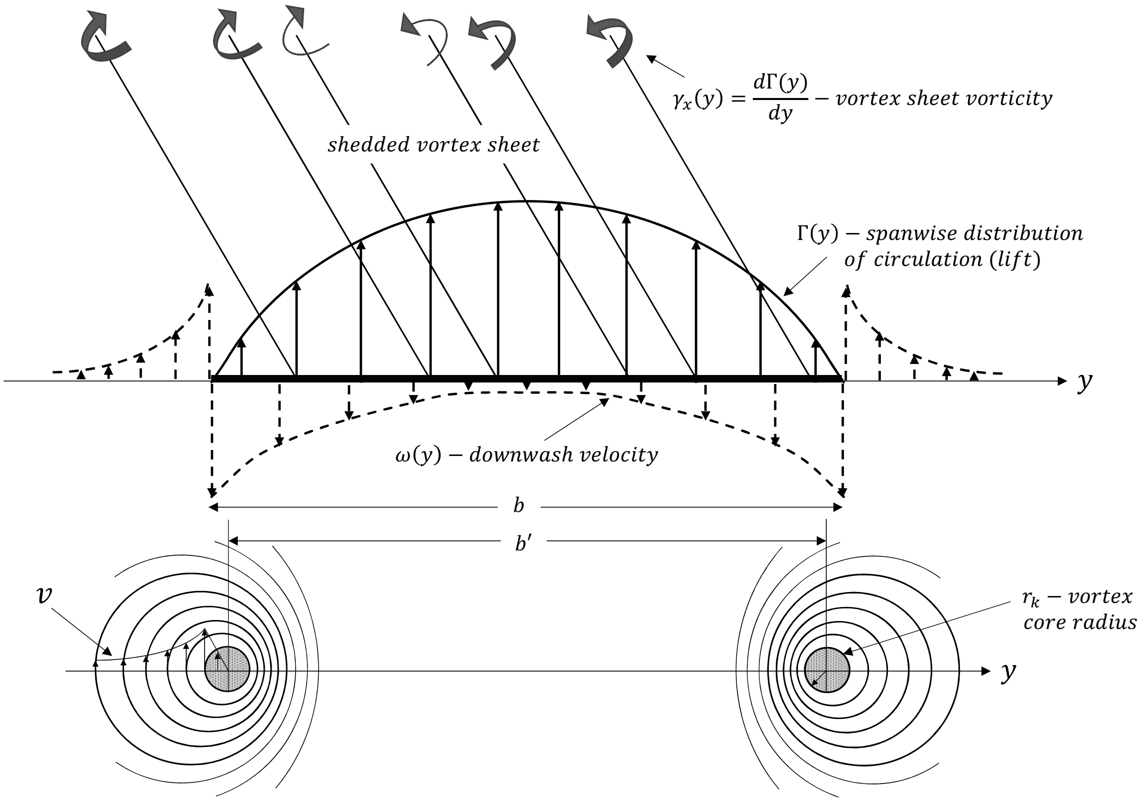

Figure 2.4: Flow pattern and downwash distribution behind lifting line and/or wings.

The induced drag can be seen as the kinetic energy in the vortices leaving the wings tip [7]. The understanding of induced drag physics is important so ways of reducing it can be devised and studied. At the same work, [7], La Roche presents a way of measuring the effect of wingtip shape in the vortex drag reduction, using the center of gravity of the circulation leaving the wing some distance behind it ($b'$) and the radius ($r_k$) of the vortex-core. These parameters are measured far behind the wing, in the Trefftz-plane which is perpendicular to the wake, represented in Figure 2.5. Here the center of gravity of the circulation leaving the wing is coincident with the center of the rolled-up vortices. So, $b'$ is the spanwise distance of the rolled-up vortices pair and $r_k$ their core radius, these vortices are Rankine-vortex with a core of radius $r_k$ rotating as a solid body. Increasing spacing $b'$ decreases the induced drag and an increase in $r_k$ will decrease the kinetic energy of the vortex and consequently the induced drag.

Through the LLT, Munk, one of Prandtl's students, calculated that the minimum induced drag from a planar wing would be obtained if the downwash velocity along the wingspan was constant [8]. This happens when the lift distribution along the span is elliptical and leads to a wing induced drag coefficient given by Equation 2.5. A wing with an elliptical load (or circulation) distribution also has an elliptic chord distribution, the planform is not an ellipse because the chord distribution is around the quarter chord line (lifting line), see Figure 2.6.

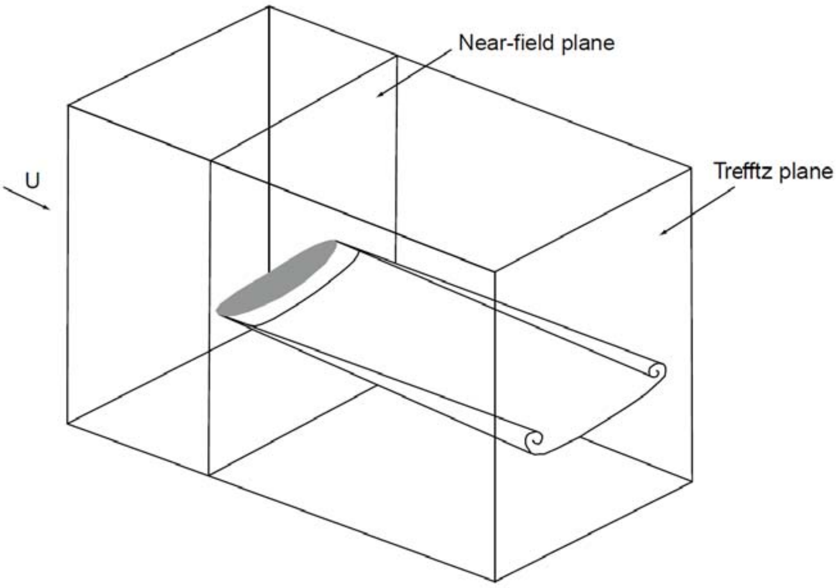

Figure 2.5: Trefftz plane representation [9].

$$C_{Di} = \frac{C_L^2}{\pi AR} \quad (2.5)$$

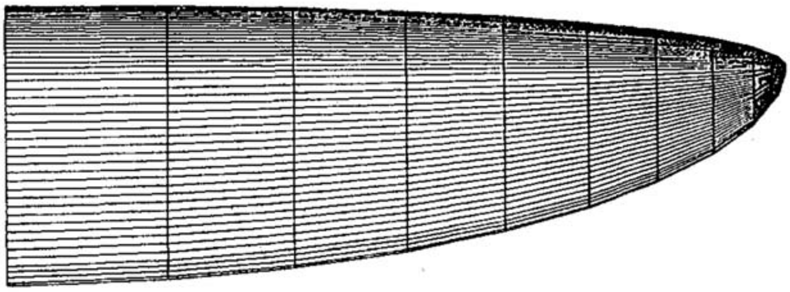

Figure 2.6: Elliptical wing planform [10].

For a wing with a load distribution other than elliptical, a correction coefficient can be added, span efficiency $e_0$, typically having values between 0.9 and 1, being the value 1 for the elliptic lift distribution, Equation 2.6. For a nonplanar wing, span efficiency can be as high as 1.46 for a box-wing [9].

$$C_{Di} = \frac{C_L^2}{\pi e_0 AR} \quad (2.6)$$

$AR$ is the wing aspect ratio, $AR = b^2/S$, $b$ is the wingspan and $S$ is the wing reference area.

It is also usual to use $k_i$ to describe the relative induced drag to the elliptical wing, which is the ratio between the induced drag coefficients of the actual wing and the elliptical wing, Equation 2.7. So $k_i$ can be rewritten as in Equation 2.8..

$$k_i = \frac{C_{Di}}{(C_{Di})_{ell}} \quad (2.7)$$

$$k_i = \frac{1}{e_0} \quad (2.8)$$

Joining the induced drag coefficient with the profile drag coefficient caused by skin friction and pressure drag due to flow separation, $c_d$, results Equation 2.9, which is the total wing drag.

$$C_D = c_d + \frac{C_L^2}{\pi e_0 AR} \quad (2.9)$$

For the whole aircraft, in Equation 2.9 the $c_d$ is changed for $C_{D,e}$, this is the parasite drag coefficient, it contains wings' profile drag and the drag of tail surfaces, fuselage, landing gear and any other component exposed to airflow. Although it is parasite drag and not induced drag, it depends on the angle of attack, especially because of the amount of separated flow over the components and consequently depends on the lift coefficient. $C_{D,e}$ can be rewritten as in Equation 2.10, $C_{D,0}$ is commonly known as the zero-lift drag coefficient. For the whole aircraft, assuming that the parasite drag coefficient is proportional to the square of the lift coefficient, the total drag equation becomes Equation 2.11.

$$C_{D,e} = C_{D,0} + rC_L^2 \quad (2.10)$$

$$C_D = C_{D,0} + \left(r + \frac{1}{\pi e_0 AR}\right) C_L^2 \quad (2.11)$$

In Equations 2.10 and 2.11, $r$ is the effect of the variation of parasitic drag with lift. As explained by Anderson in [4], $r$ can be joined with the span efficiency factor $e_0$ resulting in the Oswald efficiency factor. While the span efficiency factor typically varies between 0.9 and 1.0, as the Oswald efficiency factor includes the parasite drag due to lift and the induced drag, for a complete airplane it usually has values between 0.7 and 0.85. With the Oswald efficiency factor, which is also $e$, the total drag of the airplane can be obtained from Equation 2.12, where $C_{D,0}$ is the zero-lift drag coefficient and the term $C_L^2/(\pi eAR)$ is the total drag due to the lift coefficient.

$$C_D = C_{D,0} + \frac{C_L^2}{\pi eAR} \quad (2.12)$$

As Anderson [11] states, the drag polar in Equation 2.12, usually is not adequate for real airplanes. When flying at zero-lift, the parasite drag might be higher than the minimum value. This way the drag polar has to be translated, resulting in an asymmetrical drag polar, Equation 2.13. $C_{D,0}$ becomes the lowest $C_D$ value $C_{D_{min}}$, and the polar is translated by the $C_L$ value of the lowest drag coefficient value $C_{L_{CDmin}}$.

$$C_D = C_{D_{min}} + \frac{1}{\pi e AR}(C_L - C_{L_{CDmin}})^2 \quad (2.13)$$

There is another approach to evaluate DDL of an aircraft, not only the induced drag coefficient $C_{Di}$ can be optimized (Equation 2.6), but by looking to the induced drag equation (Equation 2.14), it is evident that the wing's aspect ratio $AR$ does not affect the induced drag, only the wingspan does. With the induced drag equation, there is a concept that can be introduced, spanloading $\frac{W}{b}$, that affects exponentially the induced drag.

$$D_i = \frac{W^2}{q\pi b^2 e} \quad (2.14)$$

where, $q = \frac{1}{2}\rho V^2$

Being the main objective to understand how DDL is produced and how to reduce it, other than by using an elliptical distributed lift span loading, the principal and most common way is through wingtip geometry and adding wingtip devices. In either case, the parameters that affect DDL still apply. Among other information, Yates presents in [12] that the vortex spanwise distance $b'$ is affected primarily by the wing tip load distribution and that the integral scale of wake vorticity $l_0$, which corresponds to $r_k$, is affected by the vertical length of the wingtip device. In the design of a wingtip device, endplate, winglet, wing tip sails, and others, the wing distribution should be known and the device should first provide an optimal load distribution. This way, the vertical length needed to have an efficiency increase is reduced. This leads to the conclusion that, retrofitting a wingtip device in an already load optimized wing will generally decrease the efficiency and that a rectangular wing, having the tip heavily (not optimally) loaded, is the best candidate to receive a wingtip device.

## 2.2 Drag Due to Lift Reduction - State of the Art

Attempts to reduce DDL were first made without any additional devices, as described in Section 2.1.3. Simply by choosing an adequate wing planform and airfoil incidence distribution along the span, ensuring an elliptic lift distribution, the wing's drag due to lift would be reduced resulting in the maximum span efficiency $e_0$ of 1. Often, in the literature, the reduction in induced drag of a wing design is not described by an increase in span efficiency but with a decrease of $k_i$, Equation 2.7

Through the years, a lot of effort has been put in reducing even more DDL. Different solutions were developed and they can be divided into several different groups: non-planar devices, that can be active like tip blowing and wing tip mounted propellers, or passive like winglets, endplates, sails; planar wings tip design, like crescent-moon-shape wingtips; non planar surfaces like bi-planes, box wing; novel devices that have some particularities in comparison with other devices that may look alike; new lift distributions; and ultimately non-conventional configurations like outboard horizontal stabilizers (OHS).

Despite these efforts, not all devices that can effectively reduce the induced drag are chosen to be implemented in aircraft. Mainly because there is a lack of studies of their actual benefit in the complete aircraft, some add more viscous (parasite) drag than they can reduce in the drag due to lift and others have structural, energy budget or even stability issues.

Several wingtip designs have been studied. The first ones were not capable of increasing the span efficiency over 1 but they could achieve this value, or close, without an elliptic wing planform, which is already an improvement as it makes the wings easier to build.

Hoerner has designed and studied different wingtips designs [13]. He has analyzed two main variables, wingtip shape, the form of the lateral edge and its influence on tip-vortex location. The wing lateral edge can be square, round or sharp (Figure 2.7 a)); the round edge lets the flow easily go from the lower surface to the upper surface decreasing the vortex spanwise distance, the sharp edge is the most efficient, increasing the spanwise vortex distance. To analyze the wingtip shape, Hoerner introduces the effective aspect ratio. This effective aspect ratio is calculated with the effective wingspan, although this nomenclature is not introduced by Hoerner, the effective wingspan is $b'$. These new wingtip designs are compared with the rectangular trough the effective aspect ration and the parasite drag of that wing tip section. Hoerner concludes that the wingtip design is extremely important for the airplane's performance, and that a sharp edge with the wingtip shape as shown in Figure 2.7 b) and a moderately tapered planform is believed to be the most effective to reduce the DDL.

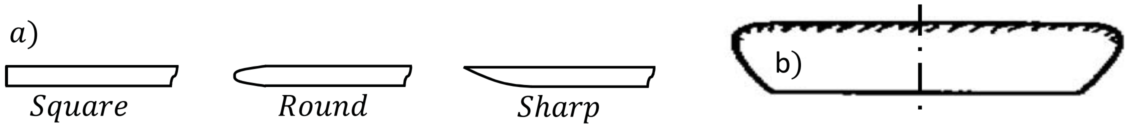

Figure 2.7: Lateral edge and wingtip shape studied by Hoerner [13].

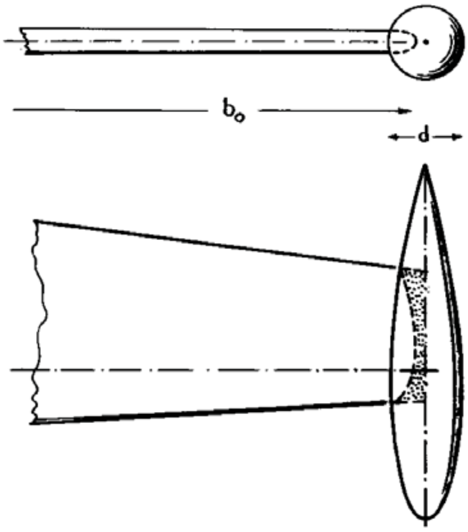

Figure 2.8: External wingtip mounted tank studied by Hoerner [1].

Tanks mounted on the wing tips have the potential to reduce induced drag by 10% [14], Figure 2.8. They have two distinct effects, they increase the span of the wing, that clearly reduces the induced drag, as it is inversely proportional to the square of the wingspan $b$, Equation 2.14 and they can also have a similar effect to end plates [1]. However, as in a round edge, the circular cross section of the tank allows the flow to travel more easily from the lower to the upper surface, so only half of their diameter can be considered to be effective when compared to the endplate height. The parasitic and interference drag between the wing and the tank reduces further the favorable effect of a tip mounted tank.

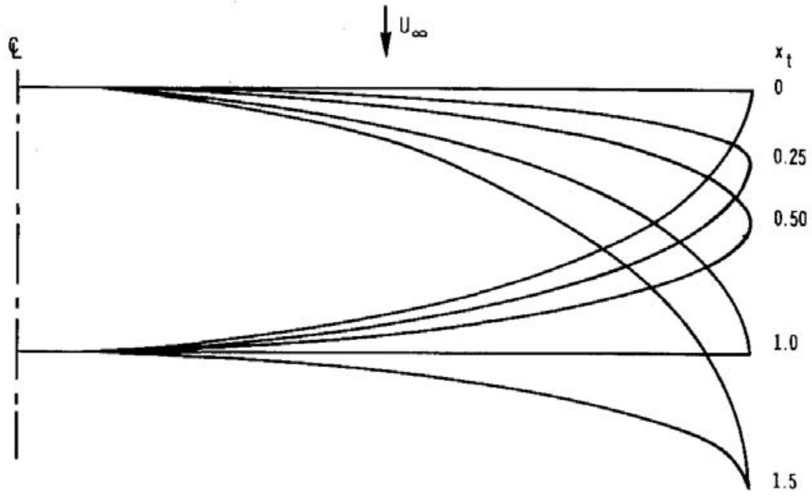

Figure 2.9: Planform geometry for various elliptical wings of $AR = 7$ [15]

Van Dam [15] developed a wing design with highly tapered aft-swept tips. He claimed that these types of wing, called ”Crescent-Moon-Shaped”, was able to produce less drag than the theoretical minimum for an elliptic wing. By comparing different chordwise locations of the wing tip $x_t$, he found that for a tip distance of 150% of the chord value from the leading edge, $x_t = 1.5$, see Figure 2.9, the design would have a $k_i = 0.919$. This result was explained by a thrust force that appeared at the wingtip due to a non-planar interaction of this portion of the wing with the local upwash.

Smith and Kroo [10] also investigated the induced drag characteristics of crescent-moon-shaped wing and even the elliptical wing design. They have concluded that the methods used by Munk [8] and by Van Dam [15] were not accurate enough to predict the induced drag. Through a high-order panel method and with a wake modeling that accounts for wake roll-up in the Trefftz plane, they concluded that the results are very sensitive to the number of panels used and that the conventional elliptical wing does not have a true elliptic lift distribution. This results in a span efficiency of only 0.97 instead of 1. Through the same methods, the crescent-moon-shape with $x_t = 1.0$, has a span efficiency of 0.99, they attribute this result to the lift distribution being closer to elliptic with this wing, than with the conventional elliptical wing.

In the same study, Smith and Kroo have re-designed the elliptical wing with a true elliptic lift distribution (constant downwash spanwise), Figure 2.10, however, the span efficiency achieved is slightly less than 1.0 as for the $x_t = 1.0$ crescent-moon-shape wing.

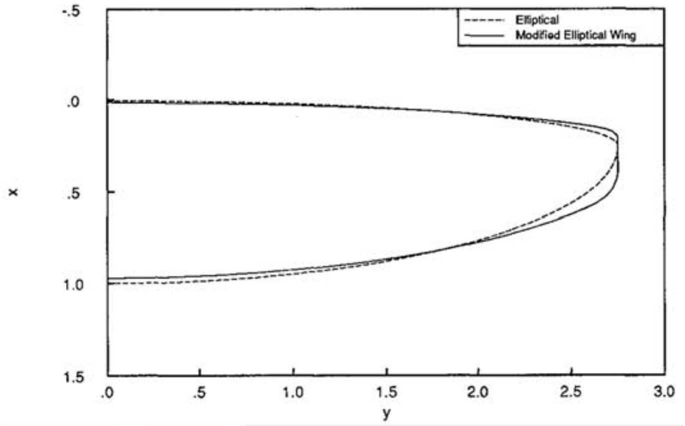

Figure 2.10: Modified elliptical wing planform with elliptic spanwise lift distribution [10].

One of the most common approaches to induced drag reduction is the use non-planar systems from endplates to winglets, spanwise camber to boxplanes. Figure 2.11, shows several non-planar concepts and for fixed span and height, their span efficiency is given. The vertical dimension near the wingtips is the critical parameter, although the box wing has the absolute maximum span efficiency, similar drag reductions can be obtained with other concepts as the spanwise camber is most effective near the tip [16].

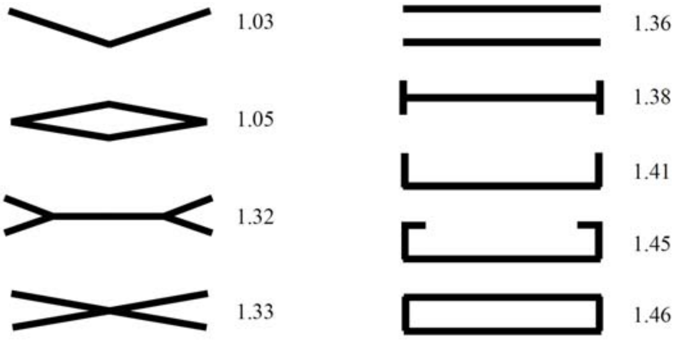

Figure 2.11: Span efficiencies for various optimally loaded non-planar systems ($h/b = 0.2$) [9].

Zimmer [17], has a review with the non-planar induced drag reduction devices created until the year 1987, he reviews the working principles behind the concepts, their application in operational aircraft and their disadvantages.

One of the first concepts is the Whitcomb winglet [18] and some variants, see Figure 2.12 a), they were tested in high wing loading airplanes like the ”KC 135” and the ”DC 10”. The first disadvantage pointed by Zimmer was the need for an increase in the wing structural strength decreasing the aerodynamic gain. McDonnel-Douglas calculated fuel savings of 2.5% to 3% with these devices.

Even though the Whitcomb proved to be an improvement, it was not optimal. Hackett [19] claimed to have an optimal winglet configuration, the vortex diffuser, see Figure 2.12 b). Nevertheless, in this design, there are structural implications. The winglet rests in a small boom behind the wing, and it is mounted vertically, however with a small inboard dihedral angle. This way, the wingtip produces a small downward force that reliefs the wing load, but being mounted so far behind the spar would lead to a necessity in increasing the wing’s torsional rigidity. Also, the downward force reduces the total lift of the aircraft, that must be balanced, for example, with a change in the wing's angle of incidence. Zimmer does not have examples of practical fuel savings from this type of winglet.

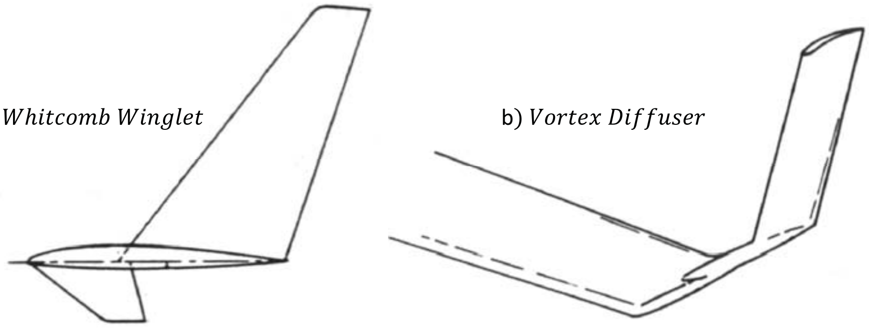

Figure 2.12: Whitcomb winglet and vortex diffuser [9].

The last designs covered by Zimmer are the non-planar multiple sectioned, also called tip sails or feathers. These devices have several individual wings mounted in the wing tips, a design that resembles large soaring land birds. Zimmer reviews and summarizes several studies in these devices by others authors.

Cone [20] announces a drag reduction of 25% in comparison with the planar elliptical wing, obtained from his mathematical model, for a natural fanned wing design, Figure 2.13 a). This design presented by Cone is not easy to build, so W. Pfenninger (cited in Zimmer [17]) suggests the tip design present in Figure 2.13 b).

Hummel (cited in Zimmer [17]), also with theoretical solutions, studied wings with two or three individual wings at the tip and derived a reduction of 14% in comparison with the planar elliptical wing.

Löbert (cited in Zimmer [17]) presents an optimal wing end design with forked points, see Figure 2.13 c), based on a theoretical model. As a function of the position of the partial wings tip and their incidence angle, Löbert reports a reduction of the theoretical induced drag of 40% in comparison with the planar elliptical wing.

Rechenberg (cited in Zimmer [17]), through his theoretical and experimental studies, concludes that the induced drag decreases as the tip vortex is divided into more sections, that is, using more individual wings will decrease even more the induced drag. He predicted that a wing with six individual wings at the tip, would have only 26% of the induced drag of the planar elliptical wing.

Although there are several studies in these multiple devices, and all predict a reduction in the drag due to lift, there is not much information about the total drag savings. These devices increase the parasitic drag and multiple wings attached to the main wing have a lot of interference drag too. Zimmer concludes that "an induced drag clearly below that of an elliptical wing of the same effective extension, has practically never been measured".

Only Spillman [21] realized flight tests with these tip sails. After experimental studies in wind tunnel, he determined the best geometrical torsion where he calculate a K, see Equation 2.15, of 0.84 for three sails mounted in a tip tank, Figure 2.13 d), against K=1.17 for no sails. The flight tests were conducted for three configurations, no sails, one sail, and three sails. The lift dependent drag reduced 9% for one sail, and 29% for three sails, however, these results are supported by relatively low data. For the zero-lift drag, for one sail there is a slightly increase, and for three sails the results predict no increase in comparison with the configuration without sails. The final results of this study show an increase of 25% in the lift to drag ratio of the aircraft with three sails in comparison with the same aircraft without sails.

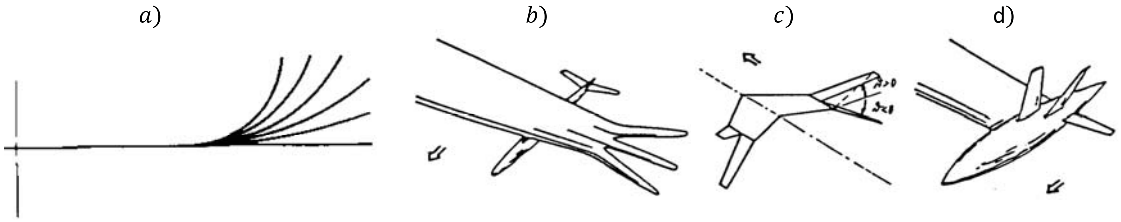

Figure 2.13: Cone tip sail design [20], Pfenninger, Löbert and Spillman tip sail designs [17].

The raked wingtip, see Figure 2.14 was patented by Boeing in 2000 [22], it is somewhat similar to the wingtip shape of the crescent-moon planform and to a winglet. It was developed by Boeing to retrofit existing wings and increase the aircraft efficiency. A study concerning aerodynamic optimization of the KC-135R [23], showed that these types of wingtip devices can be even more efficient than a winglet, increasing the endurance and range of the aircraft in 8.32% and 4.69%, respectively, against a 5.62% and a 3.55% increase from the winglet.

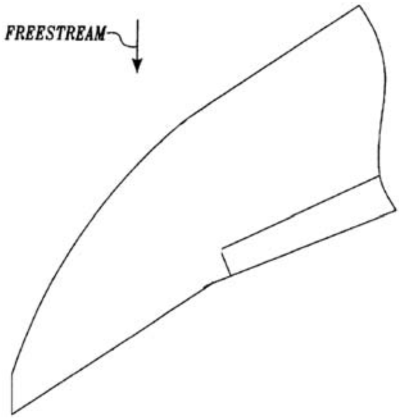

Figure 2.14: Raked wingtip, adapted from [22].

The wing-grid is a novel device presented by LaRoche and Palffy [7], this device does not fit in the conventional wingtip devices as it has a different operating principle. It has a group of horizontal winglets, parallel to each other, mounted vertically at the wing tip; this way, there is a circulation transfer and the shed vortices along the wingspan are transferred into the device (Figure 2.15). To assure this circulation transfer, the winglets must have an angle of attack and overlap chordwise, see Figure 2.16 a). This device reduces the drag due to lift by increasing $b'$ and $r_k$ at the same time, this way $k_i$ can be as low as 0.85.

The spiroid wing tip [24] has the same working principle as the wing-grid, however, instead of the circulation transfer by grid-interference, in this device, the shedded vortices are transferred by the semi-spiral connection pieces of winglets with different dihedral orientation, see Figure 2.16 b).

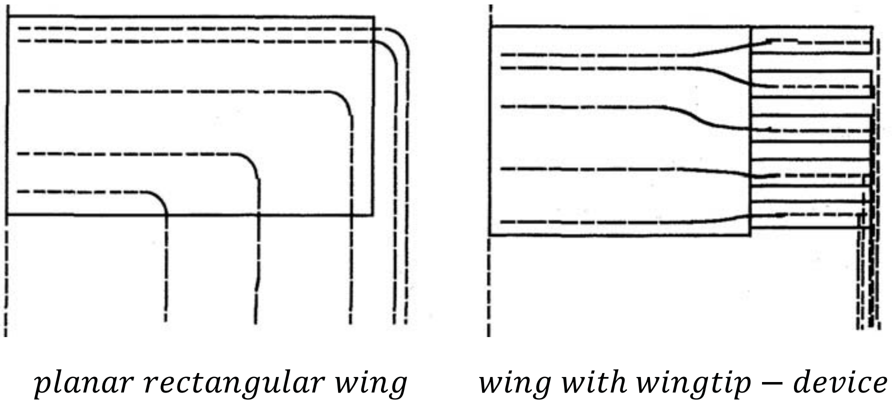

Figure 2.15: Vortex-Shedding of a rectangular wing and a wing-grid tip device, adapted from [7].

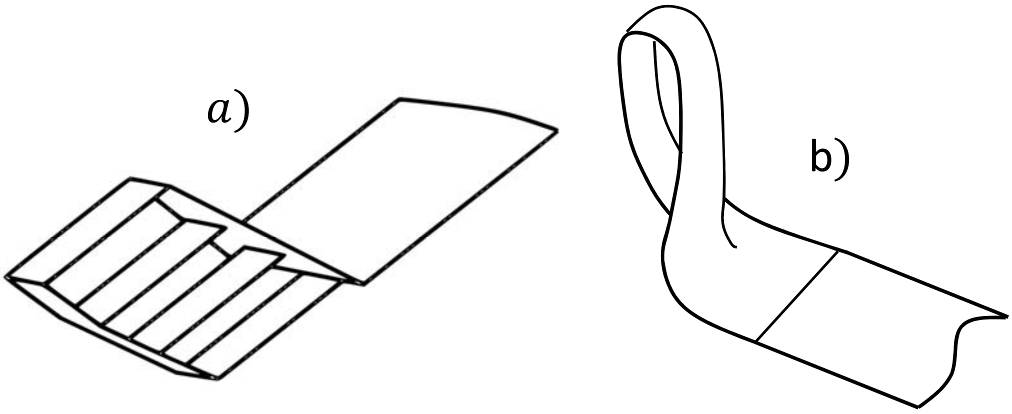

Figure 2.16: Wing-grid wingtip and spiroid wingtip.

The devices already presented are all passive ones, they do not require any additional energy to work. There are active devices that need external energy input so they can reduce the drag due to lift.

Heffernan [25] presents a review regarding several active DDL reduction devices; one of the first ones was an axial blowing jet mounted at the wing tip with the objective of introducing turbulence and consequently increasing the vortex core, $r_k$, however, no noticeable changes in the far wake of the wing were observed. Deflected tip blowing, see Figure 2.17 a), has been experimentally studied in wind tunnel. The Oswald factor increased from $e = 0.62$ to $e = 1.25$ [26], but in the same study it is concluded that such system is not suitable for practical applications due to large energy requirements to blow the necessary air mass rate. Wing-tip-mounted pusher turboprop concept, Figure 2.17 b), has been investigated in NASA Langley Research Center [27], with a propeller rotation, opposite to the vortex roll-up, the vortex circulation around the wingtip could be countered by this device. The study shows that propeller efficiency, if mounted in this location, increases, the turboprop nacelle gives an additional drag reduction and that the induced drag is successfully reduced. However, as stated by Heffernan, the effects of asymmetric thrust in single engine failure and the wing weight increase because of structural considerations may be prohibitive. Nevertheless, this concept can gain life with electric propulsion, since the electric motor is promising in lightweight and reliability.

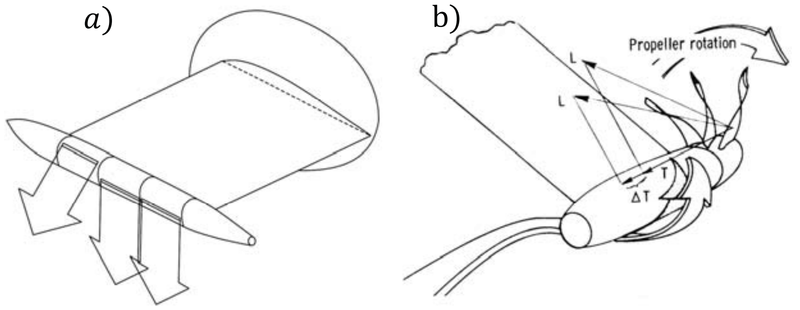

Figure 2.17: Active devices, tip blowing [26] and tip pusher propeller [27].

Advanced non-conventional aircraft configurations have been considered and studied to further extend the airplane efficiency. Kentfield [28] had his life dedicated to the development of outboard horizontal stabilizers (OHS) configurations. In this configuration, the horizontal and vertical stabilizers are mounted in booms, behind the wingtip, see Figure 2.18. With this position, the horizontal stabilizer is in the upwash flow resultant from the wingtip vortex, creating a upward force instead of the conventional downward, increasing the lift. At the same time, the vertical stabilizers, being in the middle of the wingtip vortex, have the local relative wind at a beneficial angle, such that the resultant force is pointing forward, reducing the induced drag. This configuration also increases the static longitudinal stability, however it becomes difficult to achieve a zero pitching moment as the horizontal stabilizer is now producing a nose down pitching moment instead of the nose up existing with the conventional horizontal tail.

McGinnis [29] patented a DDL reduction non-conventional configuration. An aircraft with elevon aerodynamic surfaces that are positioned outward of the central plane and connected to the wing, with vertical structures, at the wingtips and at least three-fourths of the distance from the wingtip to the central plane, see Figure 2.19. Not only this configuration is presented as having better control authority and better behavior regarding stall, it is also said that it has lower induced drag.

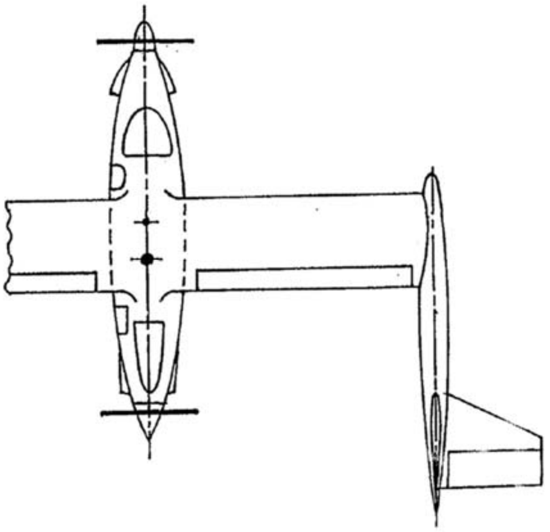

Figure 2.18: Outboard horizontal stabilizers configuration [30].

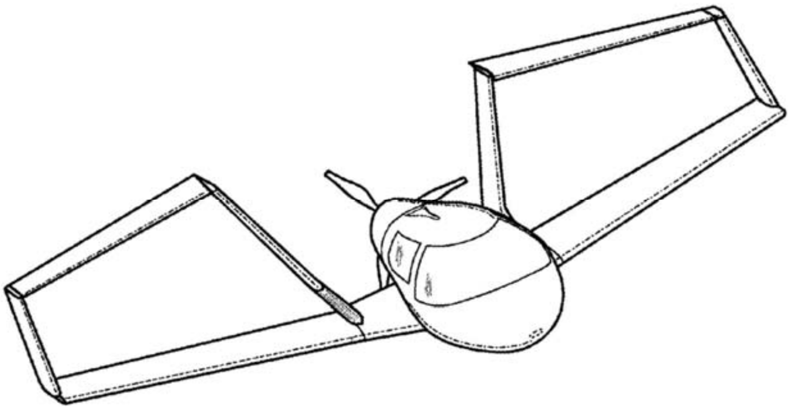

Figure 2.19: Advanced configuration proposed by McGinnis [29].

The present author considers that the latest development regarding concepts for DDL reduction is undoubtedly the work of Bowers [31]. Repeatedly, the elliptical wing and an elliptic lift distribution along the span, have been discussed and taken as the reference of an optimal solution for reducing the induced drag. However in 1933, Prandtl, the father of lifting line theory, after presenting the elliptic lift distribution together with his student Munk as the optimal solution, he presents a new lift distribution, the bell-shaped spanload, Figure 2.20. This bell-shaped spanload leads to a wing that for the same structural weight of an elliptical one, has 11% more aerodynamic efficiency and 22% greater wingspan, making it the new best solution for minimal induced drag, however, this second spanload remains virtually unknown. Around 1935 Reimar Horten, independently, reached to an equivalent solution in his flying wing designs. Prandtl had calculated the total induced drag of a wing with this spanload but without examination of its spanwise distribution and Horten, although he had calculated the induced drag along the span and noticed something singular, never conclusively proved it. During his research, Bowers, concluded that this spanload has a weaker tip vortex, that its position is not at the tips, and that at the wingtips some of the induced drag becomes induced thrust. This induced thrust is ”proverse yaw”, and it is what Prandtl did not realize and what Horten had in his designs but never achieved to prove it. Bowers, under the ”Prandtl-D” NASA program, conducted several flight tests with this design, proving the existence of the proverse yaw and reached other conclusions regarding bird flights, for example, why they do not tip stall and why they fly in formation with wings overlap. In Figure 2.21 is a picture of the model flight tested by the Bowers’ team. It has streamers attached near the wing tips to visually see the location of the wingtip vortex. However, there are no publications of drag results of the bell-shaped spanload, proving that it is better than the elliptic distribution.

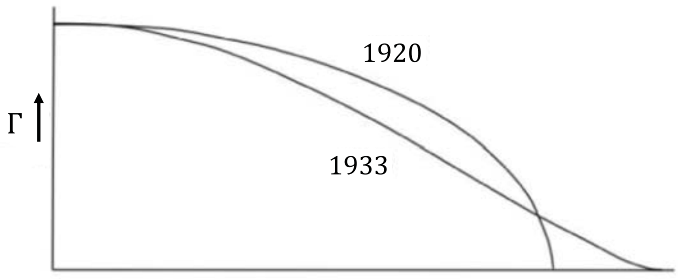

Figure 2.20: Bell-shaped spanload [31].

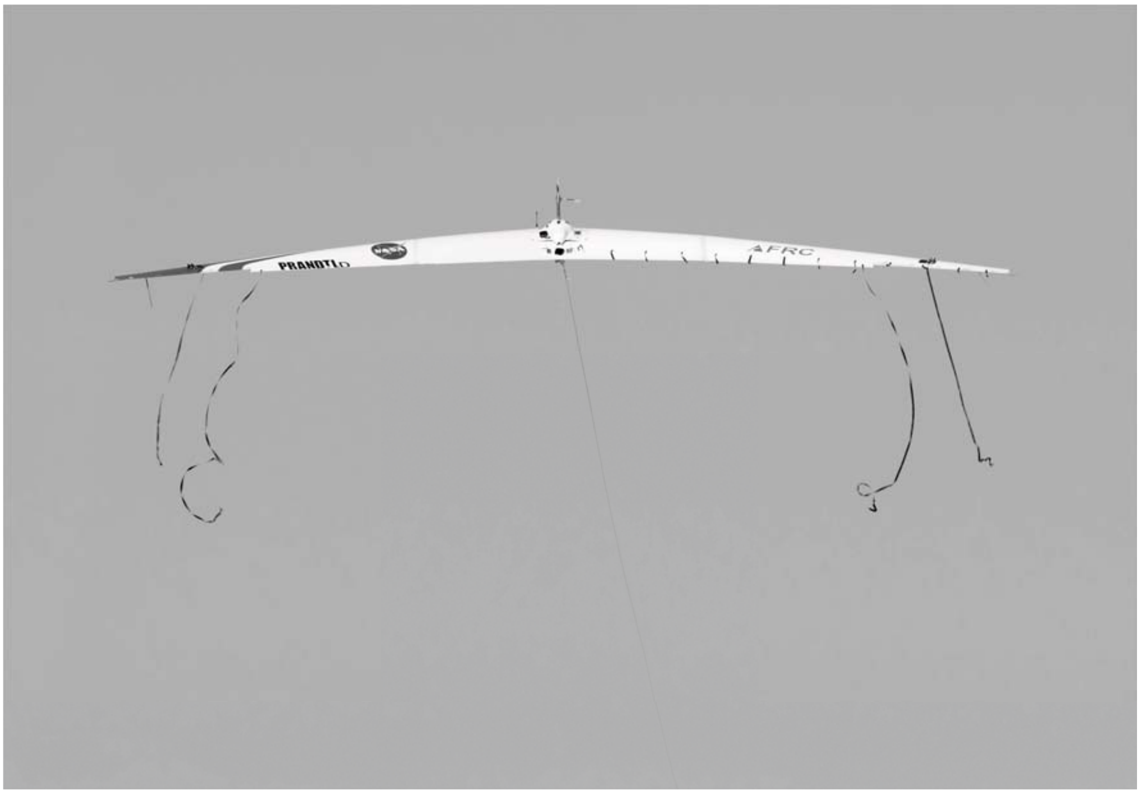

Figure 2.21: Prandtl-D flying wing [32].

## 2.3 Flight Testing Fundamentals

Section 2.1.2 started with the very basics of forces applied to an aircraft during flight. How the aircraft responds to these forces determines its performance and the principal objective of flight testing an aircraft is to obtain its performance. Techniques have to be created so it is possible to obtain these forces through measurable parameters during flight.

Kimberlin [33] says that, ”If the drag polar of an aircraft is accurately determined and the thrust, or thrust horsepower, available is known, then all of the performance characteristics of the subject airplane may be calculated”. So, the main objective of flight testing an aircraft becomes the determination of the drag polar and available thrust.

In Section 2.3.1, it is explained how the performance characteristics can be determined with the drag polar and available thrust, and presents the fundamental performance equations, it does not contain a complete deduction to explain where they come from, as further explanations can be obtained in reference [11].

In Section 2.3.2, the fundamental techniques to obtain the drag polar and available thrust through flight testing are presented.

### 2.3.1 Performance

For a steady level flight, considering that the thrust angle with the relative wind ($\alpha_{Tr}$) is negligible, the forces present in Figure 2.2 are in balance, $L = W$ and $D = T$. Because of this last condition, the drag of the airplane is commonly know as required thrust $T_r$.

The drag polar presented in Section 2.1.3, Equation 2.12, through the introduction of the induced drag factor $K$ (Equation 2.15), can be rewritten as in Equation 2.16, as Kimberlin said, the drag polar is so important because we can directly calculate $L$ and $D$, with the Equations 2.17 and 2.18.

$$K = \frac{1}{\pi e AR} \quad (2.15)$$

$$C_D = C_{D,0} + KC_L^2 \quad (2.16)$$

$$W = L = \frac{1}{2}\rho V_\infty^2 S C_L \quad (2.17)$$

$$T = T_r = D = \frac{1}{2}\rho V_\infty^2 S C_D \quad (2.18)$$

Knowing: the weight of the aircraft $W$; its wing area $S$; the flight altitude to obtain the air density $\rho$, it is possible to calculate $C_L$, for any velocity $V_\infty$, and then, with the drag polar, calculate the required thrust $T_r$. The power required for steady level flight, $P_r$, can be calculated by multiplying the required thrust by the velocity, Equation 2.19

$$P_r = T_r V_\infty = \frac{1}{2}\rho V_\infty^3 S C_D \quad (2.19)$$

One of the most important performance parameters, is the aerodynamic efficiency or glide ratio $L/D$, it can be immediately determined. The aircraft's maximum glide ratio, is a direct result from the aircraft drag polar (Equation 2.16) and can be calculated from Equation 2.20.

$$\left(\frac{L}{D}\right)_{max} = \sqrt{\frac{1}{4C_{D,0}K}} \quad (2.20)$$

Although the results already presented can be calculated from the aircraft's characteristics alone, the propulsive system has to be characterized too. The available power to overcome drag. $P_a$, is a function of the maximum available thrust and velocity, Equation 2.21.

$$P_a = T_a V_\infty \quad (2.21)$$

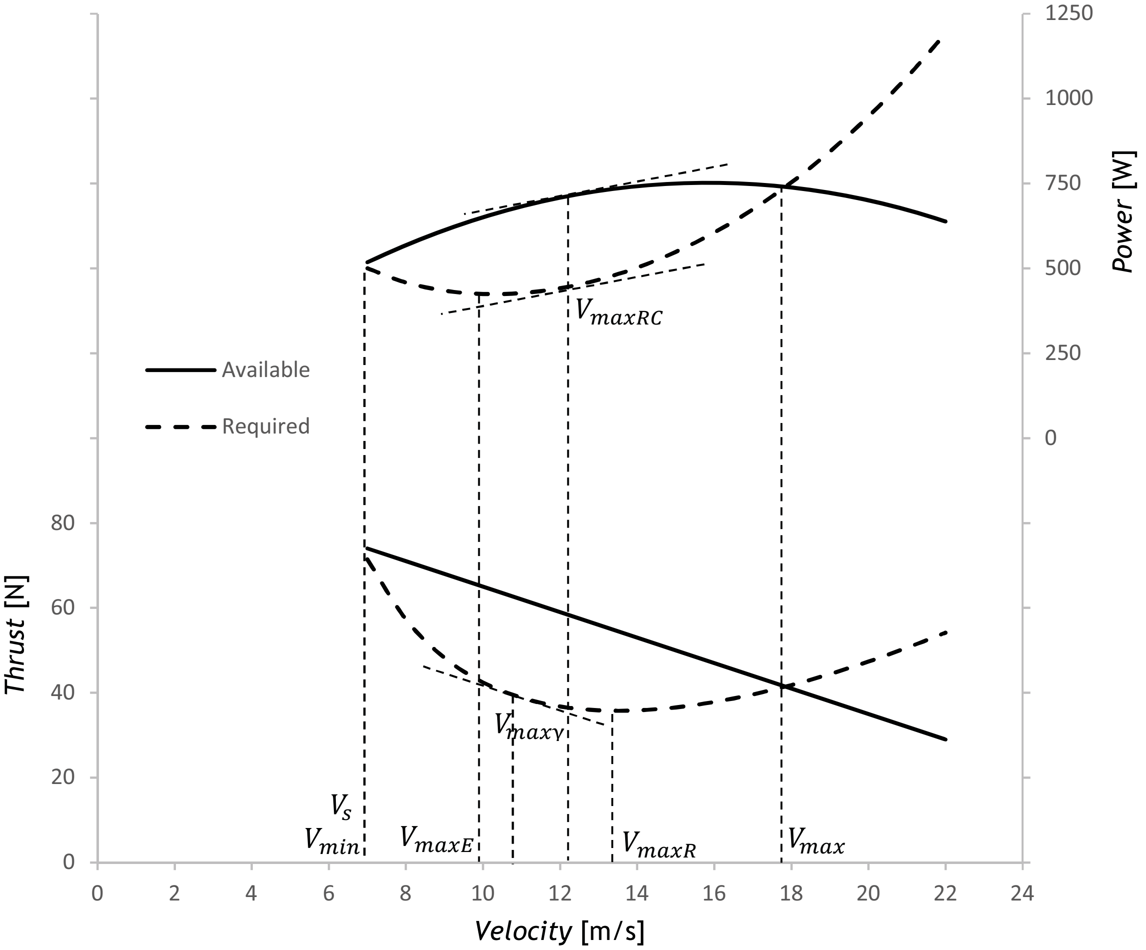

Figure 2.22: Propeller driven aircraft performance analysis from the typical curves for required thrust and power and available thrust and power.

In Figure 2.22 typical curves for the required and available thrust, for a propeller driven aircraft, are represented in the lower part of the figure, and for the required and available power, in the upper part of the figure. These curves are obtained from the drag polar, and propulsive system characteristics. With these curves it is possible to obtain the performance characteristics of the aircraft. The lower possible velocity, the stall speed $V_s$, corresponds to the beginning of the required thrust curve, where the maximum lift coefficient ($C_{Lmax}$) is required. The minimum speed for a steady level flight, $V_{min}$, occurs for the lowest velocity where the available and required thrust, or power, have the same value, usually this velocity is limited by the stall speed instead. The maximum level speed occurs for the same condition at the highest speed, $V_{max}$. The speed for maximum endurance ($V_{maxE}$) and maximum range ($V_{maxR}$) are not coincident; by minimizing the required power the endurance is maximized, that means the velocity for the lowest value in the required power (upper dashed curve in the figure); by minimizing the required thrust the range is maximized, that means the velocity for the lowest value in the required thrust (lower dashed curve in the figure). The difference between the available and required power, is called the excess power and the rate of increase in the kinetic or the potential energy of the aircraft. The rate of climb, $RC$, is the vertical speed and it is calculated dividing excess power by the aircraft's weight at constant speed, Equation 2.22. In the representation, the velocity for maximum rate of climb, $V_{maxRC}$ is obtained when the difference between required and available power is the highest, this happens at the velocity where both curves have the same derivative. With the same analysis for the thrust and drag curves, the climb angle is obtained, Equation 2.23. The maximum climb angle happens for the velocity that has the maximum excess thrust, where the drag curve has the same derivative as the thrust curve, $V_{max\gamma}$ in the figure.

$$RC = \frac{P_a - P_r}{W} \quad (2.22)$$

$$sen(\gamma) = \frac{T - D}{W} \quad (2.23)$$

### 2.3.2 Flight Testing Techniques

Whichever the flight testing techniques or the methodology used to obtain the necessary parameters for the drag polar and available thrust estimation, the environment will affect the flight of the aircraft as well as the obtained results, irrespective of the type of aircraft, manned or unmanned, large or small. Meteorological conditions are very important, all flights should be conducted in similar conditions, and they should not affect the aircraft performance, or if they do, that influence must be reduced to the bare minimum. The flight tests should be done in still air without wind and without thermal activity, these favorable conditions, usually, happen early in the morning after dawn, when the wind speed is lower and the thermal activity has not started.

**Glide Flights:**

Glide flights are the easier technique to obtain the drag polar of an aircraft, by measuring successively the airspeed and rate of descent of the aircraft during a glide, dividing the first by the second, the instantaneous glide ratio of the aircraft is calculated. With its weight, the lift and drag coefficients are obtained for different airspeeds and the drag polar estimated.

**Pressure Probes:**

The easier and usual way to obtain the rate of descent and the airspeed of an aircraft, to apply the glide flights technique, is through the use of pressure probes. With a static pressure probe, it is possible to measure the altitude of the aircraft and consequently the rate of descent. With a pitot-tube and a total pressure sensor and comparing it to the static pressure, it is possible to obtain the differential pressure and measure the airspeed.

**GPS:**

It is possible to estimate the drag polar of the aircraft only with a GPS (Global Positioning System). If there is no wind, the airspeed and groundspeed will be the same. So, it is possible to make several glides, at different speeds and with the altitude and distance measurements from the GPS, calculate the glide ratio of the aircraft. With the glide ratio, the speed and knowing the weight of the aircraft it possible to calculate the lift coefficient and with the glide ratio $L/D$, calculate the drag and drag coefficient, having this values for different speeds it is possible to estimate the drag polar of the aircraft. The usual commercial available GPS receivers, most of the times, do not have the desired precision for this type of experimental studies, however, there are already available receivers capable of real time kinematic (RTK) corrections with horizontal precision of a few millimeters and vertical precision under one meter.

#### Load Cell:

With a load cell mounted on the motor/engine capable of measuring the propeller thrust, and by flying at several speeds, knowing them, without vertical velocity or horizontal acceleration, the required thrust for several velocities is obtained and so is the drag polar. With the drag polar, measuring the rate of climb, the maximum available thrust can also be determined and the propulsive system characterized.

#### Parabolic Drag Polar:

After obtaining the drag and lift values, or coefficients, several regression methods can be applied to fit the data into a curve. However there is a special interest in fitting the results with a curve of the type of Equation 2.16, it is called the symmetrical parabolic drag polar. Although it is only an approximation of the real drag polar curve of an airplane, it is extensively used to fit the airplane real drag polar as with it is possible to obtain the zero-lift drag coefficient $C_{D,0}$ and the drag due to lift factor $K$. The most common way to obtain the coefficients $C_{D,0}$ and $K$ is to plot the drag coefficient values against the square of the lift coefficients and fit the data into to a linear regression to obtain a $y = mx + b$ line, the slope of the line, $m$, is the factor $K$ and the $Y$ intercept, $b$, is the zero-lift drag coefficient $C_{D,0}$. To obtain the coefficients for the asymmetrical drag polar the minimum drag coefficient value has to be found, together with the respective lift coefficient value. Next, the value of the $K$ coefficient, has to be iterated minimizing the error between the iterated drag polar and the experimental results.

#### Energy Method:

The conventional ”steady state” approach to determine an aircraft’s performance is cumbersome, it is hard to maintain constant airspeed. For a climb, the conventional method, does not account for airspeed change while increasing altitude [33].

In the energy method, developed by Edward S. Rutowski [34], therefore also called Rutowski energy method, it is considered that the total energy of the aircraft can be described by the sum of the kinetic energy and potential energy, Equations 2.24 and 2.25. The aircraft’s performance analysis is performed considering the balance that must exist between the potential and kinetic energy change, the energy dissipated due to drag and the energy provided by the propulsive force. The principal strength of this method is that through one equation for the rate of change of the sum of the potential and kinetic energies, the path that minimizes the time or fuel to change from one combination of speed and altitude to another can be found.

$$E = PE + KE \quad (2.24)$$

$$E = Wh + \frac{WV^2}{2g} \quad (2.25)$$

To compare different aircraft, Equation 2.25 is divided by the aircraft's weight, resulting in specific energy $E_s$, Equation 2.26. The specific energy is a length dimension, meters, for this reason it is also called energy altitude $h_e$

$$E_s = h_e = h + \frac{V^2}{2g} \quad (2.26)$$

The equations presented only describe the energy state of an aircraft, to define the performance capabilities of a given aircraft, the ability of changing its energy level in a given time must be determined, Equation 2.27.

$$\frac{dE_s}{dt} = \frac{dh}{dt} + \frac{V}{g}\left(\frac{dV}{dt}\right) \quad (2.27)$$

The left side of this equation, $\frac{dE_s}{dt}$, is change of energy over time, that is the definition of power. So, it is called specific excess power $P_s$ and can be also defined as:

$$P_s = \frac{V(T-D)}{W} = \frac{dE_s}{dt} \quad (2.28)$$

With this approach, the rate of climb can be determined taking in account the aircraft acceleration, so Equation 2.22 can be rewritten as Equation 2.29

$$RC = P_s = \frac{dh}{dt} + \frac{V}{g}\left(\frac{dV}{dt}\right) \quad (2.29)$$

## 2.4 Flight Testing - State of the Art

Flight testing is as old as the airplane itself. Through the years, several approaches and methodologies were developed and documented regarding flight testing of larger manned aircraft, instrumentation, data acquisition and calibration procedures. Flight testing these types of aircraft is a complex process, time consuming, extremely expensive and with a high safety risk.

Models, scaled down versions of large aircraft, are being used since the first times as free flight models or wind tunnel models. Chambers [35], in his book, explains the role of dynamically scaled models in support of NASA's Aerospace Programs, they can be used in several applications, including aerodynamic data gathering in wind tunnel investigations, dynamic stability responses as spin maneuvers and spin recovery, problem-solving exercises for vehicles already in production and proof-of-concept demonstrators for radical aeronautical concepts.

Another type of flight models are the powered ones which can be remotely controlled by a human pilot, now typically known as Unmanned Aerial Vehicles (UAVs), these models can also gather aerodynamic data, dynamic responses and, if scaled down not only geometrically but also dynamically, they can behave the same way a larger aircraft would for the same configuration. UAVs flight testing has several advantages, it is not so complex as for large manned aircraft. UAVs do not require as much time and space since they can be operated outside airports and respective air traffic, they do not even need an authorized airfield. Simply because of their lower costs and simpler logistics they are almost costless when compared with flight testing a regular aircraft, and most of the times they represent negligible risk. Budd et al. [36] cover the operational aspects of using radio controlled models in flight test programs and states that with the advantages of these types of aircraft, they are an adequate way of gathering research-quality data. However, flight testing UAVs is fairly new to the aeronautical environment, the methods developed through the years for large aircraft are not suitable for small UAV flight testing. There is not much literature with methods designed specifically for these small aircraft and even less for performance estimation flight testing. Together with this lack of literature, there are other difficulties as referred by Williams and Harris [37]. One of the principal rules of flight testing large manned aircraft is that a new engine must be tested in an already tested airframe and *vice versa* for a new airframe, normally with certified avionics and data acquisition systems. One of the challenges with small UAVs is that, most of the times, the tests have to be made with an untried airframe, untried avionics and data acquisition systems, untried Ground Control Station (if used) and usually with an engine or electrical motor based on model aircraft technology that was designed for a different usage profile.

There are still operational advantages of flight testing UAVs. Some flight testing methodologies that were impossible since the beginning of airplane tests campaigns such as the glide methods described by Green in [38] to determine lift and drag characteristics, were impossible due to the increment in complexity, weight and unreliability of a mechanical system to stop the propeller or the engine during flight. This methodology can now be considered with electrical UAVs as their motors can be easily stopped during flight and reliably started again.

The avionics and data acquisition systems produced and available commercially for large aircraft are not suitable for UAVs, and even if they were, their costs would not be compatible with the other associated costs. With the advances in microcontroller technology, several low cost, low weight and versatile systems are being developed for both experimental light aircraft and UAVs. This leads to the existence of different systems being used by the few authors of published flight tests regarding UAVs, being the most restrictive characteristics of these systems weight and price. The system developed by Silva and Oliveira for experimental light aircraft and UAVs [39], is based on a microcontroller and several sensors. There are commercially available, low cost microcontrollers that integrate other hardware as A/D converter, PWM, serial communication, internal clock, RAM/EPROM memory, flash memory and programmable I/O, in a single microchip. There are also commercially available low cost sensors with satisfactory precision, compatible with microcontrollers and most of the times with open source code to use them.

The advances in technology for aircraft systems also changed the procedures for flight testing and sensors calibration. Among the most important sensors are the total and static pressure, the difference between those pressures, the differential pressure, is used to calculate the airspeed of the aircraft. The differential pressure can be measured with a pitot tube and static pressure point or with a pitot-static probe for both. In the literature, it is usual to see this pressure measurements being called only by airspeed measurement. Standard airspeed calibration procedures used in large manned aircraft are well documented [40], they are accepted for certification and can be used with smaller aircraft or even UAVs. In a simplistic way, the airspeed calibration is performed comparing the groundspeed of the aircraft with the read airspeed, having in mind that it should be performed in calm days or canceling the effects of the wind by repeating it in opposite directions.

Alternative procedures were developed by Kimberlin and Sims [41] with the arrival of the Global Positioning System. Small and low cost GPS receivers have a satisfactory precision and can be used to calculate the average ground speed with the distance traveled and time, or with the instant groundspeed output from the GPS and then compare with the measured airspeed to obtain a calibration curve for the airspeed values.

Although the usual methodologies for flight testing large aircraft are not adequate for UAVs, these type of aircraft still have the same physical laws. As stated above, stopping the engine during the flight is not practical, so most of the literature focus in having a precise measure of the thrust or other variables that allow the calculation of thrust. Drag is then determined by the required thrust to maintain steady level flight with constant airspeed.

Marshall and Schweikhard [42], describe the methodology for modeling the performance of the F-104G airplane from flight tests results based on the energy method and the fuel consumption. It still needs previous tests for characterization of the engine and, as they have the predicted drag, the procedure is based on the energy method, as they measure the airplane accelerations and compare with the predictions. Although the energy method can be used for level flight and climbs it is only applicable for non-maneuvering flight, with constant power setting and constant direction of flight with a normal load factor of 1. Based on the energy method and the direction of the forces during flight, the authors compute a secondary correction for load factor near one ($\pm 0.2g$).

Norris [43], developed a glide flight testing methodology for measuring the drag polar of propeller aircraft. Then, with the measured drag polar and performing level flights, the propulsive efficiency can be calculated. The drag is obtained during glides with zero-thrust condition while measuring the sink speed and true airspeed. The rotational speed of the engine that gives zero-thrust is sensed with the fore and aft clearance motion of the engine crankshaft. For propulsive efficiency calculations, the power used by the engine is either measured by using measured flight conditions and engine-manufacturers power charts, or the propeller power is estimated. Although the propeller is not producing thrust, it is still rotating, the cited work focus in the interaction of the propeller slipstream with the rest of aircraft that results in lower propulsive and aerodynamic efficiencies than expected.

The literature available concerning flight testing methodologies for small electrical UAVs is mainly centered in the quantification of stability and dynamics [44] and [45]. Normally, during the flight, some maneuvers and control impulses are executed and the response of the aircraft is recorded.

The available literature for small UAVs performance estimation with flight tests, usually does not gather enough data to obtain the drag polar, or they describe testing specifically other performance parameters and end up not predicting the drag polar and propulsive curve that are essential to the entire airplane performance estimation.

Ramsak [46] obtains the drag of a radio controlled (R/C) discus launch glider (DLG) model without any instrumentation in it, it has no internal space, the increased weight of avionics and drag of, for example, a pitot tube would decrease significantly its efficiency. A photogrammetry approach is used to determinate the speed and glide angle of the DLG. The drag values obtained are compared with the results of CFD, but the drag polar, or other performance parameters were not estimated.

Hiller [47], conducts flight tests for drag estimation, although only for three flap settings. The overall performance of the aircraft is not discussed. In his methodology, the drag is obtained through glides, calculating the flight path angle with the airspeed and sink speed. With the measured rotational speed of the engine and previous engine and propeller tests, the thrust is also predicted to allow the calculation of the drag polar.

Jin and Lee [48] conduct their flight test with a different methodology, as for level flight the drag and thrust have the same value, they performed a long flight at the same altitude and constant airspeed and measured the battery voltage and current draw. With previous wind tunnel test for the propulsive system characterization they obtain the thrust which is also the drag. Although they are testing a long endurance UAV with 4.5 hours of endurance, they only realized the flight test at one velocity, making it impossible to obtain a drag polar. The drag value obtained was compared with a CFD simulation, concluding an under prediction of 2.3% compared with the drag from flight testing.

Ostler et al. [49] have the most complete work regarding flight testing of small electrical UAVs for performance analysis. A similar methodology to the one of Jin and Lee [48] is used, the motor and propeller are tested to obtain the propulsive efficiency, a level flight is conducted at several airspeeds, measuring the battery voltage and current draw to later calculate the required thrust which, once again, is the same as the drag. Doing these tests at different values of airspeed, makes possible to obtain a drag polar for the aircraft. Together with the previous tests of the propulsive system, all the performance parameters can be calculated

# Chapter 3

# Methodology

## 3.1 Numerical Study

The proposed concept configuration to reduce the vortex drag is compared with a baseline configuration, first through numerical analysis and then with an experimental approach; several flight tests of a small electric unmanned aerial vehicle are conducted to estimate the drag polar of both the proposed Wing Tip Tail concept and the baseline configurations. At the same time, the flight test methodology used is evaluated and compared with other methodologies. With this methodology, not only the drag polar can be obtained, but also the thrust curve and the global propulsive system efficiency.

The numerical study is divided in three phases: the first phase has the objective of estimating the merit the WTT DDL reduction concept and some of the limitations of the software formulation used in this particular study; the second phase is the creation of the baseline configuration and comparison with the proposed configuration; the third phase starts with a search for the important parameters for the WTT concept to work and later with an effort to optimize the WTT configuration for this particular aircraft.

The software used is the XFLR5 [50] which includes the XFOIL [51] formulation for the two-dimensional airfoil analysis. For the inviscid DDL estimation, the lifting line theory and two different vortex lattice method (VLM) are used for the finite wing and tail surfaces analysis. XFLR5 is continuously being developed and updated, there is not enough information covering each version, and the available information, not only is not known for which version it was released, as most of the time does not have the essential information to understand which analysis type is most suitable for the intended objectives. In the document [52], that briefly explains the methods used in the calculations, it is explained that the VLM methods are the most suitable for multiple surfaces analysis, it is also stated that the second VLM method, VLM2, is the recommended by Katz and Plotkin[5] for calculations in configurations with elevator and fin.

Both VLM analysis are well suited for multiple surfaces, although they are not described in the document [52], in the work of Maskew [53] it is explained that the quadrilateral (ring) vortices allow the calculation of the deformation of force free wakes through the vortex sheet roll-up. XFLR5 has the type 1 VLM1-Horseshoe vortex and type 2 VLM2-Ring vortex, to better understand their differences and their influence in the studied configurations, both methods were used in two different configurations. One configuration with a conventional inverted ”T-tail”, Figure 3.1 b), and another with the horizontal tail in the same position, but the vertical tail divided in two and placed near the wingtips, Figure 3.1 a), to understand how the methods simulate the interaction between the wing and tail. The same study could be performed between the WTT configuration and a baseline conventional configuration, however, both VLM methods are influenced by the planform of the tail, what would lead to a misleading results difference between the VLM methods.

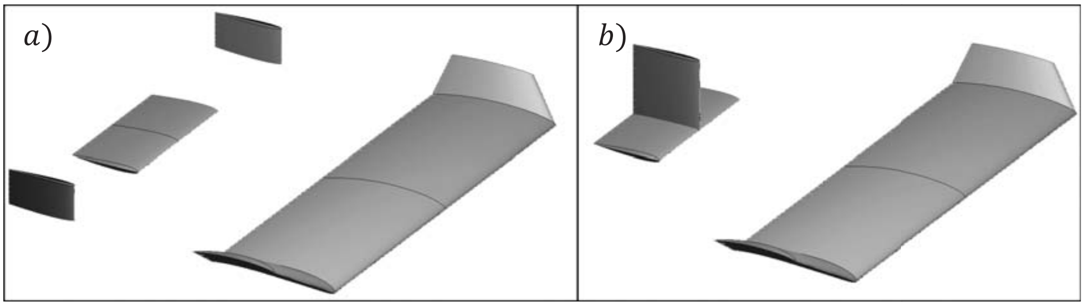

Figure 3.1: XFLR5 configurations used to test the different vortex lattice methods.

Given the two tail configurations in Figure 3.1 used to test the XFLR5 VLM methods, Figure 3.2 presents the result, where ”tip” is the configuration a) in Figure 3.1 and ”conv” is the configuration b) in Figure 3.1. The first conclusion is VLM1 and VLM2 methods do give different results for the same configuration. While VLM1-Horseshoe vortex is not sensitive to the vertical tail position, VLM2-Ring vortex estimates that the tail configuration where the vertical surfaces are at the wingtips, has a better maximum value of glide ratio. It is possible to conclude right away that VLM2 is the suitable vortex lattice method for this study, and that it seems there is a drag reduction for a tail configuration with surfaces behind the wingtips. This drag reduction is more noticeable at higher lift coefficient values.

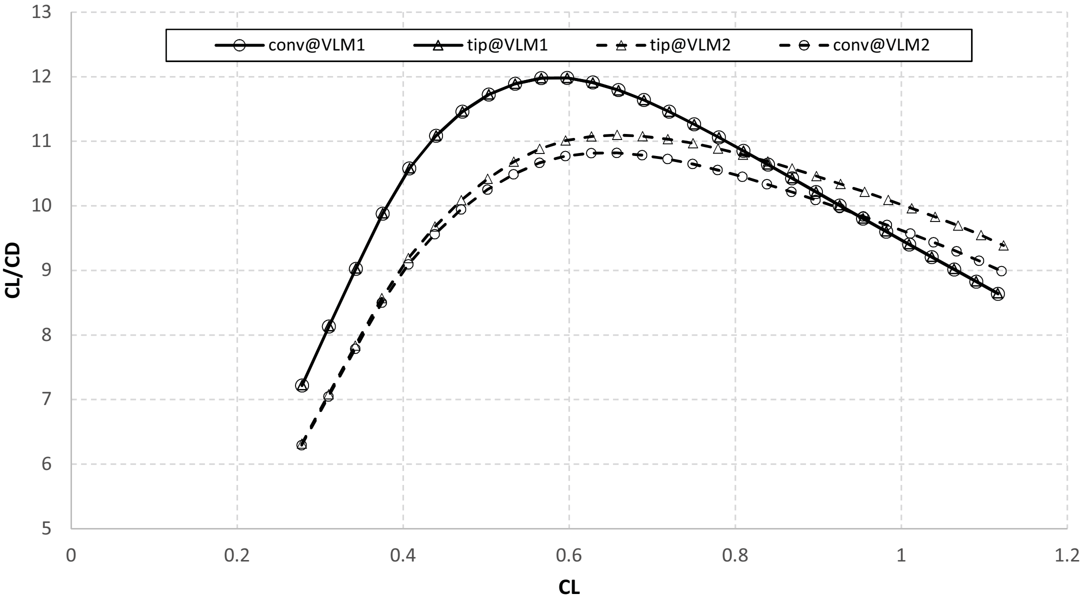

Figure 3.2: XFLR5 vortex lattice methods analysis for tail surfaces at the wingtips.

After choosing the adequate VLM method, it is possible to perform the numerical analysis. The proposed WTT configuration is compared with a baseline, a conventional configuration that serves as a reference to verify the existence of a reduction in the vortex drag and a consequent glide ratio increase. The baseline configuration is designed carefully to ensure that any differences between their performance is mostly due to the aerodynamic concept in study, the design of this baseline configuration is discussed in Section 3.3.

### 3.1.1 WTT Concept Improvement

A study for improving the WTT configuration was performed by systematically changing the design variables of the WTT concept geometry regarding the tail position and comparing the resultant glide ratio value with the one from the original WTT aircraft. The tail variables: spanwise distance from the center plane of the tail surfaces; the vertical distance; the angle of incidence; the wing's angle of incidence; the dihedral angle was inverted and the longitudinal (chordwise) position were systematically changed and the results analyzed. To keep the tail volume coefficient constant, the tail surface area is changed in the same proportion of the tail moment arm. The results from this type of study, in this software, have to be critically evaluated, as sometimes, a slight change in the tail position leads to big changes in the airplane drag that are not real but rather a limitation of the program or from the surfaces mesh.

## 3.2 Wing Tip Tail Concept Configuration

### 3.2.1 Brief Description

The aircraft used in this study, is geometrically similar to the one used in the 2007 ACC. New wings were built with a carbon fiber (CFRP) D-box to increase the torsional stiffness. The aircraft was further modified for the present work. A previously built fuselage was modified to carry the data acquisition system, attach the wings and allow the assembly of the conventional tail. This wingtip mounted tail configuration is extremely difficult to transport if it has not detachable tail surfaces. So, the existing tail booms were cut and an interface between them and the wings was designed to make it easy to disassemble, transport and assemble.

### 3.2.2 Propulsion

As stated in Section 3.1, the WTT configuration is implemented in a small electrical vehicle. The power plant is the same allowed by the ACC regulations [54], an electric brushless outrunner motor, a lithium polymer (LiPo) battery of any capacity with three elements in series and an APC propeller. Given the origin of this aircraft, the Air Cargo Challenge, besides the flight testing equipment, it is able to carry a heavy battery and still have good excess power to fly comfortably. Two different batteries that were already available were used. The propulsive system components and their characteristics are described in Tables 3.1, 3.2, 3.3, 3.4 and 3.5. Battery number two, Table 3.4, was modified to double the capacity, the model of the battery presented is the original and the characteristics are the final ones after the modification.

### 3.2.3 Airframe

In this configuration the aircraft has a $1.71m$ wingspan, $1.5m$ length and $4kg$ of take of mass. Detailed dimensions and specifications are described in Table 3.6 and a photograph is present in Figure 3.3. An important detail about this configuration is the position of the center of gravity ($CG$), usually, for small UAVs, the $CG$ is between 25% and 33% of the mean aerodynamic chord

Table 3.1: Electric brushless outrunner motor characteristics [55].

| Technical Specification | |
|---|---|
| Model | AXI 2826/10 Gold Line (V1) |
| Rotational Constant KV | 920 RPM/V |
| Max. Efficiency | 84% |
| No load current | 1.7 A |
| Current Capacity | 42 A |
| Internal Resistance | 42m$\Omega$ |
| Dimensions ($\phi$ x L) | 35x48 mm |
| Mass | 181 g |

Table 3.2: Electronic speed controller (ESC) characteristics [56].

| Technical Specification | |
|---|---|
| Model | Castle Creations Phoenix Lite 100 |
| Min. Input Voltage | 7.4 V (2S LiPo) |
| Max. Input Voltage | 29.6 V (8S LiPo) |
| Max Continuous Current | 100 A |
| BEC Voltage | 5 - 8.4 V |
| BEC Current | 5 A |
| Mass | 91.5 g |

Table 3.3: Battery number one characteristics [57].

| Technical Specification | |
|---|---|
| Model | SLS APL 10000mAh 3S1P 11.1V |
| Voltage | 11.1 V |
| Configuration | 3S1P |
| Capacity | 10000mAh |
| Continuous Discharge | 25 C |
| Burst Discharge | 40 C |
| Mass | 710 g |

Table 3.4: Battery number two characteristics [58].

| Technical Specification | |
|---|---|
| Model | Basher 4000mAh 6S 65C |
| Voltage | 11.1 V |
| Configuration | 3S2P |
| Capacity | 8000mAh |
| Continuous Discharge | 65 C |
| Burst Discharge | 90 C |
| Mass | 604 g |
| Added Ballast | 106 g |

Table 3.5: Propeller characteristics [59].

| Technical Specification | |
|---|---|
| Model | APC 13x7 Sport Propeller |
| Diameter | 13” |
| Pitch | 7” |
| Mass | 47.9 g |

($MAC$) of the wing, in this aircraft it is at 20% of the MAC, the concept behind this position is an effort to increase the drag reduction. With a fore $CG$ position, to achieve longitudinal stability, the tail must produce a higher downforce. As the WTT induced thrust is proportional to the downforce, it is increased. The landing gear only has one main wheel in the center of the fuselage ahead of the $CG$, the tail tubes (booms) have skids for during the take-off run, the aircraft is controllable and easy to take-off with this configuration. Shortly into the take-off run, the tail rises and the aircraft is flown while still supported on the single wheel main gear by the ground.

To ensure the airplane is controllable up to its maximum level flight velocity, the wings must have a high torsional stiffness due to the high pitching moment caused by the tail acting near the wing tip region. This is particularly serious when a roll elevon input is performed at high airspeed, leading to aileron reversal after a certain airspeed in the original ACC aircraft. To solve the issue, the present WTT aircraft has a 33% chord carbon fiber D-box, balsa wing ribs and covering film.

In this specific version of the WTT configuration, each tail surface is mounted at 80% of the wingspan, at the end of a carbon fiber tail boom tube. In the wing, at the tail mount position, there is a wood reinforcement and a carbon fiber tube built in the D-box, behind the wing spar. The wing ribs next to the tube were reinforced with plywood so they had enough strength to allow mounting the interface. The interface between both carbon fiber tubes is done with an external nylon tube and a clamp in one side, that is screwed to a rigid point between the reinforced wing ribs, see Figures A.1, A.2 and A.3. The wing is attached to the fuselage through four points, two at the leading edge and two at the wing spar. The tail is all constructed with balsa and covering film.

Figure 3.3: Wingtip tail configuration.

Table 3.6: Wing Tip Tail configuration model airplane's main dimensions.

| Wing Tip Tail Configuration Dimensions | [mm] |
|---|---|
| Wing | |
| Airfoil | SG6043 |
| Wingspan | 1710 |
| First section wingspan | 695 |
| Root chord | 450 |
| Tip section wingspan | 160 |
| Tip chord | 300 |
| Tip dihedral | 40 deg |
| Tail | |
| Wing trailing edge to tail leading edge distance | 270 |
| Wingspan | 345 |
| First section wingspan | 120 |
| Root chord | 510 |
| Second section wingspan | 225 |
| Mid chord | 250 |
| Tip chord | 150 |
| Elevator chord | 100 |
| Tail dihedral angle | 35 deg |
| $\bar{V}_h$ | 0.34 |
| $\bar{V}_v$ | 0.042 |
| Fuselage | |
| Nose length | 280 |
| Total length | 770 |
| Maximum height | 170 |
| Internal width | 80 |
| Fuselage width | 130 |
| Take-off Weight | 40 N |

## 3.3 Baseline Configuration

The baseline configuration, which serves as a reference to analyze the effects of the proposed configuration, was carefully designed to ensure that both aircraft configurations are similar in everything except for the tail such that any difference in their performance will be due to the tail differences. The easier and best way to achieve this, is to use the same wing and fuselage in both configurations, and to create the necessary mechanisms in order to change between the two sets of tails. This way, the tails are really the only difference between the WTT concept and baseline configuration.

At this point, a conventional tail was designed, an inverted T configuration. First, it was chosen to design equivalent tail surfaces to those of the WTT concept configuration. However, as in the WTT concept configuration the tail is very close to the wing, this philosophy would lead to a conventional configuration but not conventional surface dimensions and positions. Therefore, the conventional tail design philosophy was a compromise between an adequate level of similarity between both tails and, at the same time, the conventional configuration should not be too far from an independently designed tail. The tail surface area is calculated with the historic volume coefficients for the tail [3], Equations 3.1 and 3.2. Given the relatively low aspect ratio wing, the horizontal tail will have a larger surface than the vertical tail, to keep the resultant parasite drag in conventional values, the horizontal surface is positioned behind the vertical, and the trailing edge of the conventional vertical tail has the same distance from the wing as the trailing edge of the tail surfaces of the WTT configuration. The tail volume coefficients and dimensions resultant from this philosophy are presented in Table 3.7.

Table 3.7: Initial tail dimensions for the baseline conventional configuration.

| Configuration | Inverted ”T” |
|---|---|
| Vertical tail | [mm] |
| $\bar{V_v}$ | 0.042 |
| Span | 300 |
| Root chord | 250 |
| Tip chord | 130 |
| Horizontal tail | [mm] |
| $\bar{V_h}$ | 0.42 |
| Span | 475 |
| Root chord | 300 |
| Tip chord | 180 |

$$\bar{V_h} = \frac{S_h l_h}{S\bar{c}} \quad (3.1)$$

$$\bar{V_v} = \frac{S_v l_v}{Sb} \quad (3.2)$$

In Equations 3.1 and 3.2, $S_h$ is the horizontal tail surface area and $S_v$ is the vertical tail surface area, $l_h$ and $l_v$ are the moment arms (distance from tail surface aerodynamic center to aircraft's CG) for the horizontal and vertical tail surfaces respectively. $S$, $b$ and $\bar{c}$ are the wing's area, span and mean chord, respectively.

The resultant tail of the baseline configuration, as well as the tail from the WTT configuration, are overlapped in Figure 3.4, allowing a direct comparison between the two different tail configurations.

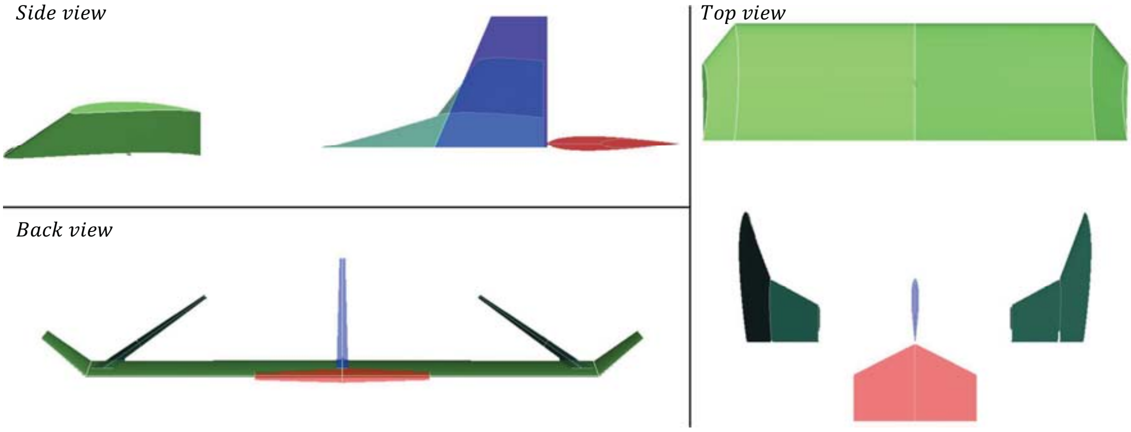

Figure 3.4: Tail design comparison with both configurations overlapped.

Further changes to the tail were necessary after the first flight of the baseline configuration. The aircraft had dutch roll. To correct this effect, the vertical tail surface area was increased. It was increased twice and flown each time. After the second correction the aircraft was successfully controllable. Both configurations had the same vertical tail volume coefficient, the need of a larger vertical tail surface is justified with the lack of interaction from this surface with the wingtip vortex, as seems to be happening in the WTT. So, the horizontal tail, that is also not in the wake of the tip vortex, had the surface area slightly increased too. The final tail dimensions are present in Table 3.8

Table 3.8: Final tail dimensions for the conventional configuration.

| Configuration | Inverted "T" |
|---|---|
| Vertical tail | [mm] |
| $\bar{V_v}$ | 0.056 |
| Span | 470 |
| Root chord | 250 |
| Tip chord | 80 |
| Horizontal tail | [mm] |
| $\bar{V_h}$ | 0.48 |
| Span | 585 |
| Root chord | 300 |
| Tip chord | 150 |

The baseline configuration tail was not the only change needed after the first flights. With its tail configuration, with a single tail boom in the center of the airplane, the mono-wheel landing gear is no longer stable enough to perform the take-off run. Since the take-off distance is short ($< 60m$), and taxi capabilities are not needed, the solution was to add two wheels behind the $CG$ to add lateral stability. They are easily removable and allow a successful take-off.

Automatically, with two extra wheels, the parasite drag is increased. But, being the objective to compare both configurations, this can be seen as a disadvantage of this conventional configuration. In this configuration, the $CG$ position had to be changed too, to achieve a comfortable aircraft handling and control. The $CG$ had to be changed to an aft position of about 30% of the MAC. The last change that was done, concerning the piloting of the baseline configuration aircraft, was the angle of the motor thrust line. A negative angle had to be added, so it was possible to easily climb the aircraft, only applying throttle, without loosing too much airspeed and end up with a stall followed by an abrupt altitude loss.

The final baseline configuration is shown in Figure 3.5.

Figure 3.5: Conventional configuration.

## 3.4 Flight Testing Methodology

The flight testing methodology is based in the kinetic and potential energy of the aircraft. For a closed system, the total energy remains constant, so, when gliding, the loss in potential energy should be compensated with an increase in the kinetic energy. In reality, not all the potential energy is transformed in to kinetic energy, as there is energy dissipated from the drag of the airplane. As presented in the Section 2.3.2, the effects of environment in the airplane should be zero, however, it is impossible to ensure that, so they should be minimized. Wind and thermal activity represent an external energy source and would affect the results of the tests. The exact methodology used, that is described in the present section, is only possible for aircraft that can turn the motor/engine off during flight, and then, turn it on again. Not only it has to be turned off, but it must brake itself as well, as the propeller can not be rotating. This is the case of brushless electric motors, so for electrical UAVs of any size, this methodology can be applied.

Another advantage of this type of aircraft for the methodology, is that electrical airplanes do not change its weight during the flight with the fuel consumption.

If the second Newton law, $F = m\frac{dV}{dt}$, is applied to the free body diagram of Figure 3.6, in the direction of the relative wind, the result is Equation 3.3.

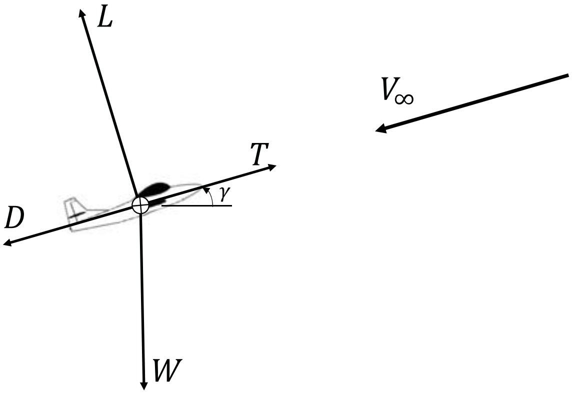

Figure 3.6: Free body diagram during flight for drag and thrust calculation.

$$T - D - Wsin(\gamma) = m\frac{dV}{dt} \quad (3.3)$$

Replacing $m = \frac{W}{g}$ :

$$T - D = \frac{W}{g}\frac{dV}{dt} + Wsin(\gamma) \quad (3.4)$$

$$\frac{T - D}{W} = \frac{1}{g}\frac{dV}{dt} + sin(\gamma) \quad (3.5)$$

Multiplying both sides of Equation 3.5 by the velocity, Equation 3.6 is obtained.

$$\frac{(T - D)V}{W} = \frac{VdV}{gdt} + Vsin(\gamma) \quad (3.6)$$

$Vsin(\gamma)$ is the vertical velocity which is the time variation of altitude $\frac{dh}{dt}$. Representing the derivatives of the altitude and velocity with $\dot{h}$ and $\dot{V}$, respectively, solving Equation 3.6 for the drag $D$ and considering a glide flight, with a stopped propeller and consequently zero thrust, $T = 0$, the result is Equation 3.7.

$$D = -\frac{\dot{h}W}{V} - \frac{\dot{V}W}{g} \quad (3.7)$$

Equation 3.7 is the first equation of this methodology; with it, it is possible to calculate the instant drag of the airplane during a glide by measuring the altitude and velocity variation, the velocity and knowing the weight of the aircraft.

Now, with the free body diagram in Figure 3.7, applying the second Newton law to the vertical direction, it is possible to obtain a correction for the calculation of lift. During a glide, the airplane is not producing enough lift to keep the aircraft in a steady level flight, so, the lift coefficient should be calculated with this correction instead of considering the lift equal to the aircraft weight. From Equation 3.8, Equation 3.9 can be obtained considering that for small glide angles $Dsin(\gamma) = 0$. In Equation 3.8 the acceleration is vertical, so it is the derivative of the vertical speed. The vertical speed was already presented as the altitude derivative, so the vertical acceleration is the second altitude derivative, represented as $\ddot{h}$.

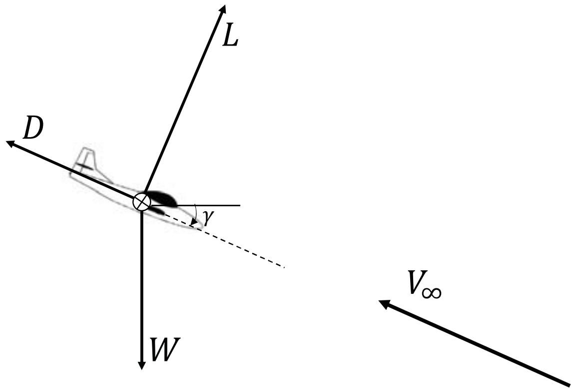

Figure 3.7: Free body diagram during flight for the lift correction calculation.

$$Lcos(\gamma) - W + Dsin(\gamma) = m\frac{dV_v}{dt} \quad (3.8)$$

$$L = \frac{\ddot{h}m + W}{cos(\gamma)} \quad (3.9)$$

In Equation 3.9, the gliding angle $\gamma$ can be calculated with Equation 3.10.

$$\gamma = arctg\left(\frac{\dot{h}}{V}\right) \quad (3.10)$$

With Equations 3.7, 3.9, 3.11 and 3.12 it is possible to calculate the drag and lift coefficients of the airplane and estimate the drag polar through several glide flights without motor at different airspeeds.

$$C_L = \frac{2L}{\rho V^2 S} \quad (3.11)$$

$$C_D = \frac{2D}{\rho V^2 S} \quad (3.12)$$

Remembering that Equation 3.7 was obtained considering that the thrust in Equation 3.6 was zero, after estimating the drag polar of the airplane, the drag for any velocity is known. In Equation 3.6, the only unknown variable is the thrust. So, if Equation 3.6 is solved for thrust $T$, Equation 3.13 is obtained and for a flight, with a load factor near one and a known throttle position, it is possible to calculate the available thrust, repeating this procedure at several airspeeds, the thrust curve of the propulsive system can be estimated.

$$T = \frac{\dot{h}W}{V} + \frac{\dot{V}W}{g} + D \quad (3.13)$$

With the estimation of the thrust curve as a function of the velocity, the available power $P_a$, can be calculated directly with Equation 3.14. To further estimate the characteristics of the propulsive system, having the available power, by measuring the electrical power $P_e$ consumption from the battery, the global efficiency of the propulsive system, $\eta_p$, can be determined with Equation 3.15. The electrical power $P_e$ is calculated with the voltage $U_{bat}$ and the current drain from the battery $I_{bat}$, Equation 3.16.

$$P_a = VT_a \quad (3.14)$$

$$\eta_p = \frac{P_a}{P_e} \quad (3.15)$$

$$P_e = U_{bat} I_{bat} \quad (3.16)$$

This flight testing methodology has several advantages in comparison with the others that are being used with UAVs.

In comparison with the methodology used in the work of Ostler [49] and the similar one in the work of Jin [48], this methodology, together with the developed data acquisition system, excludes the necessity of a more expensive autopilot system to do the data acquisition and piloting. An autopilot is usually harder to implement as it is necessary to read its documentation and the data acquired is not ready to be analyzed and manipulated. The data acquisition system developed does not need any special attention from the user, it only records the useful data for this methodology and the output file is ready to be analyzed and manipulated. From the piloting point of view, install and tune an autopilot to test an aircraft is not an easy task, it is very time consuming and the pilot still must be able to pilot the aircraft manually. Although this methodology needs the aircraft to be manually controlled, it is easier than the usual dynamic methodologies where the pilot must perform several maneuvers so that performance can be estimated. Especially with small UAVs these maneuvers are not easy to perform as flying line of sight is a limitation. In this methodology it is only needed to perform several glides followed by a climb. For electric UAVs this is relatively easy, as the motor can be turned on and off, and during the same flight perform several glides and climbs.

Experimental works, in any field of study, are a special activity that usually need more resources, time, facilities, manpower, have complex procedures and this details consequently increase the associated costs. Continuing comparing the methodology of this thesis with the methodology of Ostler and Jin, in their work, the propulsive system and aircraft are tested separately and their characterization are both mandatory. The drag polar of the aircraft is determined with flight tests together with the thrust curve that was obtained with wind tunnel tests. With this method only the aircraft is needed, and the drag polar can be estimated without the thrust curve. Not only this is an advantage as the drag of the airplane can be estimated without wind tunnel tests, as the conventional wind tunnel tests for the propulsive characterization can be changed for flight tests. This is clearly an advantage for universities or companies that do not have a wind tunnel.

In this methodology, like the others that are being used for small UAVs that are remotely piloted at line of sight, the line of sight is a disadvantage. Especially with this non-conventional tail configuration, the aircraft becomes very slim at the distance, and it starts to be uncomfortable to fly. Especially at higher speeds, as the airplane can not be piloted at high distances (horizontally or vertically), the time duration of the glides is not long enough to obtain as much data as it would be desired.

Another disadvantage if this method is used with the intention to compare with numerical simulations, is the drag of the propeller, during the glides the motor is braked and the propeller is stopped causing drag. In the scope of this work this is not a limitation, as both configurations will have the same propeller stopped, this extra drag will be the same for both. Once again, in the other methodologies this is a problem too, especially for steady level flight where there is also the slipstream effect that will increase the drag of the airplane. This limitation of the presented methodology can be reduced if a folding propeller is used, the drag of this type of propeller is almost zero.

### 3.4.1 Alternative Methodologies

There are other flight testing methodologies based in glide flights. While this methodology estimates directly the drag polar of the aircraft, the other methodologies first estimate the glide ratio at several speeds and then calculate the drag polar.

**Geometrical glide ratio:**

Since the aircraft is equipped with a GPS receiver, it is possible to determine the geometrical glide ratio with the horizontal and vertical distance. The traveled distance is not a direct output of the GPS, so, it is determined by the sum of the instantaneous groundspeed $V_{GND}$ multiplied by the time between measurements. The vertical distance is the difference between the altitude at the beginning and at the end of the glide. The instantaneous lift coefficient is also calculated, with Equation 3.17, being the glide ratio $L/D$ the horizontal distance divided by the vertical, it is calculated with Equation 3.18 and for each glide the $L/D$ for the average $C_L$ is obtained.

$$C_L = \frac{2W}{\rho V^2 S} \quad (3.17)$$

$$L/D = \frac{\sum_{i=1}^{n} V_{GND_i}(t_{i+1} - t_i)}{h_1 - h_n} \quad (3.18)$$

**Glide angle:**

As the glide ratio can be calculated with the horizontal and vertical distances, it is also possible to calculate with the glide angle, Equation 3.19. In this equation, if the glide angle is replaced with Equation 3.10, solving for the glide ratio, it can be calculated with Equation 3.20. In Equation 3.20, $V$ is the airspeed and as already presented, $\dot{h}$ is the vertical velocity. In this method, the instantaneous glide ratio is calculated, and for each flight, for the average $C_L$ of that glide, the glide ratio is the average of the instantaneous glide ratios.

$$tg(\gamma) = -\frac{1}{L/D} \quad (3.19)$$

$$L/D = \frac{V}{\dot{h}} \quad (3.20)$$

One of the principal disadvantages of this alternative methodology is the number of outlier points, if for an instant, the aircraft have a positive, or close to zero vertical speed, as only the vertical speed counts, it will result in a negative or extremely high glide ratio value that causes the glide ratio average of that glide to change completely.

Summing up, the principal equations to implement the proposed methodology are the drag equation, the corrected lift equation, and the thrust equation, Equations 3.7, 3.9 and 3.13, respectively. After the analysis of these equations, it is possible to understand that, for the drag polar and thrust curve estimation with this methodology, what parameters have to make part of the necessary data and must be obtained by the data acquisition equipment. In Section 3.4.2 the procedure to obtain these data during flight will be discussed and in Section 3.5 how the data acquisition by the system is made will be discussed.

### 3.4.2 Flight Procedure

This section presents the adopted procedures concerning the flight tests, however, piloting an UAV is not an exact science and for some parameters different approaches could be used to reach the same objectives. The flight test campaign can be divided in several parts, the weather, the setup, the first flight, the glide and the climb.

As presented in the fundamental theory, Section 2.3.2, the meteorological conditions and the environment should make the minimum interference possible in the flight of the aircraft.

Although the energy method should be able to be used with some wind speed, and testing this is an objective too, all flight tests were done in days without or unnoticeable wind speed. To minimize the possible influence of rising air currents, that is thermal activity, the tests were preferably done early in the morning at the dawn, at this time, usually the wind also has its minimum velocity and most of the times it is even still.

As stated by other authors [37], and as every activity in the aeronautical field, all approaches should be methodological, if one relies in his memory, it will eventually fail and cause problems or an accident. The setup and the flight test must be thought of before, as the time is limited. A delay in the setup of the test due to a lack of preparation, will delay the flight and increase the probability of wind and thermal activity to start, that can make the flight inappropriate to obtain data. The setup time should influence the project of the aircraft, so everything can be assembled and prepared at the field with the minimum time possible. To ensure that the setup is done the fastest possible and that nothing is left behind, a flight test checklist should be prepared with all the necessary steps in order. For almost any aircraft, the flight time is limited, for UAVs usually the flight time is extremely limited, so it is important to plan the flight. It is easier to follow the plan and obtain more useful data if the pilot knows the aircraft well, its behavior and can comfortably control it. Figure 3.8 presents the most important points of the checklist used during the flight testing campaign, most of the points covered in this list are common to other flight test campaigns of different aircraft.

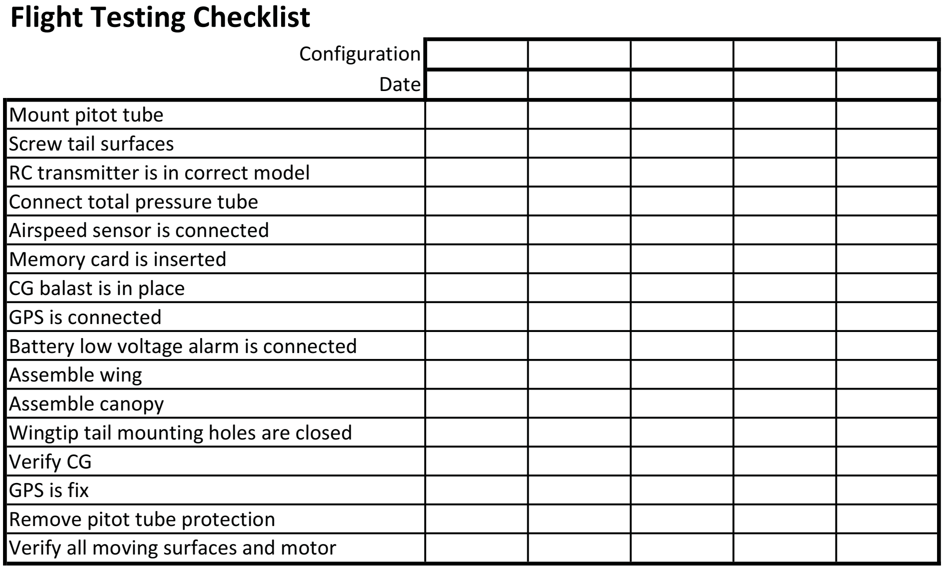

**Flight Testing Checklist**

| | | | | | |
|---|---|---|---|---|---|
| Configuration | | | | | |
| Date | | | | | |
| Mount pitot tube | | | | | |
| Screw tail surfaces | | | | | |
| RC transmitter is in correct model | | | | | |
| Connect total pressure tube | | | | | |
| Airspeed sensor is connected | | | | | |
| Memory card is inserted | | | | | |
| CG balast is in place | | | | | |
| GPS is connected | | | | | |
| Battery low voltage alarm is connected | | | | | |
| Assemble wing | | | | | |
| Assemble canopy | | | | | |
| Wingtip tail mounting holes are closed | | | | | |
| Verify CG | | | | | |
| GPS is fix | | | | | |
| Remove pitot tube protection | | | | | |
| Verify all moving surfaces and motor | | | | | |

Figure 3.8: Flight testing checklist.

The first flight is important to be done in a day without any wind as it is not a test flight but a calibration flight. The pitot tube must be calibrated, several steady level (constant altitude and without acceleration) passes are done in at least two perpendicular directions and in both ways, this is repeated for the most different directions possible or even fly in large circular paths. With this flight, considering that there is no wind speed, the airspeed and groundspeed should have the same value and the pitot tube can be calibrated with the help of the GPS. In a second first flight, or at the same flight, the airplane controls have to be trimmed. Usually an airplane is trimmed for the cruise settings, however, the trim of airplane while the motor is running will be affected by the torque of the propeller and during the glides, as there is no torque, the airplane would not do a glide without turning. As the glides are the most important part of the flight, the airplane is trimmed during glides to make sure that no inputs are needed to maintain a glide, these inputs would increase drag with a lot of uncertainty. Without turning and control inputs the aircraft is not affected by the imprecise control inputs.

After the first flight, the flight testing campaign may start, as well as the glides and climbs. As already explained, the drag is estimated through the glide and it should be as steady as possible. To do so, the control inputs should be minimized before, after and nonexistent during the glide. The glides have to be performed at different airspeeds, the control of the airspeed is made with the elevator, as controlling it manually would be extremely difficult and imprecise, the ”trim” button at the transmitter (radio controller) is used to fly at different airspeeds. After the first glide at the cruise elevator position, the elevator is trimmed to achieve a different airspeed and the glide is repeated, this process is repeated for higher airspeeds with ”nose down” trim and lower airspeeds with ”nose up” trim. At the end of the glide, the altitude should not be too low, first the motor is turned on, if the airplane does not start climbing, only after increasing the throttle, the elevator can be controlled by the pilot to end the glide. Especially for lower airspeeds, attention is needed at the beginning of the glide, to start a glide, the opposite at the end has to be performed, first the elevator stops being controlled and then the engine is turned off. Before the beginning, the airplane has to be cruising at the desired airspeed for the next glide, if it is flying with too much throttle and speed, at a non-steady state, after turning the motor off, the airplane will oscillate longitudinally leading to an invalid glide or even a series of stalls.

For thrust determination, the climbs can be done at different flights or after each glide. They should be carried at full throttle to obtain the maximum thrust curve and with as little control inputs as possible. During the climb the airplane can have longitudinal acceleration but not vertical, so, if any control input has to be given to maintain a climb or prevent a stall, it has to be done with small movements at the controls. During the flights, a rule of thumb to keep the vertical acceleration as low as possible, is to keep the angular velocity at a minimum, one should not see the airplane rotating as in take-off or during a loop, where a circular path is described, the airplane should always fly in straight lines.

## 3.5 Data Acquisition Equipment

A data acquisition equipment was developed to obtain the needed data during the flight. More than the ability to register the flight parameters that allow the computation of the drag and lift to estimate the drag polar or the thrust curve, there are two characteristics that are extremely important, the weight and cost. An effort to minimize them and still have a reliable and capable system should be done.

Observing several components equipment that are on the market and that are being developed to do similar studies, it was chosen to use a microcontroller as the base of the entire system. There are several microcontrollers commercially available that fit the cost and weight requirements, with satisfactory processing capacity and very important too, a lot of support online with open-source code. Arduino Mega2560 [60] board with an ATmega238 microcontroller and other features was chosen, that makes the implementation in this study relatively easy. Arduino boards are the most used worldwide, with a lot of documentation and online support, it has several sensors that are specially developed with libraries or code right available. The relevant specifications for this microcontroller board are present in Table 3.9 and it can be seen in Figure 3.9. An electrical schematic of the complete data acquisition system can be found in Figure A.4.

Table 3.9: Microcontroller board specifications [60].

| Technical Specification | |
|---|---|
| Model | Arduino Mega 2560 |
| Microcontroller | ATmega2560 |
| Operating Voltage | 5 V |
| Input Voltage | 7-12 V |
| Digital I/O Pins | 54 |
| Analog Input Pins | 16 |
| Flash Memory | 256 KB |
| Clock Speed | 16 MHz |
| Mass | 37 g |

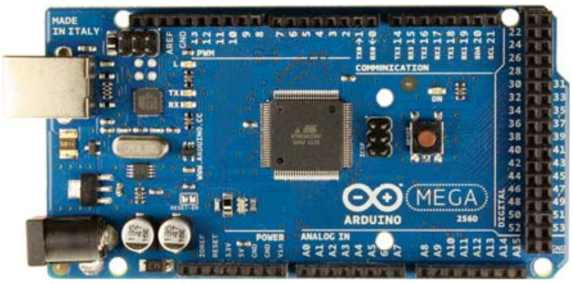

Figure 3.9: Arduino Mega microcontroller [61].

After describing the methodology in Section 3.4, it is possible to summarize the data that the system must be able to record. For the airspeed calculation, which needs some corrections presented in Section 3.6, further atmospheric parameters have to be recorded:

- Time, $t$
- Altitude, $h$
- Airspeed, $V$
- Groundspeed, $V_{GND}$
- Battery voltage, $U_{bat}$
- Current drawn, $I_{bat}$
- Pressure, $p$
- Temperature, $T_k$

Time, altitude and groundspeed are recorded by the GPS receiver, an Adafruit GPS [62], Figure 3.10, with a MTK3339 receiver; it has a library available from the manufacturer specially developed for this unit, the principal specifications are described in Table 3.10. The date is also recorded as the satellites number as well, to make sure that the minimum satellites for a correct position are available. To make the system faster, the coordinates are not recorded.

Table 3.10: GPS receiver specifications [62].

| Technical Specification | |
|---|---|
| Model | Adafruit Ultimate GPS Breakout |
| Receiver Module | MTK3339 |
| Sensitivity | -165 dBm |
| Update Rate | 10 Hz |
| Channels Number | 66 |
| Max. Satellite Number | 22 |
| Supply Voltage | 5 V |
| Mass | 11 g |

Figure 3.10: Adafruit GPS receiver [62].

As the pressure and temperature have to be recorded too, it is possible to calculate the altitude pressure, this results in a higher precision altitude measurement when compared with the output from the GPS. The digital static pressure sensor is the BMP180 [63], Figure 3.11. It also measures the temperature and has a library available from the manufacturer specially developed for this unit, the principal specifications are described in Table 3.11.

Table 3.11: Digital static pressure and temperature sensor specifications [63].

| Technical Specification | |
|---|---|
| Model | BMP180 |
| Supply Voltage | 3.6 V |
| Interface | $I^2C$ |
| Pressure Range | 330 - 1100 hPa |
| Temperature Range | -40 - +85 °C |
| Pressure Error | ± 0.01 hPa |
| Temperature Error | ± 0.1 °C |
| Mass | 5 g |

Figure 3.11: Temperature and pressure sensor [64].

Although the airspeed is a direct output of the developed system, it is calculated through the differential pressure. The equipment has a MPXV70002DP [65] analog differential pressure sensor, Figure 3.12. It does not have a specific library, more information can be found in the datasheet [65] and the principal specifications are described in Table 3.12.

Table 3.12: Differential pressure sensor specifications [65].

| Technical Specification | |
|---|---|
| Model | MPXV70002DP |
| Supply Voltage | 5 V |
| Pressure Range | -2 - +2 kPa |
| Error | 2.5 % |
| Mass | 10 g |

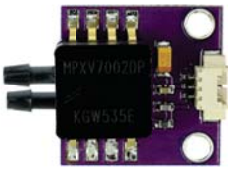

Figure 3.12: Differential pressure sensor [66].

For the electrical power during flight, it is necessary to record the battery voltage and current drawn. A parallel voltage divider is connected to the battery and the output connected to an analog input of Arduino that will calculate the real battery voltage. Relatively high resistors have to be used to limit the current in the analog port of the Arduino; any two resistors that divide the maximum battery voltage to a maximum of 5V can be used. A sketch of the voltage divider used in this equipment is present in Figure 3.13, further specifications as the resistors values and operating limits are present in Table 3.13. The current is measured with an ACS 770 [67], Figure 3.14; it is an analog sensor without a specific library and information is available in the datasheet [67], the principal specifications are described in Table 3.14.

Table 3.13: Voltage divider specifications.

| Technical Specification | |
|---|---|
| Function | Battery Voltage Sensor |
| R1 value | 20 kΩ |
| R2 value | 6.9 kΩ |
| Maximum Battery Voltage | 20 V |

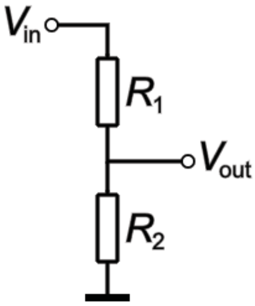

Figure 3.13: Voltage divider for voltage sensing schematic.

Table 3.14: Hall effect current sensor specifications [67].

| Technical Specification | |
|---|---|
| Model | ACS770-50U |
| Max. Current | 50 A |
| Sensitivity | 80 mV/A |
| Supply Voltage | 5 V |
| Mass (with wires) | 34 g |

Figure 3.14: Hall effect current sensor [68].

All data have to be recorded: an SD card was selected. After the flight the SD card is removed and the file is transferred to the computer. A SD card read/writer [69], Figure 3.15, is used. This SD read writer works of digital levels with a voltage of 3.3V, as the digital pins of the Arduino work at 5V, a level shifter [70] is necessary, Figure 3.16, connected between Arduino and the SD card read/writer digital pins. This level shifter lowers the digital input voltage to the supplied voltage through its digital output, supplying the level shifter using the 3.3V Arduino power output, the digital signals are lowered from 5V to 3.3V. The principal specifications of the SD read writer and the level shifter are described in Tables 3.15 and 3.16.

Table 3.15: SD card read writer specifications [69].

| Technical Specification | |
|---|---|
| Model | LC Studio SD Card Read Writer |
| Supply Voltage | 3.3 V or 5 V |
| Digital Levels Voltage | 3.3 V |
| Mass | 10 g |

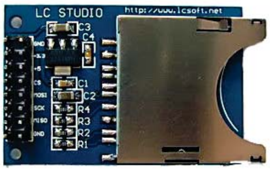

Figure 3.15: SD card read writer.

Table 3.16: Level shifter specifications [70].

| Technical Specification | |
|---|---|
| Model | 74HC4050D |
| Max Input Voltage | 16 V |
| Input/Output Number | 6 |
| Mass | 1 g |

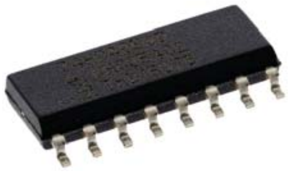

Figure 3.16: Level shifter [71].

The internal space of the fuselage of an airplane is usually limited, carrying this system mounted in a bread board is not an option, carrying it with single wires connected to the sensors and to the board still need more space than needed and would cause bad connections, data recording failure and it is not practical. A printed circuit board (PCB), Figure 3.17, was developed as a shield for the microcontroller board; it has connected on itself the static pressure sensor, the level shifter, the SD card read writer, the voltage divider and single plugs to connect the sensors that can not be attached to the board (GPS, differential pressure and current sensor). With this developed shield, the system becomes more compact, easier to install in the aircraft and more practical to interact with. A 3D printed Polylactic Acid (PLA) case is used to enclose the system and protect it, Figure 3.18. The resultant data acquisition equipment, Figure 3.19 has a total mass of $250g$, it is inexpensive and extremely versatile, it can be easily modified and redundancy could be added. It is easy to implement in any UAV and no configuration is needed, the data is outputted as a comma separated values (CSV) file that is ready to be analyzed and manipulated for the drag polar estimations.

The system, as it is, has a data rate of only $1Hz$, this is due to the microcontroller used and specially to the open source libraries. Particularly, the GPS library is not optimized and is too complex for the requirements of this system. This results in the need of a board with more memory, consequently bigger and heavier, as it is the case of the Arduino Mega2560. The data rate could be increased and the weight of the microcontroller board could be decreased with the development of a new GPS library.

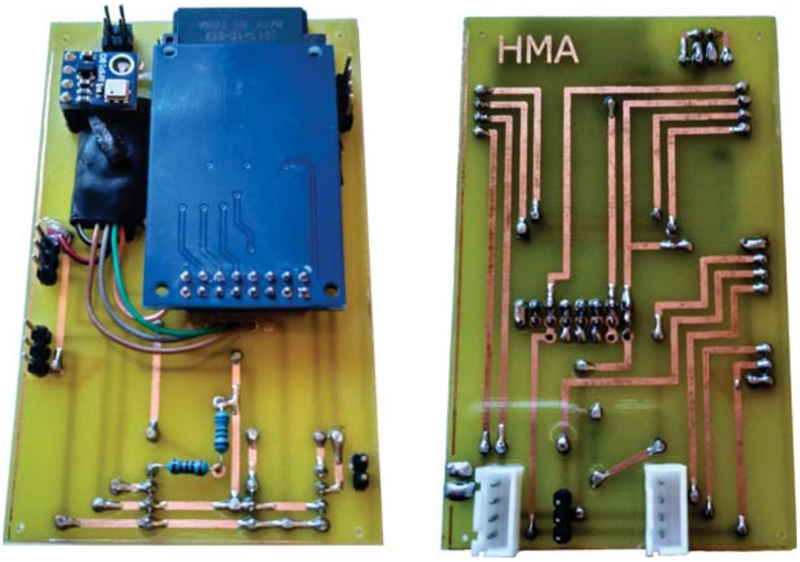

Figure 3.17: Printed circuit board shield for the sensor integration with the microcontroller.

Figure 3.18: 3D printed PLA case for the complete system.

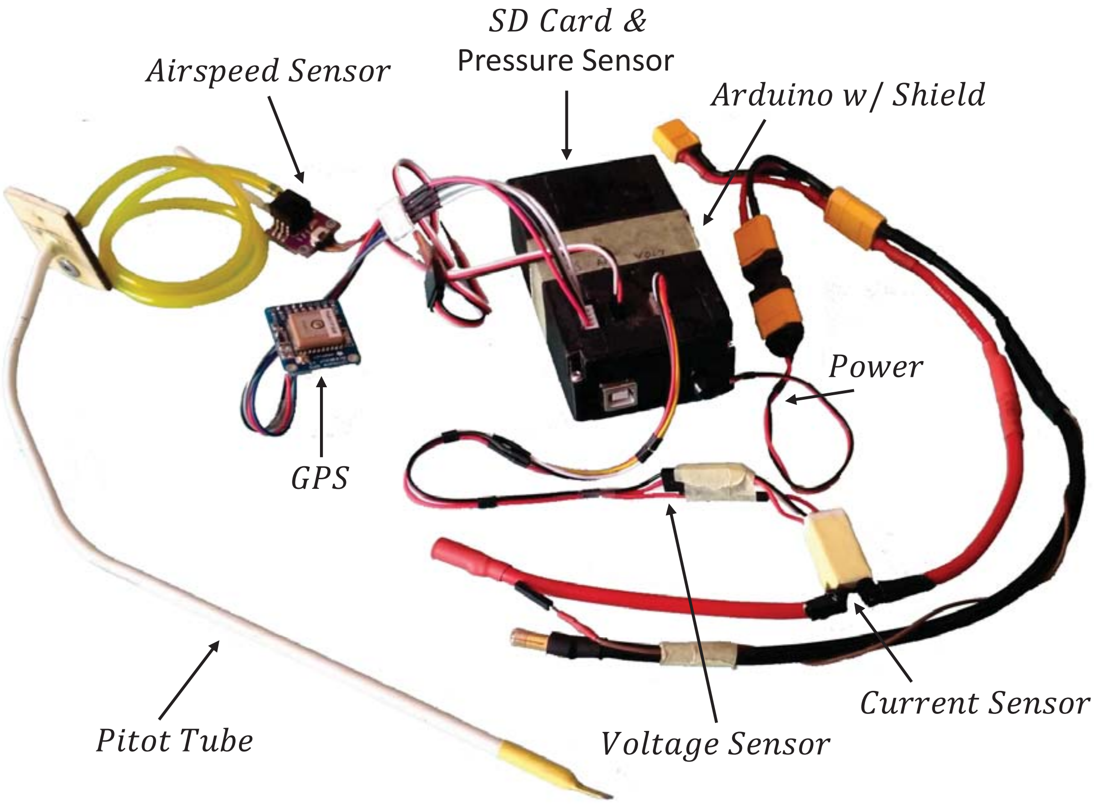

Figure 3.19: Complete data acquisition equipment.

## 3.6 Data Analysis

The data outputted by the equipment has to be analyzed and manipulated so that the methodology can be implemented to estimate the drag polar and thrust curve. All parameters are measured and outputted to a line with a corresponding time in start, so, every second a new set of all parameters is recorded in a line of a file.

The first step is the airspeed calibration, as explained, for the first flight the groundspeed and airspeed should be the same, however, due to the construction, position and alignment of the pitot tube that may not happen. The groundspeed values are plotted against the airspeed ones, the theoretical resultant plot should be a set of points that form a line with the expression $y = x$, the real result is a scatter plot, a linear regression is used in the linear equation $y = mx + b$, that relates the airspeed with the groundspeed, this result is the calibrated airspeed $CAS$, Equation 3.21, where the coefficients $m$ and $b$ are obtained with the linear regression and $V_{AIR}$ is the airspeed.

$$CAS = mV_{AIR} + b \quad (3.21)$$

The second step is to register the pressure and temperature at the field. It was chosen to averaging the measures right before the takeoff.

The third step is to identify the several glides during the entire flight. Due to the procedure used to do the flight tests, the glides happen when the motor and the propeller are stopped. To identify this situation, in the entire flight data, the desired data are the lines when the current draw is zero. The data acquisition is drawing energy from the battery and the motor brake drains some energy too, this current is low, however, at lower currents the sensor is not as precise as it is for higher currents, so it is observed that when the motor is running the minimum current is about $10A$ and that when the motor is stopped, the maximum current registered by the sensor is about $2A$. So, every data line that has a current draw below $2A$ is a glide; it is analyzed and then the drag and lift computed.

The fourth step is to start the drag and lift calculation, it is started with the calculation of the time between each data line $dt$, Equation 3.22. The integer subscript $i$, always indicates the line number; it is used when an equation use multiple data lines (that is parameters from different time instants), $i = 1$ corresponds to the first line of the glide data, $i = 0$ corresponds to the line before the glide is initiated, this line is only used to calculate the first time differential.

$$dt_i = \begin{cases} t_i - t_{i-1}, & if(t_i - t_{i-1}) \geq 0 \\ 60 - t_{i-1} + t_i, & if(t_i - t_{i-1}) \leq 0 \end{cases} \quad (3.22)$$

The fifth step is the calculation of relative and absolute pressure altitude, Equations 3.23 and 3.24, respectively.

$$h_{rel} = \frac{T_f}{\lambda}\left(\left(\frac{p}{p_f}\right)^{-\frac{\lambda R}{g_0}} - 1\right) \quad (3.23)$$

$$h_{abs} = \frac{T_0}{\lambda}\left(\left(\frac{p}{p_0}\right)^{-\frac{\lambda R}{g_0}} - 1\right) \quad (3.24)$$

In Equation 3.23 $T_f$ is the average of the temperature at the field and $P_f$ is the average of the pressure at the field. In Equation 3.24 $T_0$ is reference temperature at sea level for the International Standard Atmosphere (ISA) model, $T_0 = 288.15K$, $P_0$ is the reference pressure at sea level for the ISA model with a value of $P_0 = 101325.0Pa$. The coefficient $\lambda$ is the temperature change with altitude, $\lambda = 6.5 \times 10^{-3}K/m$.

The sixth step is to calibrate the airspeed recorded during the glide with the already obtained calibration line. Although the output of the data acquisition system is the airspeed, the sensor outputs the pressure differential $\Delta P$, the airspeed is calculated with the Equation 3.25.

$$V_{AIR}^2 = \frac{2(\Delta P)}{\rho_0} \quad (3.25)$$

The seventh step is to apply a filter to the acquired data. All experimental data have noise associated with it. At the flight tests, usually there are not fast changes in the measured parameters, if this happens, probably it is noise. So, it was tested a filtering methodology to reduce the noise and the instability in the measurements. This filter is applied to the calibrated airspeed and the relative altitude, Equation 3.26 describes the filtering methodology used.

$$h_{fil} = \frac{1}{4}h_{i-1} + \frac{1}{2}h_i + \frac{1}{4}h_{i+1} \quad (3.26)$$

The eighth step is the airspeed correction with the altitude, to calculate the true air speed $TAS$. First it is necessary to calculate the air density with Equation 3.27, after that, the $TAS$ is calculated with Equation 3.28.

$$\rho = \frac{p}{RT} \quad (3.27)$$

$$TAS = CAS\sqrt{\frac{\rho_0}{\rho}} \quad (3.28)$$

The ninth step is to calculate the three needed derivatives, altitude, vertical velocity and true air speed, the three are calculated the same way, Equations 3.29, 3.30 and 3.31.

$$\dot{h_i} = \frac{h_i - h_{i-1}}{dt} \quad (3.29)$$

$$T\dot{A}S_i = \frac{TAS_i - TAS_{i-1}}{dt} \quad (3.30)$$

$$\ddot{h_i} = \frac{\dot{h_i} - \dot{h_{i-1}}}{dt} \quad (3.31)$$

The tenth and last step is to calculate the drag and lift for each data line, Equations 3.7 and 3.9 and the drag and lift coefficients, Equations 3.12 and 3.11.

Before obtaining the drag and lift points to estimate the drag polar, attention must be paid to the altitude variation of each glide, sometimes, due to the piloting, especially at the beginning of the glide, the airplane oscillates and instead of a steady glide, it gains and loses altitude repeatedly, this type of glides is not adequate to consider for the drag polar estimation.

After obtaining the experimental drag and lift points, the data has to be analyzed and processed, it is necessary to fit the data with curves to estimate the drag polar, the symmetric parabolic drag polar or other adequate drag polar. The deviation and uncertainty of the measurements have to be calculated too.

The first step is to confront the experimental data with the expected results and typical results for a similar system, in this case the drag polar of an aircraft. The reliability of the data and outliers are delicate subjects, the number of points and their distribution also influence their reliability.

As presented in Section 2.3.2, to obtain the symmetrical drag polar, the drag coefficient is plotted against the square of the lift coefficient and the data is fitted with a linear equation to obtain the zero-lift drag coefficient $C_{D_0}$ and the induced drag factor $K$. However, the symmetrical drag polar is only an approximation of the real airplane drag polar. In some cases, this approximation can lead to a drag polar that is not adequate to describe the real drag polar of the aircraft.

### 3.6.1 Bins Division and Outliers

To better process and analyze the experimental data, it is divided in several bins, those are small groups of several points where the experimental coefficients are averaged to simplify the visualization and describe the results of the system. This division in bins allows the calculation of the standard deviation and a curve fitting to obtain the drag polar. For each bin the dispersion can be evaluated and it is possible to understand how the data is distributed around the mean. The number of points of each bin can also be a parameter to understand if they are reliable. It is observed that for each bin, the drag coefficient points are close to a normal distribution. Given this distribution and observing Figure 3.20, a criteria is formulated to exclude outlier points. All the drag coefficient or glide ratio points whose value is outside a 99.99% confidence interval, are considered outliers and excluded from the data set, this is done with the average $\bar{x}$ and standard deviation $\sigma$ of each bin, excluding the points that have a value lower than $\bar{x} - 4\sigma$ and higher than $\bar{x} + 4\sigma$. With this procedure, the average of each bin is changed when excluding the outliers, the same procedure is applied to the new data points and it is repeated until the average is not changed, that is, there are not more outliers to exclude.

Before the next procedure regarding the data analysis, that would be a curve fitting, it is necessary to carefully analyze the drag and glide ratio results. As already referred several times during this work, especially for performance flight testing, there is not much literature available and, in the few available works, the following point, in Section 3.6.2, is not discussed.

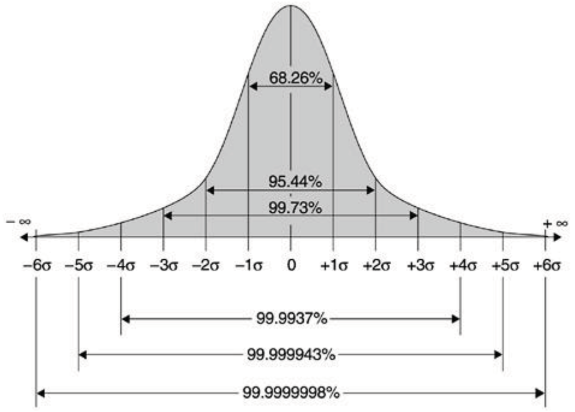

Figure 3.20: Probability for a normal distribution curve [72].

With the methodology described in Section 3.4, the drag and lift values, as well as their coefficients are experimentally obtained and the glide ratio can also be obtained right away for each lift coefficient value. The next step is the bins division, averaging these results and exclude the outliers to obtain a meaningful data to compare both configurations.

### 3.6.2 Erroneous Approach

One approach to obtain the $C_L/C_D$ that may seem reasonable, would be to use the bins average of the $C_L$ and $C_D$ values and divided them to obtain the glide ratio. However, there is a difference between the glide ratio that is obtained with the average of the glide ratio values for each experimental point and the glide ratio that is obtained with the average of the lift coefficient divided by the average of the drag coefficient. The glide ratio values obtained from the averages of the lift and drag coefficients is around 20% lower than the values obtained from the glide ratio of each point. To understand this effect and which methodology is correct to obtain the glide ratio values, the following exercise is made:

Considering the arbitrary drag and lift coefficients represented in the plot of Figure 3.21, each point has a corresponding glide ratio, the same points and glide ratio values are in Table 3.17. If all the values are averaged, a $C_L/C_D = 6.11$ is obtained for the glide ratio points average and if the $C_L$ average is divided by the $C_D$ average a $C_L/C_D = 5$ is obtained. This result for this simple example is the same result obtained for the entire experimental points. To understand which glide ratio is correct, this result has to be analyzed from a performance point of view. In Figure 3.22 the glide path of an aircraft that during a single glide experienced three different moments with different experimental glide ratio and drag values is represented. At a first moment with a $C_L = 1$ and a $C_D = 0.1$, the glide ratio for these values is $C_L/C_D = 10$ and as it is only one point the problem with the averages does not occur; in a second moment the aircraft flies with a $C_L = 1$ and a $C_D = 0.2$, the glide ratio for this values is $C_L/C_D = 5$; in the third moment the aircraft flies with a $C_L = 1$ and a $C_D = 0.3$, the glide ratio for this values is $C_L/C_D = 3.33$. Each moment lasts enough time for the aircraft to lose 1 meter in altitude which corresponds to a traveled distance of 10 meters for the first moment, 5 meters for the second, 3.33 meters for the third moment and 18.33 meters for the total distance. These are the real glide ratios and distances for that single glide. To represent this single glide in one point, the real glide ratio value has to be $C_L/C_D = 6.11$ so that in 3 vertical meters, a distance of 18.33 meters is traveled. This concludes that to represent the data well, the average of the glide ratio for each experimental point should be used. These are the values that should be fitted with an adequate curve to represent the drag polar of the aircraft.

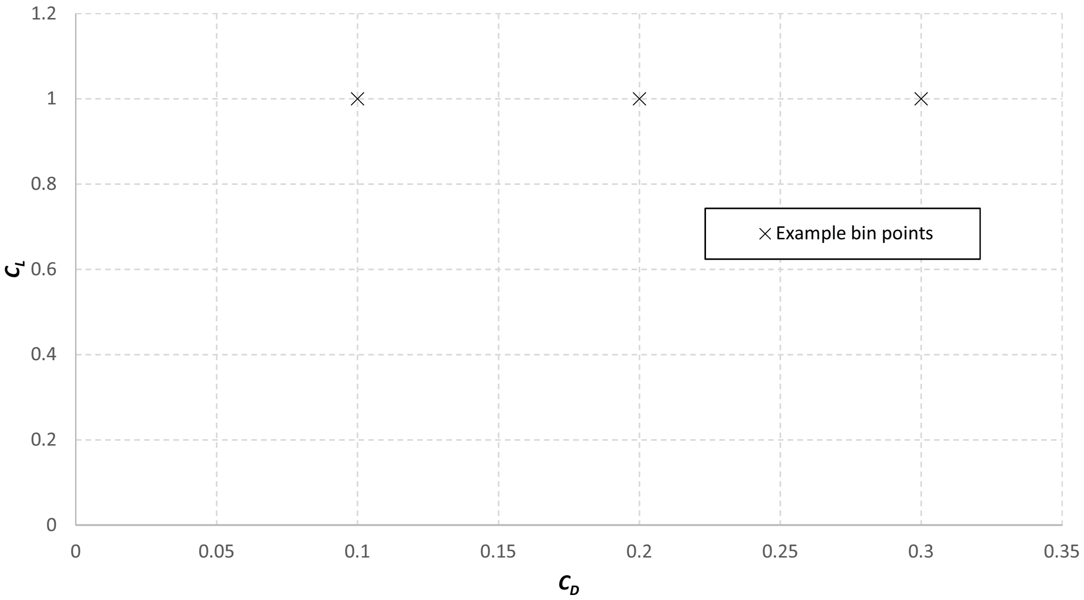

Figure 3.21: Example of lift and drag coefficients points in one bin divison.

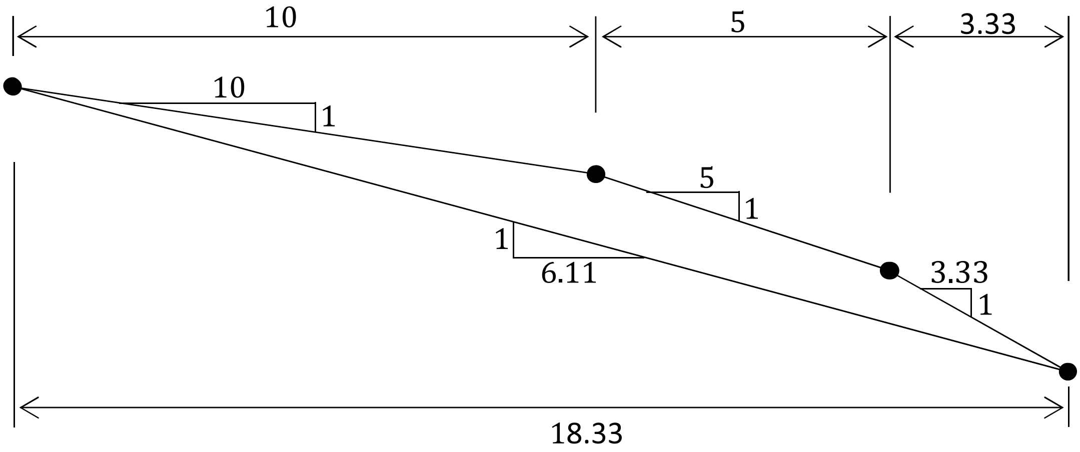

Figure 3.22: Glide path example for the example bin points.

Table 3.17: Example lift and drag coefficients points with their glide ratio value and the glide ratio for the erroneous approach.

| points | $C_L$ | $C_D$ | $C_L/C_D$ |
|---|---|---|---|
| 1 | 1 | 0.1 | 10 |
| 2 | 1 | 0.2 | 5 |
| 3 | 1 | 0.3 | 3.33 |
| average | 1 | 0.2 | 6.11 |
| $\frac{average C_L}{average C_D}$ | 5 | | |

### 3.6.3 Performance Analysis

After estimating the drag polar of the aircraft, it is possible to calculate the drag of the aircraft for any velocity and applying Equation 3.13, the available thrust for each data line can be calculated. At the same time, the electrical power is also calculated with the Equation 3.16. The resultant data points allow the estimation of the thrust curve as a function of the velocity. Knowing this curve and the previous calculated electrical power, it is now possible to calculate the available power with Equation 3.14, and with Equation 3.15 the propulsive efficiency can be calculated too. The propulsive efficiency result is also a scatter plot that has to be fitted with a curve to estimate the equation of the propulsive efficiency. The propulsive system, battery, motor and propeller are the same used in the ACC competition, there are already several wind tunnel tests for this propulsive system by other universities; the results obtained with this method are compared with these previous wind tunnel tests.

At this point, the drag polar and thrust curves are known. The plot present in Figure 2.22 can be obtained for this specific aircraft, both configurations can be compared and all the performance parameters described in Section 2.3.1 can be calculated.

### 3.6.4 Energy Method and Methodology Tests

The filtering technique used with the measured parameters, the vertical acceleration to correct the lift and the energy methodology that accounts for the change in the airspeed instead of only the vertical speed as in the alternative methods, were also tested to understand their influence in the dispersion of the results. One of the flights was analyzed in five different ways, one way with the already described methodology, that is called ”energy method”. In the second way, the filter applied with the Equation 3.26 is not used, this is called ”without filtering”. In the third way, instead of calculating the lift with Equation 3.11, the weight of the aircraft is directly used, this is called ”without $C_L$ correction”. In the fourth way, the calculated drag is done in the conventional way without considering the changes in airspeed, that is, considering a constant airspeed, with Equation 3.32, this is called ”constant speed assumption”. In the last way, all the corrections were not used, the aircraft weight is used directly to calculate the $C_L$, the filter is not used and the simplified Equation 3.32 is also used; this is methodology is called ”without correction”. The methodology used to analyze the influence of this change in the results was the same for every alternative method. The alternative methodology is plotted together with the energy method to visually evaluate the results in the drag polar. Then, the data points are divided in bins of 50 points, the drag and lift coefficients are averaged and the standard deviation for the drag coefficient of each bin is calculated. Just with the standard deviation values it is possible to analyze the influence of these corrections. However, the standard deviation changes for each bin, increasing and decreasing consecutively, so, the standard deviation points are fitted with a polynomial regression as a function of the lift coefficient. The averaged drag coefficient is added and subtracted by the result of the polynomial regression to obtain ranges of the dispersion. These superior and inferior dispersion limits, are plotted together with the data points to understand how the results are affected with the several methodologies used.

$$D = -\frac{\dot{h}W}{V} \quad (3.32)$$

### 3.6.5 Uncertainty Analysis

The uncertainty of each measurement equipment used is known, however their influence in the final result has to be calculated. Considering that the desired result $R$ is a function of raw primary measurements $a$, $b$, $c$, ..., that are mathematically independent with a known uncertainty [73], Equation 3.33, the uncertainty in $R$ that results from the uncertainties in $a$, $b$, $c$, ..., can be calculated with Equation 3.34. The final uncertainty is calculated with the several changes in the result induced by a change in the primary measurements due to their uncertainty.

$$R = f(a, b, c...) \quad (3.33)$$

$$\delta(R) = \sqrt{\left(\frac{\partial R}{\partial a}\delta(a)\right)^2 + \left(\frac{\partial R}{\partial b}\delta(b)\right)^2 + \left(\frac{\partial R}{\partial c}\delta(c)\right)^2 + ...} \quad (3.34)$$

# Chapter 4

# Results and Discussion

## 4.1 Flight Testing Campaign Overview

During the flight testing campaign, a total of 20 flights were conducted, with 7 valid flights for the WTT configuration and 8 valid flights for the conventional configuration, usually the flight tests started around 6:30AM and ended a little before 9:00AM. A little over 6.5 hours of flight time were accumulated with an average of 19.65 minutes per flight and a maximum flight time of 30 minutes that happened twice for the WTT configuration. Between both configurations, 258 glides were made with 215 valid ones. For the climb analysis, 98 valid climbs were realized.

### 4.1.1 Flight Handling of Configurations

The handling characteristics of both configurations are important to be evaluated. Creating a new concept aircraft might work in theory but handling problems may appear.

It was already described in Chapter 3 that to fly the conventional configuration comfortably, some changes had to be made to this configuration. To solve the dutch roll problem, the vertical tail surface had to be increased. Although the problem was solved and the aircraft could be flown with relative ease, it was not as precise as the WTT configuration during turns. A big change between both configurations is the $CG$ position, the WTT configuration was easily flown and ”trimmed” for the glide tests with the $CG$ at 20% of the MAC, but for the conventional configuration, the $CG$ had to be changed to 30% of the MAC in order to have the possibility to ”trim” the aircraft for the glide tests. It was not the only cause, but changing the $CG$ position, made the climb tests more difficult. The aircraft would tend to rotate, decrease the airspeed and end in a stall. From the piloting point of view, controlling the aircraft in this situation is extremely uncomfortable, requiring more attention and increasing the work load for the pilot. Although both configurations required attention to the airspeed before initiating the glide, to prevent the aircraft from oscillating and gaining and losing altitude repeatedly, the conventional configuration required more attention and was harder to initiate a good glide, especially at lower airspeeds.

On the other hand, the WTT configuration was easily flown during the several tests, the previous problem with the control reversal did not occur with this wing structure and the airplane was almost ”self piloted” decreasing the work load during the flight tests. Not only this configuration is overall easier to fly, but especially at lower airspeeds. Unlike the conventional configuration that usually ended unintentionally stalling several times during a single flight, the WTT would not stall unintentionally and the stalls were gentle and controllable. Although this effect was noticed later in the flight test campaign and it was not further investigated, after reviewing some flights, it was noticed that maybe even after the stall, the tail surfaces still provided control to the aircraft which would result in a controllable deep stall.

### 4.1.2 Uncertainty Analysis

Dispersion in the results of an experimental test is inevitable, and in this particular study, the dispersion is considerably large. An uncertainty analysis must be conducted, it makes possible to understand how the different components of the systems affect the final result and to calculate the uncertainty value of the final result. Following the methodology described in Section 3.6.5, Table 4.1 summarizes the uncertainty analysis and Table 4.2 has the uncertainty results for the final values and the uncertainty that each measurable parameter induces in the final result. The experimental drag values have an uncertainty of 22.6% and the experimental drag coefficient values have an uncertainty of almost 24%. From Table 4.2, it is observed that the main uncertainty comes from the perturbation in the primary variable $d$, which is the airspeed measurement. The uncertainty of the airspeed sensor used for the total uncertainty calculation, is the one present in the datasheet of the sensor [65], 2.5%. However, as referred in [74], it is expected to have less uncertainty at higher airspeeds, this can be confirmed with the lower dispersion of the results for lower $C_L$ values and higher dispersion for lower airspeeds, that is, higher $C_L$ values, 4.2. This is one of the limitations of the current work, but there is a potential to reduce the uncertainty by changing to a better, digital differential pressure sensor [75], with an error of less than 1.0%

Table 4.1: Uncertainty analysis summary.

| Primary measurements | Primary variable | Quantity | Primary uncertainty | Perturbation | Perturbated value |
|---|---|---|---|---|---|
| Time (GPS) [s] | a | 1.016 | 4E-08 | a+da,b,c,d,e,f,g,h,i | 1.016 |
| Temperature [K] | b | 304.650 | 0.10 | a,b+db,c,d,e,f,g,h,i | 304.750 |
| Pressure i [Pa] | c | 94795.210 | 1.00 | a,b,c+dc,d,e,f,g,h,i | 94796.210 |
| Differential Pressure i [Pa] | d | 75.602 | 2.5% | a,b,c,d+dd,e,f,g,h,i | 77.492 |
| Mass [kg] | e | 4.002 | 1E-03 | a,b,c,d,e+de,f,g,h,i | 4.003 |
| Pressure@field [Pa] | f | 96387.803 | 1.00 | a,b,c,d,e,f+df,g,h,i | 96388.803 |
| Temperature@Field [K] | g | 302.830 | 0.10 | a,b,c,d,e,f,g+dg,h,i | 302.930 |
| Differential Pressure i-1 [Pa] | h | 81.709 | 2.5% | a,b,c,d,e,f,g,h+dh,i | 83.752 |
| Pressure i-1 [Pa] | i | 94787.500 | 1.00 | a,b,c,d,e,f,g,h,i+di | 94788.500 |

Table 4.2: Uncertainty analysis results.

| | D [N] | CD |
|---|---|---|
| Final Result | 4.2428061 | 0.0818215 |
| Uncertainty | 0.9581173 | 0.0196209 |
| Uncertainty, % | 22.58 | 23.98 |
| Primary uncertainty, % | | |
| a+da,b,c,d,e,f,g,h,i | 3.94E-06 | 3.94E-06 |
| a,b+db,c,d,e,f,g,h,i | 0.002 | 0.002 |
| a,b,c+dc,d,e,f,g,h,i | 7.370 | 7.370 |
| a,b,c,d+dd,e,f,g,h,i | 14.251 | 16.376 |
| a,b,c,d,e+de,f,g,h,i | 0.025 | 0.025 |
| a,b,c,d,e,f+df,g,h,i | 1.22E-06 | 1.22E-06 |
| a,b,c,d,e,f,g+dg,h,i | 0.019 | 0.019 |
| a,b,c,d,e,f,g,h+dh,i | 14.079 | 14.079 |
| a,b,c,d,e,f,g,h,i+di | 7.371 | 7.371 |

## 4.2 Airspeed and Pitot Tube Calibration

Airspeed undoubtedly is an important variable, and its reading should be as accurate as possible. The result of the calibration of the differential pressure sensor and pitot tube, with the help of a GPS receiver, is present in Figure 4.1. From the scatter plot in Figure 4.1 or from the resultant calibration line, it is possible to see that the indicated airspeed is very close to the groundspeed output from the GPS receiver. The obtained calibration line is applied to the indicated airspeed values of this and the following flights to obtain the calibrated airspeed (CAS).

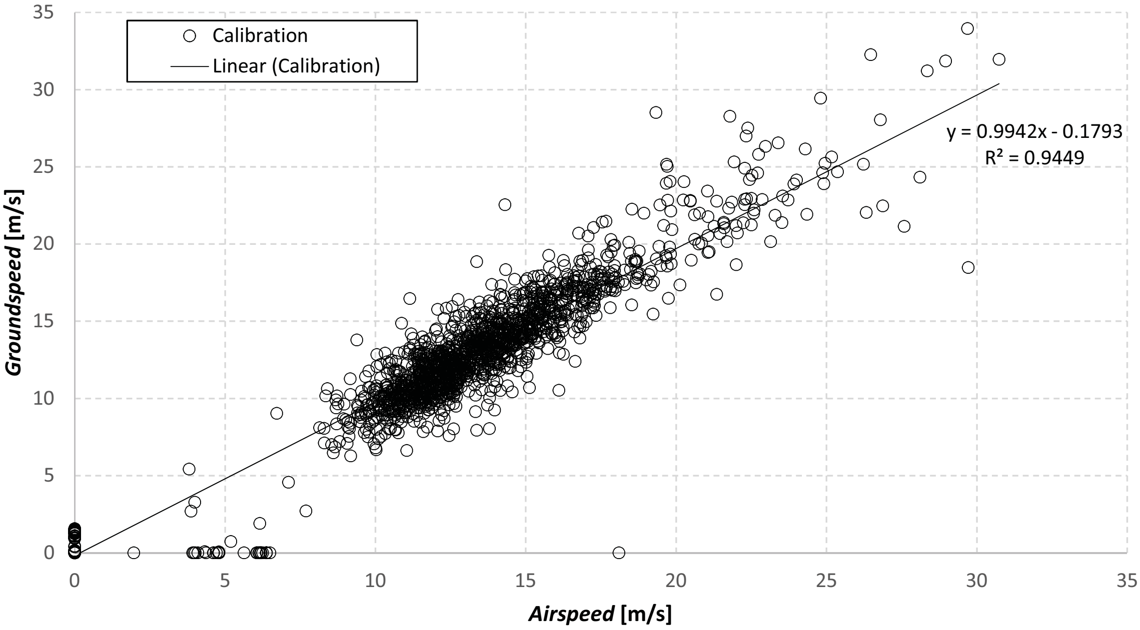

Figure 4.1: Airspeed calibration line.

## 4.3 Flight Testing Results - Glides

The flight testing results, for both the WTT and conventional baseline configurations, with the methodology described for the drag polar determination is in the scatter plot of Figure 4.2; the typical dispersion of an experimental test is well present and it increases with the lift coefficient. Observing the plot, the drag coefficient for both configurations is roughly in the same regions. It is important to notice that towards the end of the lift coefficient range, there are just a few points and with higher dispersion, for the conventional configuration there is a group of points with a lower $C_D$ than for the previous $C_L$ values; for the WTT configuration there ia a group of points with an extremely high $C_D$ value when compared with the values for the previous $C_L$. These values at the end of the $C_L$ range, with high dispersion, low number of points and with values that do not follow what would be expected for the drag of an airplane, are removed from the data. The fact that they are just a few and in a region where it is difficult to fly, near the stall speed, will not affect the results neither the conclusions of this work.

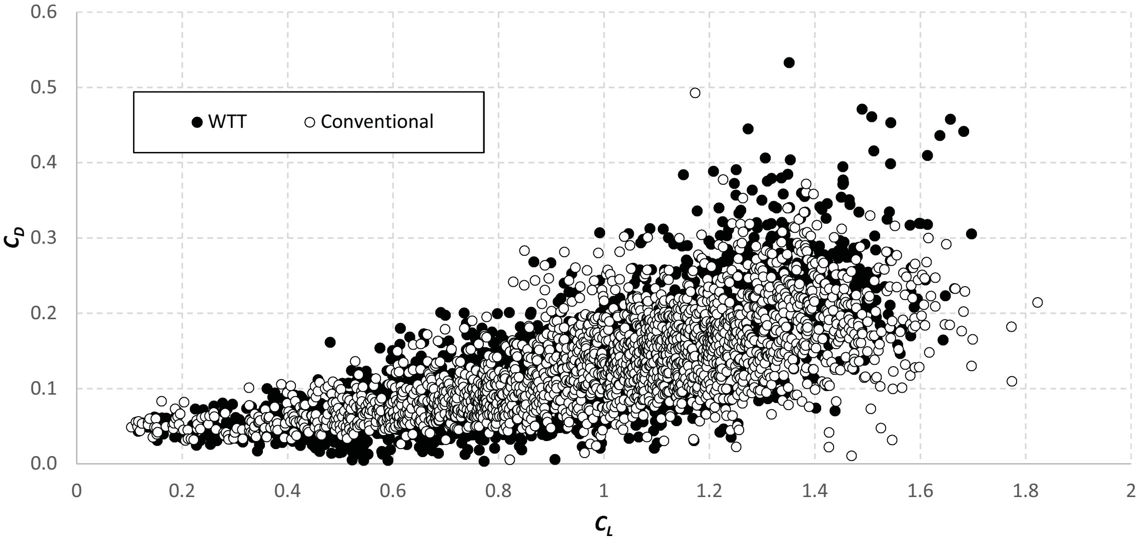

Figure 4.2: Plot of the experimental $C_D$ and $C_L$ for both configurations.

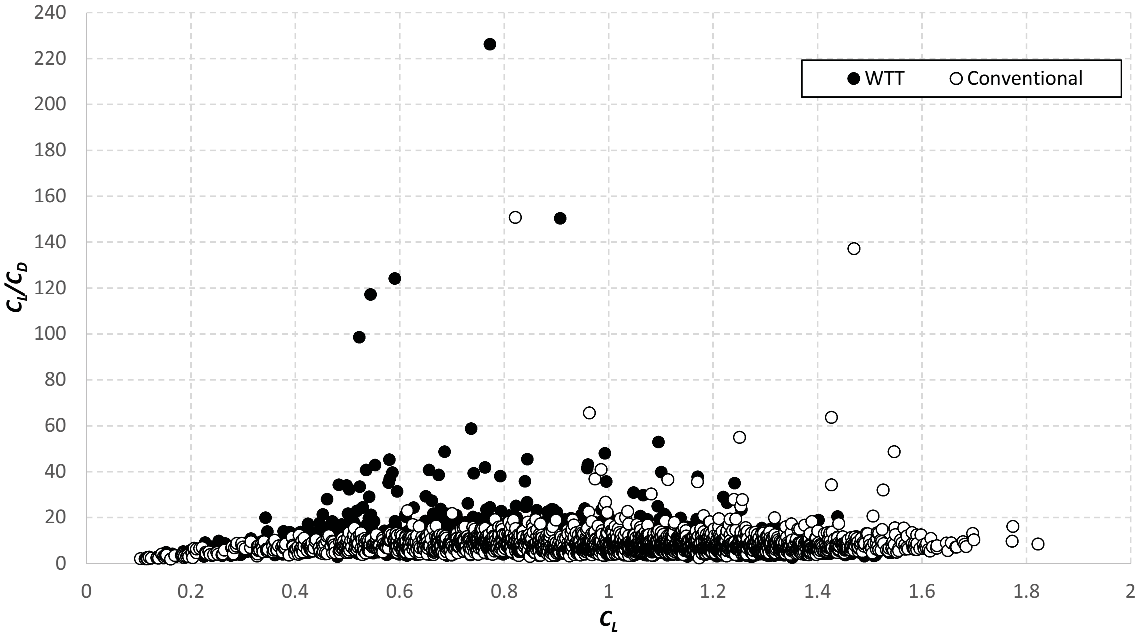

Figure 4.3: Plot of the experimental glide ratio values against the lift coefficient for both configurations.

Both configurations can be better compared through the glide ratio plot; for each point, the lift coefficient is divided by the drag coefficient to obtain the glide ratio. Some of the lower $C_D$ values result in extremely high glide ratio values; this result is present in Figure 4.3; These high glide ratio values affect the visualization of the results.

In Figure 4.4, exactly the same values are plotted, however the vertical axis maximum value is limited to 60. To further enhance the graphical representation of the results, this limit is halved, and taking advantage of the marker style used for the conventional configuration in Figure 4.4, that allows to visualize the points density by the darker areas. The glide ratio for both configurations is plotted separately. In Figure 4.5 the glide ratio for the WTT configuration is plotted and in Figure 4.6 the glide ratio for the conventional configuration is plotted.

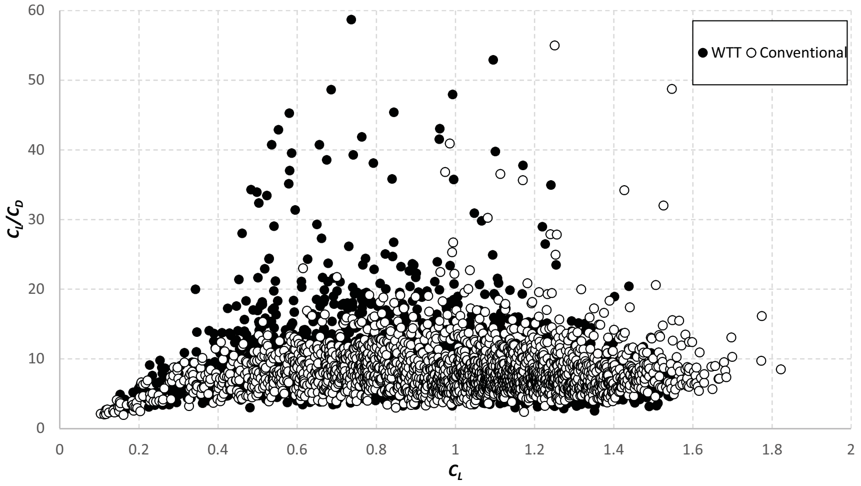

Figure 4.4: Plot of the experimental glide ratio values, limited to a maximum value of 60, against the lift coefficient for both configurations.

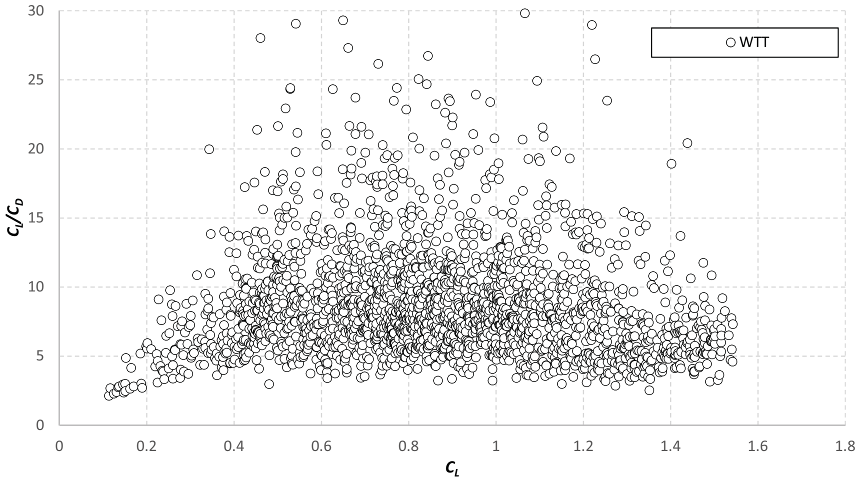

Figure 4.5: Plot of the experimental glide ratio values, limited to a maximum value of 30, against the lift coefficient for the WTT configuration.

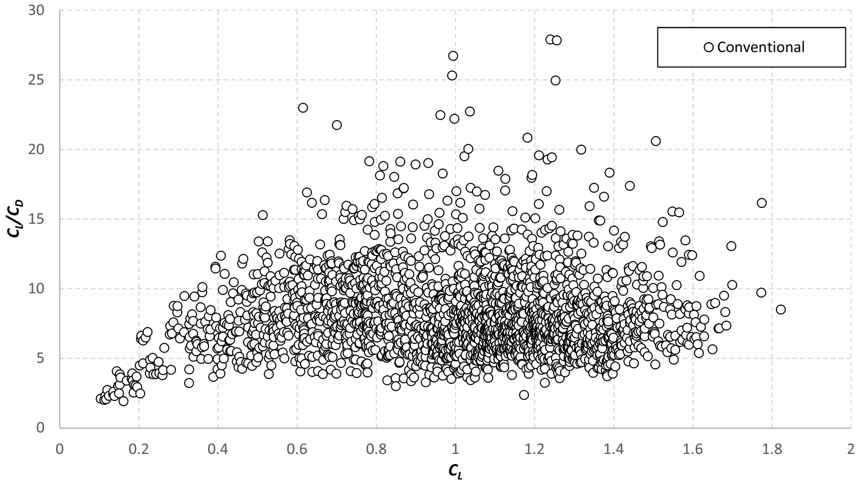

Figure 4.6: Plot of the experimental glide ratio values, limited to a maximum value of 30, against the lift coefficient for the conventional configuration.

The glide ratio values are important to compare both configurations and this methodology with others. These glide ratio values have a good correlation because for each $C_D$ point it is used the respective $C_L$ value; this does not happen if the bins are applied to the drag coefficient values, and the $C_D$ average is used with the $C_L$ average for that bin to obtain the glide ratio values, this effect is further explained in Section 4.3.2. This way, the methodology described in Section 3.6 to exclude the outlier points, is applied to the glide ratio values data and the results for each configuration are present in Figures 4.7 and 4.8, for the WTT and conventional configuration respectively, where the excluded points can be seen. The effect on the glide ratio average for each bin, after the iteration of this methodology, is present in Figure 4.9 for the WTT configuration and in Figure 4.10 for the conventional configuration. For both plots in Figures 4.7 and 4.8, although the extremely high values are not shown, obviously they are considered outliers. For the WTT configuration, the number of outlier points is higher than for the conventional configuration and they occurred for a wide range of $C_L$. For the conventional configuration, the number of outlier points is lower and they mostly occur at higher $C_L$ values. From the plots of the bins average, Figure 4.9 for the WTT configuration, the number of outlier points across a wide range of $C_L$ values is well evident, as the resultant average, after excluding these outlier points, was lowered almost for every $C_L$ value, the biggest change was in the region where there were four outlier points with a glide ratio value above 95. These values would cause a spike in the glide ratio average that with this outliers methodology disappeared. For the conventional configuration, Figure 4.10, the average is lowered mostly for $C_L$ values between 0.8 and 1. The final plot after excluding the outliers for both configurations, that allows the comparison between both configurations, is present in Figure 4.11. Removing the outliers points resulted in a maximum glide ratio value of around 25 for the WTT configuration, and it can be seen that only this configuration reached the higher glide ratio values between 20 and 25.

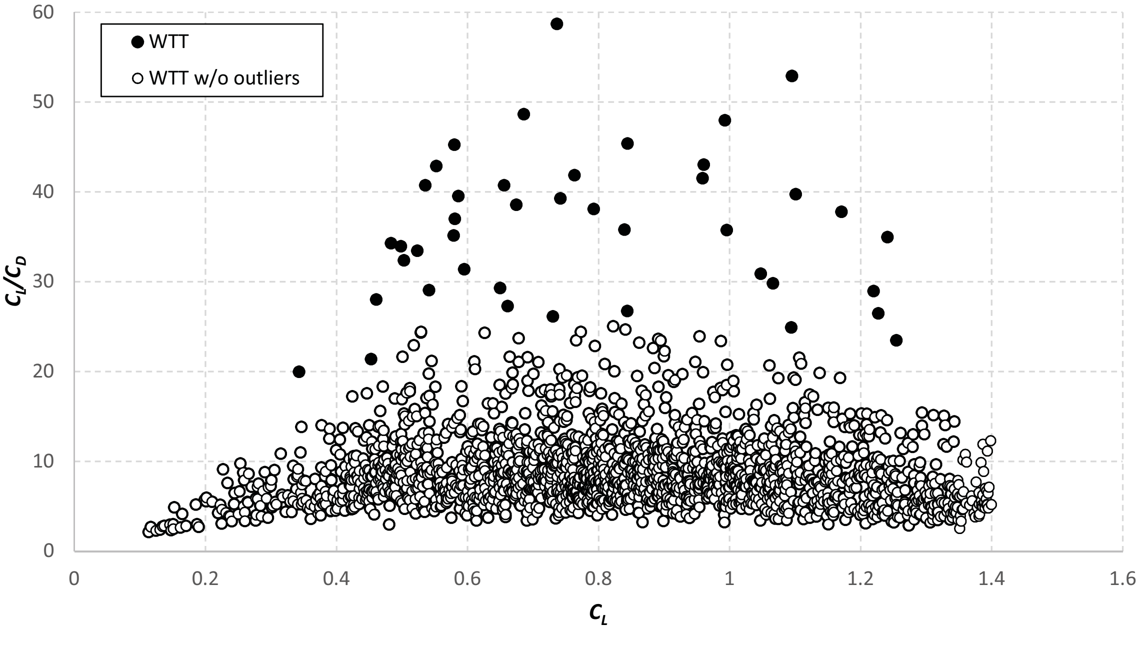

Figure 4.7: Plot of the experimental glide ratio values, limited to a maximum values of 60, before and after removing the outlier points for the WTT configuration.

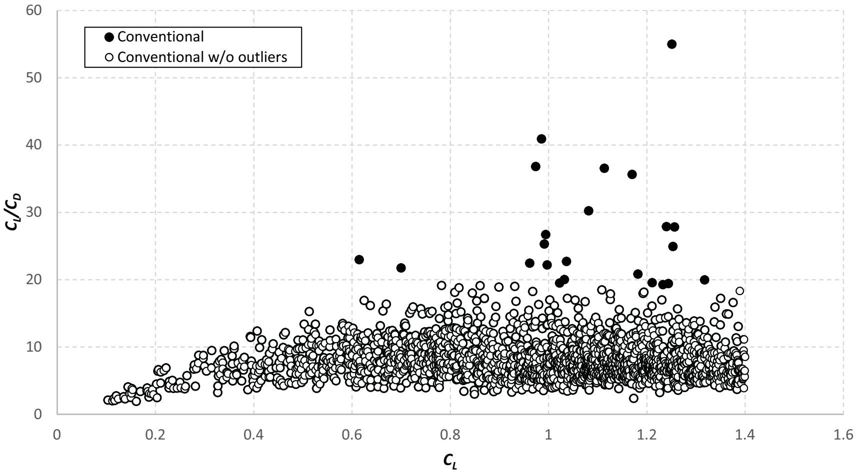

Figure 4.8: Plot of the experimental glide ratio values, limited to a maximum values of 60, before and after removing the outlier points for the conventional configuration.

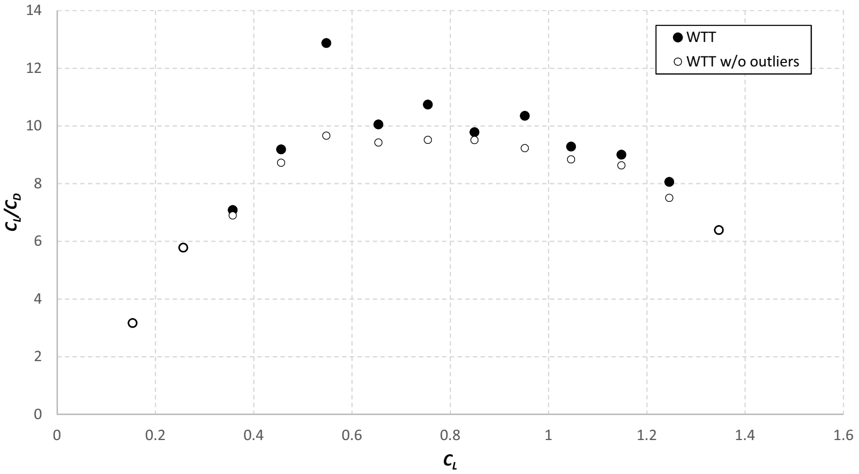

Figure 4.9: Plot of the glide ratio average values before and after removing the outlier points for the WTT configuration.

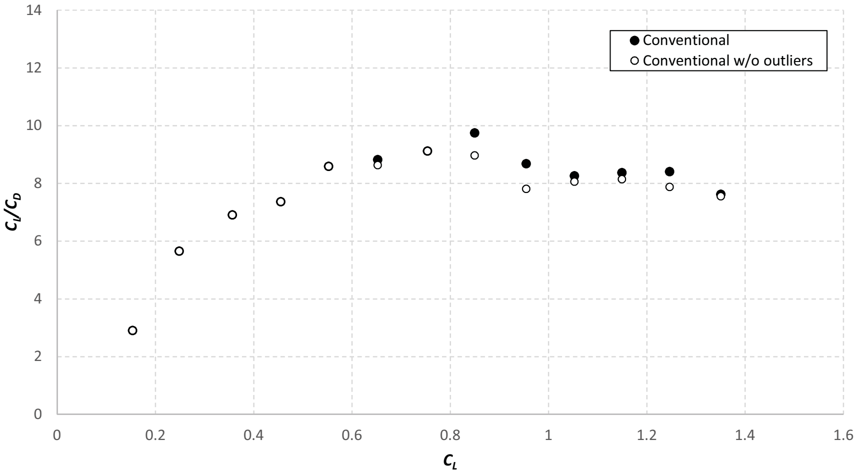

Figure 4.10: Plot of the glide ratio average values before and after removing the outlier points for the conventional configuration.

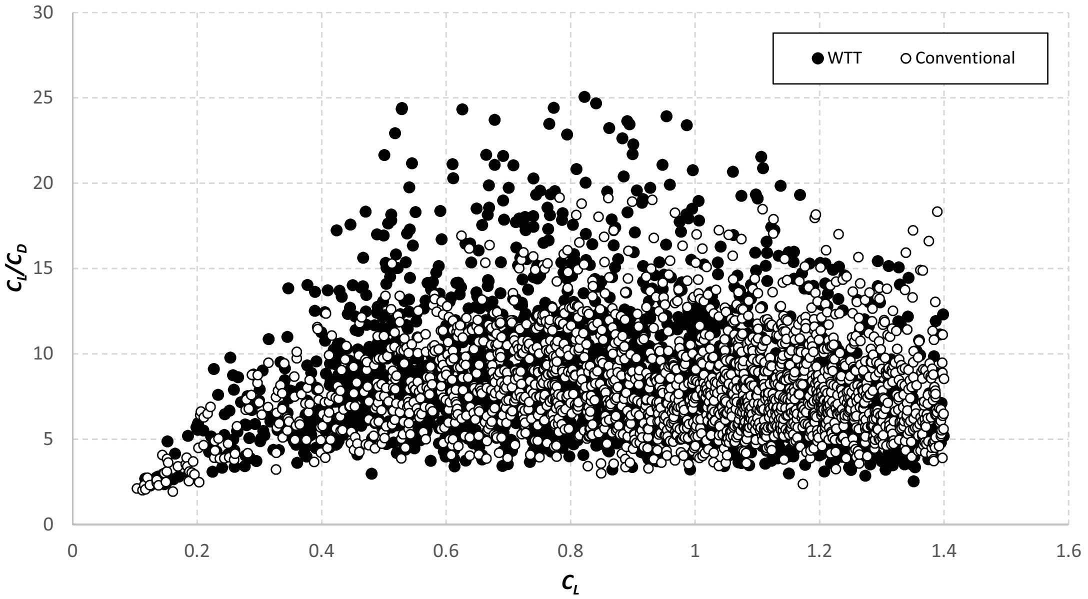

Figure 4.11: Plot of the experimental glide ratio values after removing the outlier points for both configurations (without any limit at the vertical axis).

After the bins division and removing the outliers, the standard deviation for the experimental lift and drag coefficients can be calculated. Figure 4.12 is the plot for the standard deviation of the drag and lift coefficients, for both configurations, along the $C_L$ range. The standard deviation absolute value for the lift coefficient remains approximately constant for every $C_L$ value and has about the same value for both configurations; this means that the relative standard deviation decreases with the $C_L$. In the case of the drag coefficient, the standard deviation increases with the $C_L$ value, as expected due to the increasing dispersion. For the WTT configuration, the relative standard deviation stays close to constant and for the conventional configuration, for lower $C_L$ values the deviation is considerably higher than for the WTT configuration, but the value decreases with the lift coefficient being lower than the ones for the WTT configuration for the higher $C_L$ values.

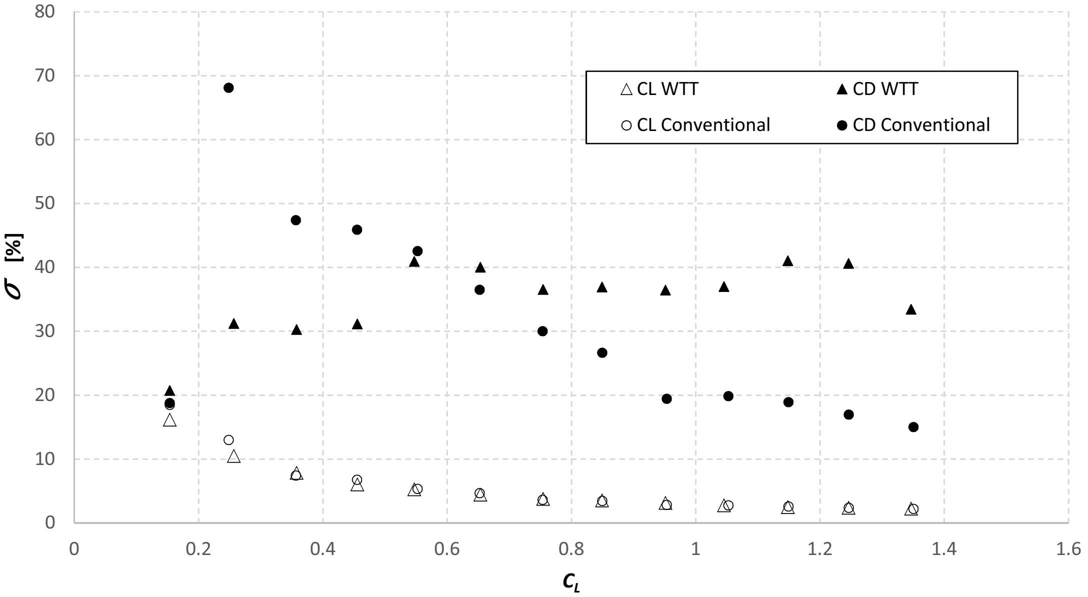

Figure 4.12: Standard deviation for the drag and lift coefficients for both configurations.

The typical experimental drag polar that results from the bins division, with the respective standard deviation for each bin, for the WTT configuration, is present in Figure 4.13. This result can be compared with the result obtained from Ostler [49], Figure 4.14, for the flight testing of his small flying wing. As already stated several times during this work, there is not much complete information about flight testing small UAVs. This plot from Ostler shows that, high results dispersion that results in a high standard deviation is usual for flight testing of small UAVs for performance estimation.

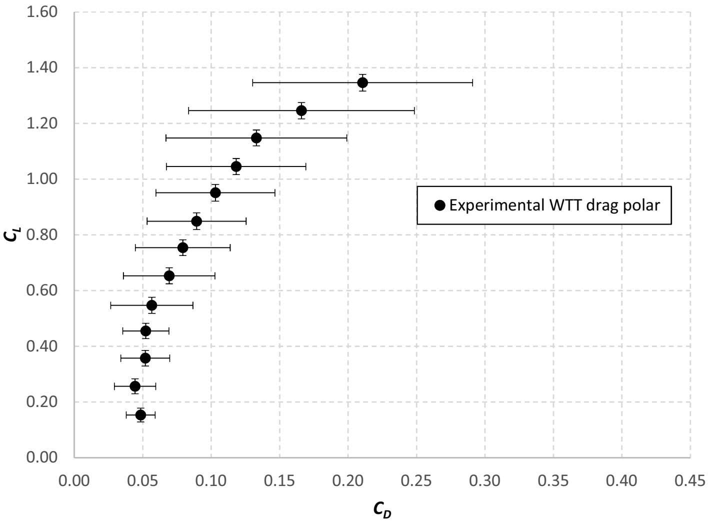

Figure 4.13: Experimental drag polar plot and standard deviation for the WTT configuration.

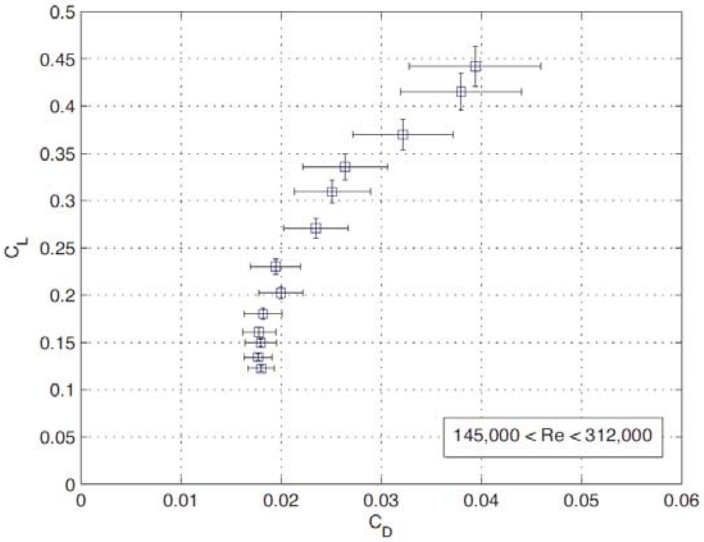

Figure 4.14: Experimental drag polar of the Unicorn UAV [49].

The bins division and the respective glide ratio average result, for both configurations, is present in Figure 4.15. This plot is the best suited to summarize the experimental work; both configurations can be compared. The same data can be used to plot the $C_D$ instead of the $C_L/C_D$, the conclusions are the same, however the difference between both configurations is more noticeable in the glide ratio plot.

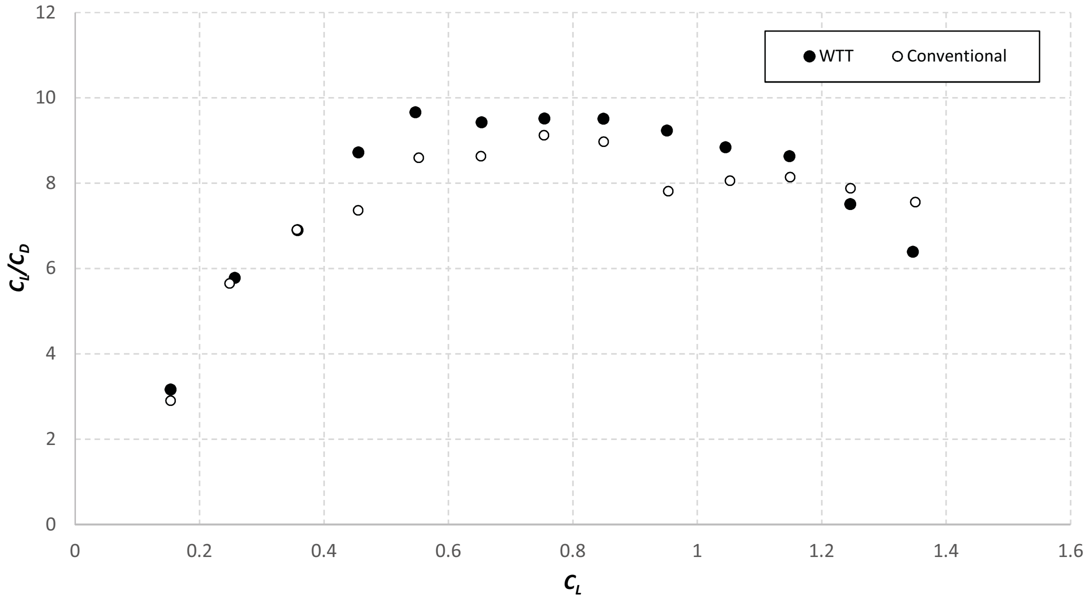

Figure 4.15: Plot of the experimental glide ratio average values for both configurations comparison.

The symmetrical parabolic drag polar, not only does not fit the data well as the methodology described in Section 2.3.2 to obtain it, in this study, tends to overestimate or underestimate the zero-lift drag coefficient which results in an erroneous induced drag factor $K$.

The plot in Figure 4.15 is the one used to curve fit an adequate drag polar. The asymmetrical parabolic drag polar is used, Equation 4.1. The $C_{D_{min}}$ and the $C_{L_{CDmin}}$ coefficients are easy to determine as they are the lowest drag coefficient value in Figure 4.13 and the respective lift coefficient. The induced drag factor $K$ is determined minimizing the error between the asymmetrical drag polar and the data points with the least square method.

$$C_D = C_{D_{min}} + K(C_L - C_{L_{CDmin}})^2 \quad (4.1)$$

In Figure 4.16 the result of the curve fitting together with the equations and the coefficient of determination $R^2$ is present. As shown by the higher coefficient of determination for the WTT configuration, the curve fitting has a better quality for this configuration. For the conventional configuration, for the intermediate $C_L$ values, the glide ratio values are not well represented by the curve fitting. Both curve fittings are very close to each other in the intermediate $C_L$ region, but the experimental glide ratio values are much lower for the conventional configuration.

Exactly the same drag polars are also present in Figure 4.17, As the only difference in the curve fitting between both configurations is the induced drag factor, the curve fitting is more affected by the points at the higher lift coefficient values. In this $C_L$ region, the conventional configuration starts to have a higher glide ratio, although it becomes higher than the glide ratio for the WTT configuration for the same $C_L$ values; the fitting is affected but does not show this glide ratio inversion.

The main objective of this work, is the comparison between both configurations, so the plot in Figure 4.15 is the most relevant one, as it shows that for intermediate $C_L$ values, the WTT configuration has clearly a higher glide ratio. Curve fitting these results is important to describe the drag of the airplane and to be used in other equations, as for the experimental thrust determination. Using an adequate drag polar and not only any polynomial equation, has the objective of describing the efficiency increase of the WTT configuration through a decrease in the induced drag factor, however, as the efficiency increase is not present for every $C_L$ value, especially at higher lift coefficients, the higher glide ratio values at intermediate lift coefficients is not well translated by the difference in the induced drag factor between both configurations.

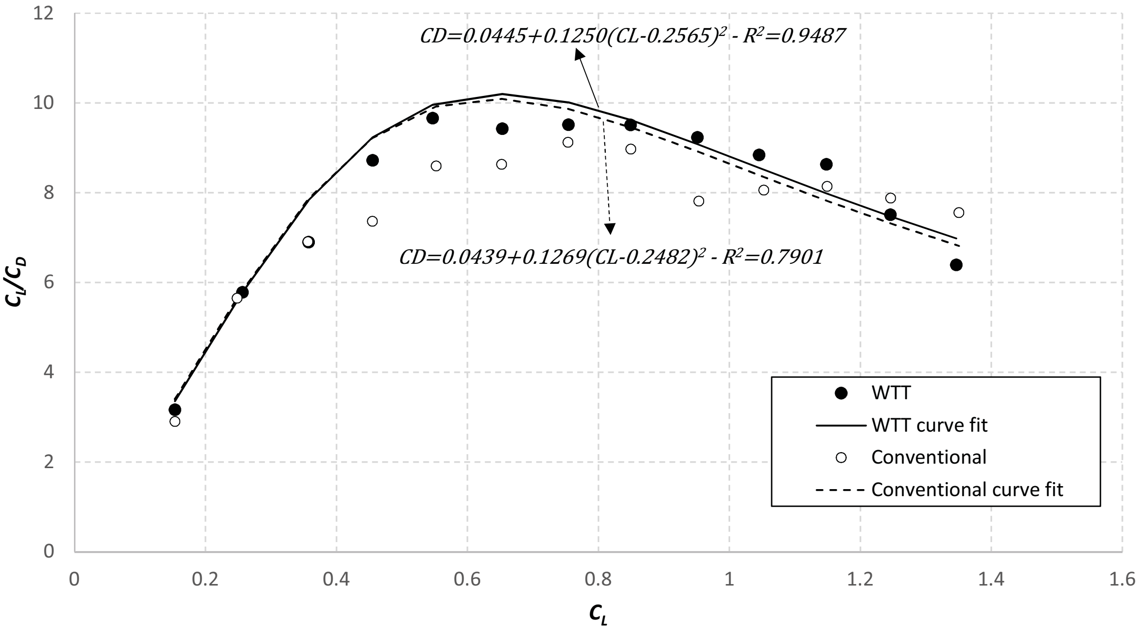

Figure 4.16: Asymmetrical drag polar curve fitting at the glide ratio values plot.

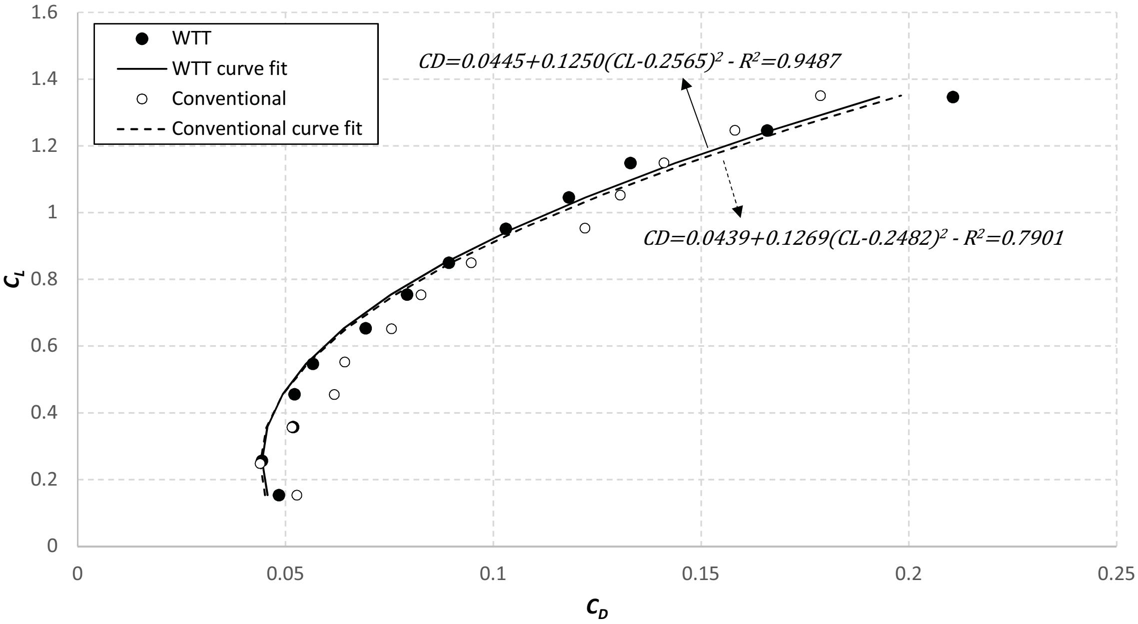

Figure 4.17: Asymmetrical drag polar curve fitting at the drag polar plot.

### 4.3.1 Numerical Results Comparison

These experimental results can be compared with the numerical ones, attention has to be paid, as the numerical results do not have a fuselage body and the simulations only reached a solution until a lift coefficient of 1.2.

As the numerical results are only for a wing and tail surfaces, the absolute glide ratio values will be higher than the ones obtained with the experimental flight testing. With this study, the most important conclusions should be the comparison between both curves. The plot in Figure 4.18 has the experimental and numerical glide ratio results represented together. From a lift coefficient of 0.45 until a lift coefficient of 0.8, the WTT configuration shows a higher glide ratio, towards the higher lift coefficients, the glide ratio is about the same for both configurations and at the end of the $C_L$ range, the numerical simulation predicts an inversion and the conventional configuration has a higher glide ratio than the WTT configuration. Again, without considering the absolute values, the experimental results have a similar behavior. Until $C_L = 0.45$ the average of the glide ratio values are about the same for both configurations. At the intermediate lift coefficient values, until a $C_L = 1.15$ the WTT configuration has always a higher average glide ratio value. From a lift coefficient of 1.2 until 1.4, the same inversion in the glide ratio value is observed and the conventional configuration as a higher glide ratio in this interval as in the numerical study.

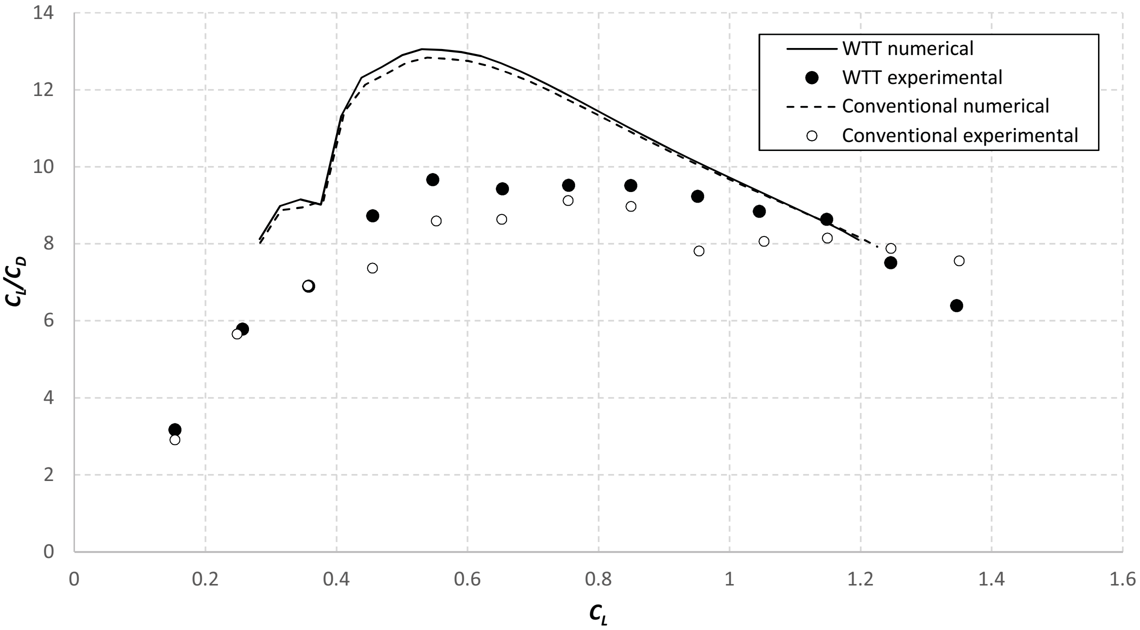

Figure 4.18: XFLR5 glide ratio values comparison with the experimental results for both configurations.

In Figure 4.19 the experimental and numerical results for the drag polar are also represented, for the lowest $C_L$ values. The difference between both configurations should be the parasite drag of the fuselage, tail booms and landing gear, however, this difference does not remain constant along the $C_L$ values. For the higher $C_L$ values, the experimental and numerical results are about the same, which indicates that the numerical results have a higher induced drag than the one experimentally determined. It is interesting that the numerical simulation predicted a drag spike for a $C_L$ between 0.3 and 0.4; it is less noticeable, but also the experimental results, especially for the WTT configuration show this spike at the same $C_L$ value.

In Figure 4.20 the estimated parasite drag coefficient for the fuselage and other components is represented. It is obtained by subtracting the numerical drag coefficient from the experimental drag coefficient. For the lowest $C_L$ values the estimation should be correct, the induced drag coefficient is approximately zero and the only difference is in the parasite drag. Along the $C_L$ values, the fuselage drag coefficient decreases until values of zero, once again, this show that the numerical induced drag coefficient is higher than the experimentally obtained induced drag coefficient. For the lowest $C_L$ values, both configurations have approximately the same parasite drag coefficient, with the WTT configuration having a slightly lower value. As the numerical induced drag coefficient is not the same as the experimental, the parasite drag is influenced and does not remain as constant as it should be.

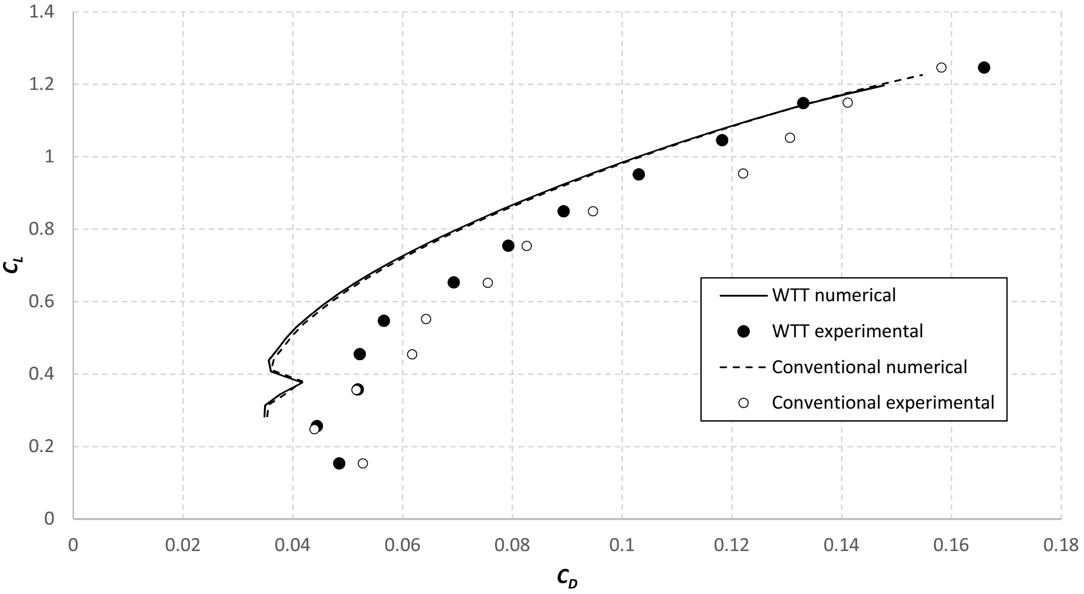

Figure 4.19: XFLR5 $C_L$ and $C_D$ values comparison with the experimental results for both configurations.

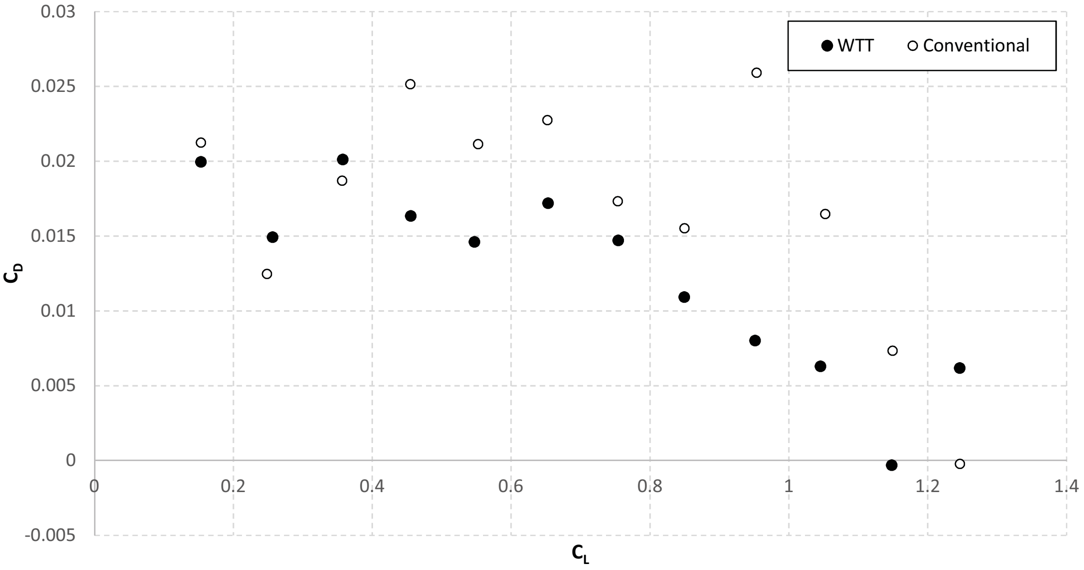

Figure 4.20: Estimated parasite drag coefficient for fuselage and other components for both configurations.

### 4.3.2 Erroneous Approach Result

One result about this methodology that is not described in the reviewed literature, is the difference between the glide ratio that is obtained with the average of the glide ratio values for each experimental point and the glide ratio that is obtained with the average of the lift coefficients divided by the average of the drag coefficients. As it is mentioned in Section 3.6, the data analysis should be performed considering the glide ratio of each point and not the drag coefficient values because that would lead to erroneous glide ratio values. In Figure 4.21 it is present the plot for the glide ratio values obtained from the average of the glide ratio for each point and the glide ratio calculated with the average of $C_L$ and $C_D$ for the group of points from each bin. For the higher $C_L/C_D$ values, the difference between both methodologies is about 15% and the values obtained with the average of the lift and drag coefficients are always lower than the values for the same configuration with the average of the glide ratio for each point.

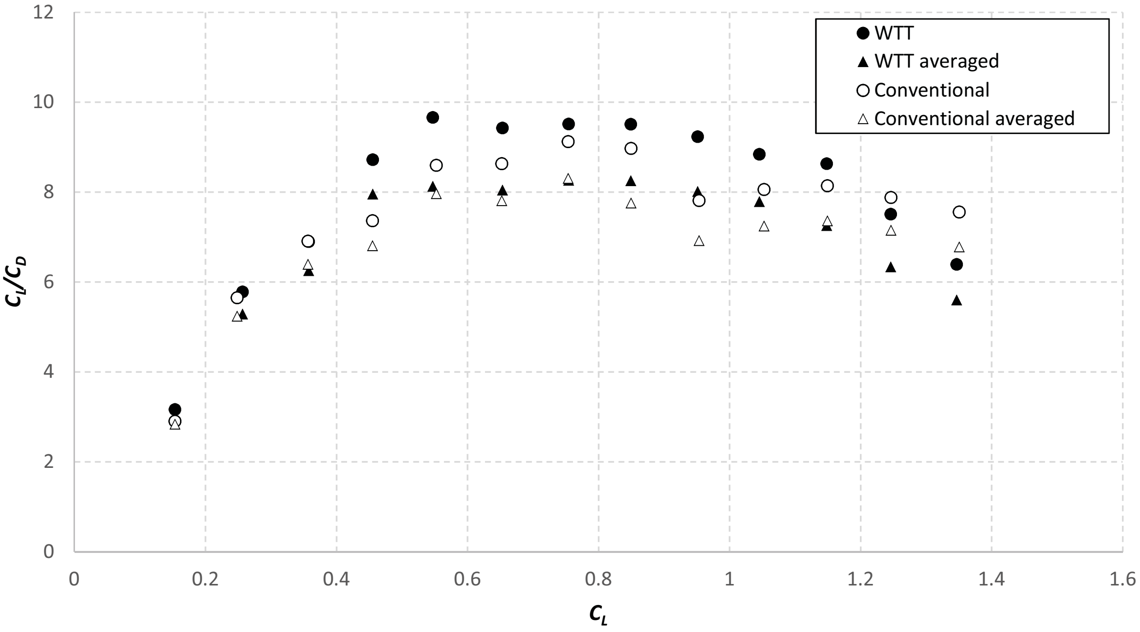

Figure 4.21: Comparison of the experimental glide ratio values with the ones (averaged) obtained with the erroneous approach.

## 4.4 Energy Method and Methodology Tests Results

Before comparing the presented methodology with the alternative ones, an effort to understand how the results are affected with the energy method, corrections and filtering are made. In Figure 4.22 the results for the energy method and without filtering with the respective dispersion curves is present. The effect is obvious, without the filtering, it results in negative drag coefficients values and the dispersion increases, the regression methodology to represent the standard deviation is not totally adequate, for example, for a $C_L$ between $0.6$ and $0.8$ there is a big increase in the dispersion that is not present in the regression.

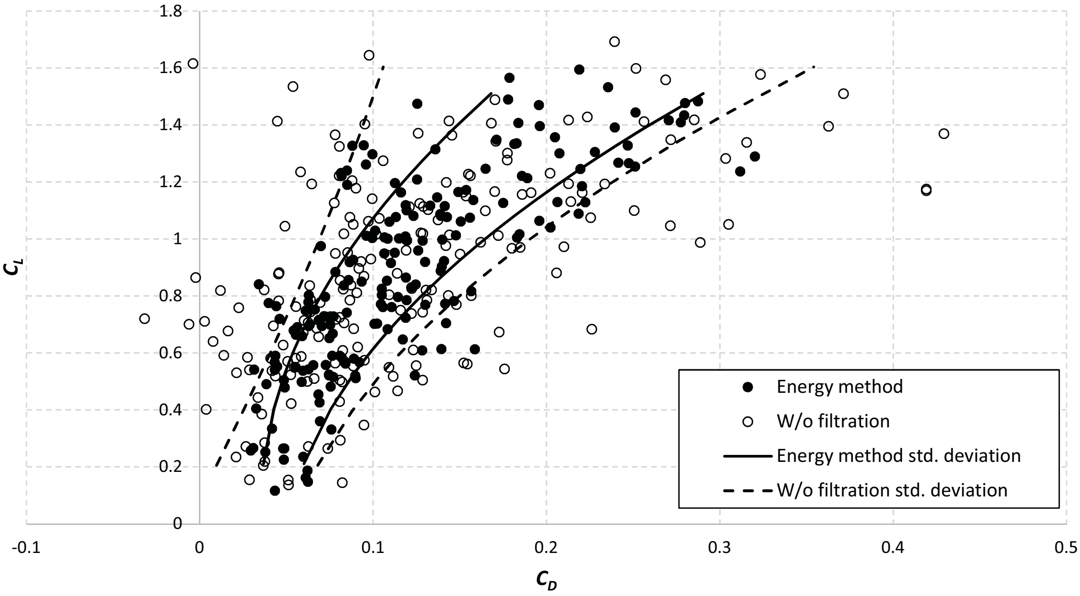

Figure 4.22: Results dispersion comparison between the energy method and the methodology without the filtration.

In Figure 4.23, the energy method is compared with the methodology with the constant speed assumption, considering that the speed change, that is the horizontal acceleration, is what characterizes the energy method, without this, the results are even worse than in the comparison before; there are more negative and lower drag coefficient points, in some regions the dispersion increases and for some regions the average changes its value, changing considerably the resulting drag polar.

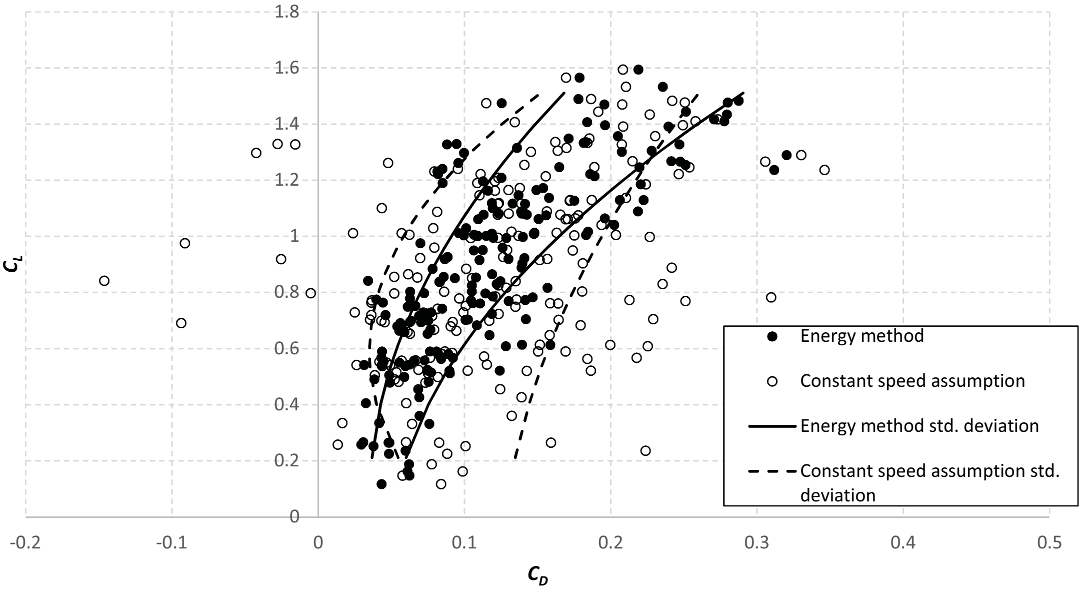

Figure 4.23: Results dispersion comparison between the energy method and the methodology with the constant speed assumption.

In Figure 4.24, the energy method is compared with the methodology without the lift correction. Attention to this plot has to be paid, the effect of this correction is only in the vertical axis, so the represented standard deviation curves are for the standard deviation of the lift coefficient in the vertical axis. Although the lift coefficients values are slightly changed, the dispersion does not increase considerably, it can be concluded that this correction has the least effect on the results. Although the standard deviation increases for lower and higher $C_L$ values, this correction is important to account for small accelerations that change the real lift coefficient value.

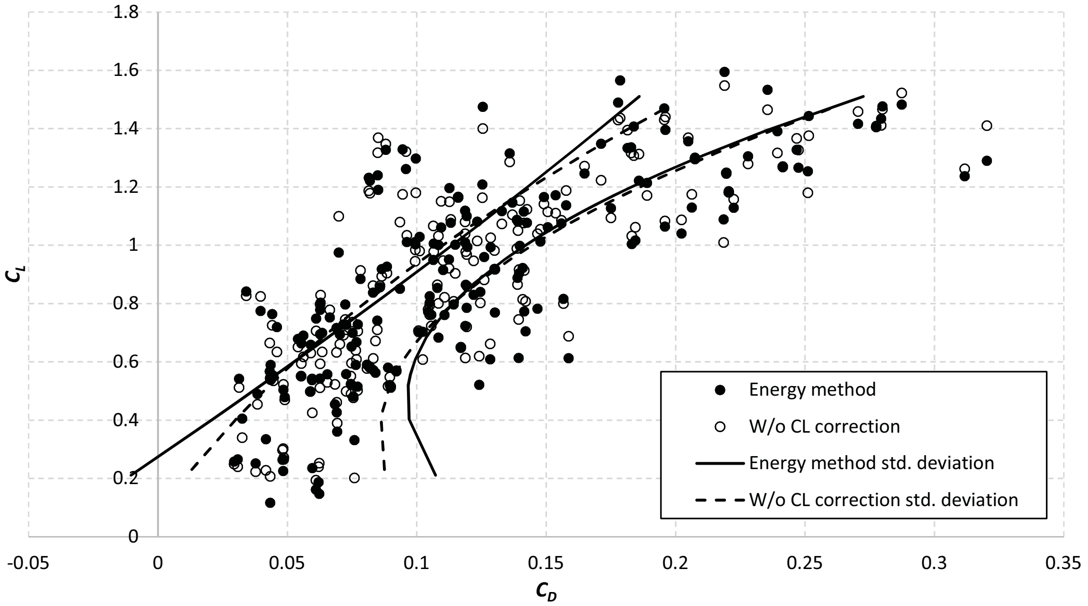

Figure 4.24: Results dispersion comparison between the energy method and the methodology without the lift coefficient correction.

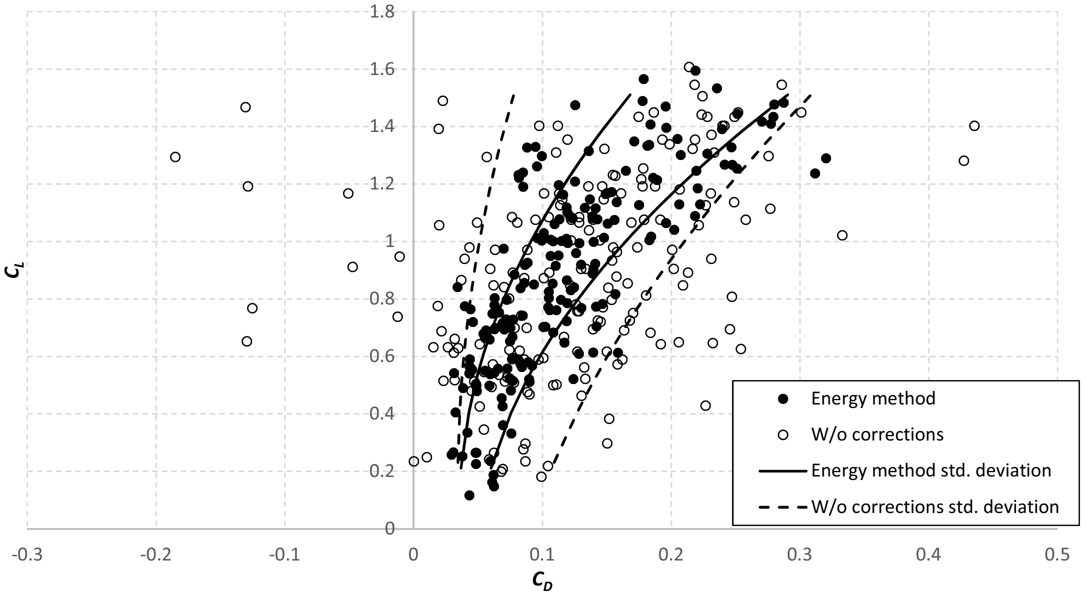

Figure 4.25: Results dispersion comparison between the energy method and the methodology without all the corrections.

In Figure 4.25, the effect of not using any of the corrections is represented. The resulting dispersion is not a sum of the dispersion of each correction, as some corrections affect the results in one way and others in the opposite way. Without all the corrections, the results have more dispersion than with the energy method, but in the same scale of the previous comparisons analyzed. Summing up, apart from the lift correction that does not have a considerably influence, all the other corrections decrease the dispersion in the results. The base of the energy method, the correction of changes in the velocity is the most important one. It can be seen that without all the corrections the standard deviation change is not constant for both the superior and inferior limit, the average values of the resultant experimental points are also changed without the corrections, changing considerably the experimentally obtained drag polar.

## 4.5 Alternative Methodologies Comparison

Comparing the experimental results obtained through the energy method and the alternative methodologies described in Section 3.4.1, is done through the plots in Figures 4.28 and 4.29. These plots are the comparison between the alternative methodologies and energy method, each for each configuration. The data for both the alternative methodologies, are the average of the bins division as done previously, the data that was the origin of this bins division, that is, the glide ratio for each glide analyzed, is present in Figures 4.26 and 4.27. In Figure 4.26 the result of the geometrical glide ratio alternative methodology for both configurations is present and in Figure 4.27 the result of the glide ratio from the glide angle alternative methodology for both configurations is present. The results between the methodologies are slightly different between the configurations, for both configurations at the lower $C_L$ values both the alternative methodologies under predict the glide ratio values, for the WTT configuration this trend continues along the $C_L$ and for the conventional configuration from a $C_L = 0.6$, all the methodologies result in similar glide ratio values.

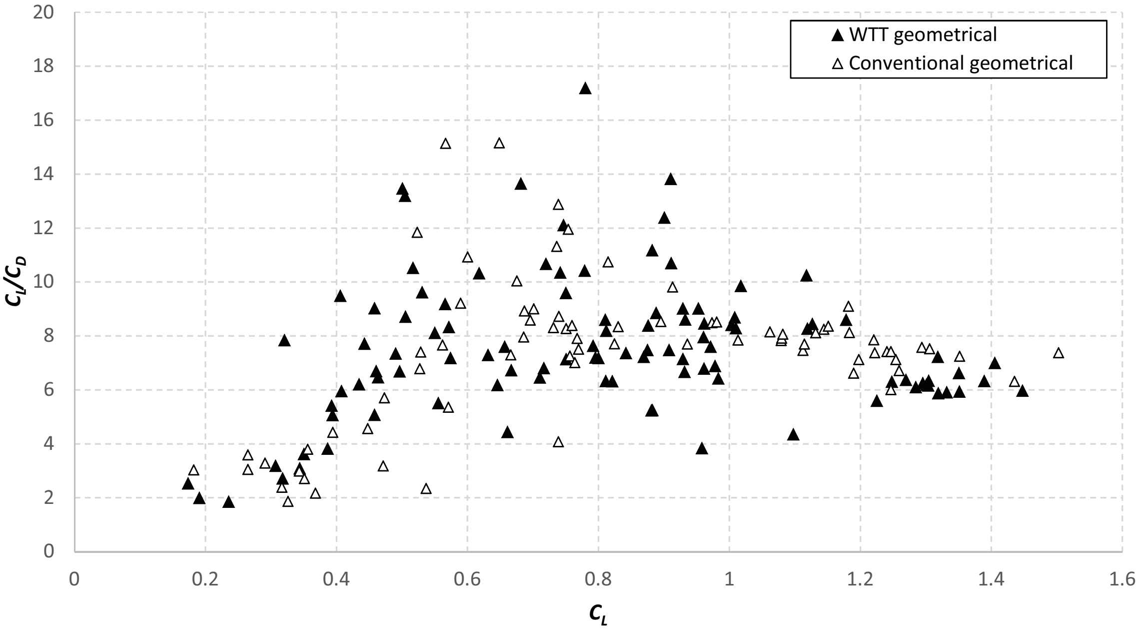

Figure 4.26: Comparison of the glide ratio values obtained with the glide angle methodology for both configurations.

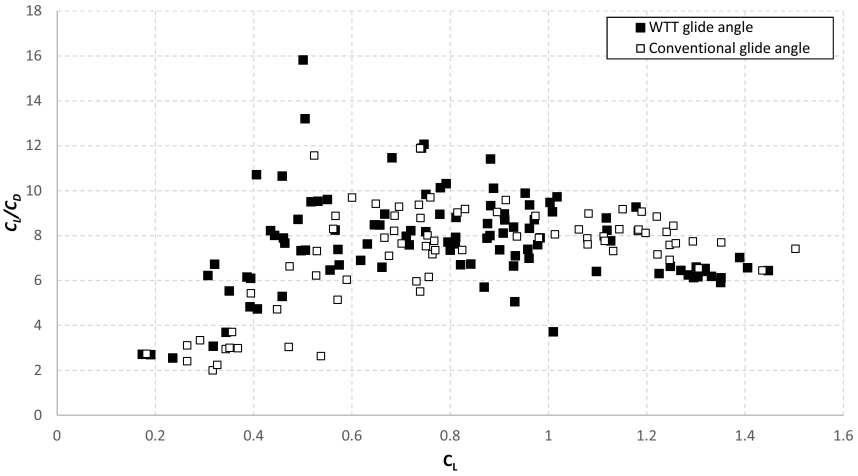

Figure 4.27: Comparison of the glide ratio values obtained with the geometrical methodology for both configurations.

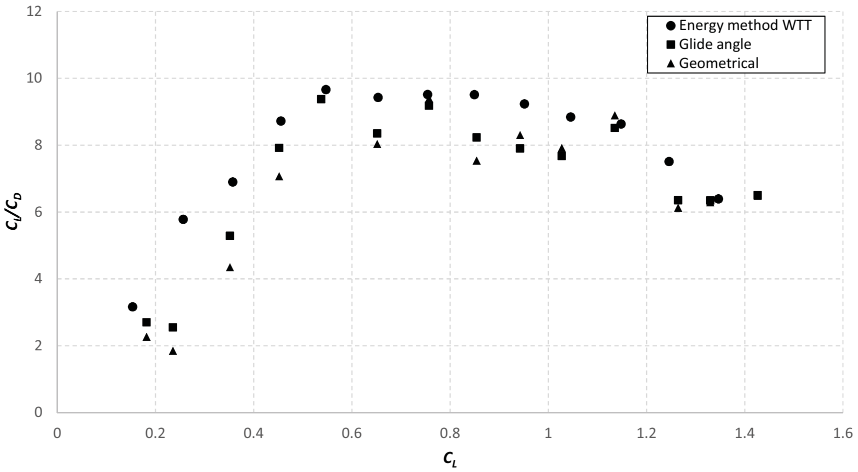

Figure 4.28: Comparison of the glide ratio average values between the energy method and the alternative methodologies for the WTT configuration.

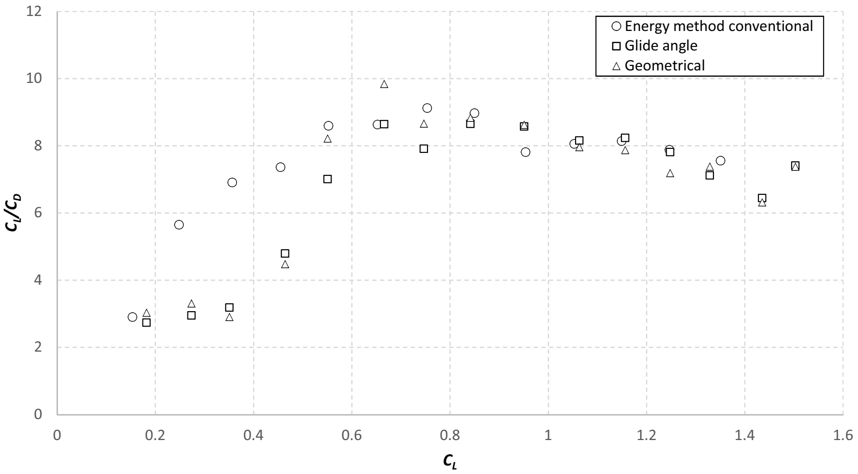

Figure 4.29: Comparison of the glide ratio average values between the energy method and the alternative methodologies for the conventional configuration.

## 4.6 Flight Testing Results - Climbs

The plot in Figure 4.30 is the result of the climb analysis, for both configurations, to determine the thrust curve of the propulsive system. As the propulsive system and its coupling to the airframe is the same for both configurations, as expected, the results for both configurations are about the same. The experimental thrust for both configurations is joined in only one group of data to describe the propulsive system and a linear regression is used in this joined data to obtain the thrust line. The stall speed of the aircraft is about $7.5m/s$. In this plot, there are data points at velocities lower than the stall speed, because, near the end of some climbs the airplane would end near or in a stall with a lot of angular velocity achieving, for an instant, velocities lower than the stall speed. These instantaneous low speed values will result in a higher estimated drag value and consequently increase the experimentally obtained thrust. To fit the results with a straight line, and obtain a realistic characterization of the propulsive thrust, only the thrust points above an airspeed of $7.5m/s$ should be considered. A linear regression is also applied to the same data set, considering only points with velocities higher than $10m/s$; this is the range of velocities where the airplane flew more and the data have a more linear behavior. The straight line for the velocities above $10m/s$ is the one chosen to best represent the propulsive system. This experimental thrust line is compared with already existing wind tunnel tests for this propulsive system combination. In Figure 4.31 the wind tunnel results of Zagreb [76] and Stuttgart [77] universities, the UBI's numerical result using the PROPSELECTOR software [78], and the regression line of the flight tests are represented.

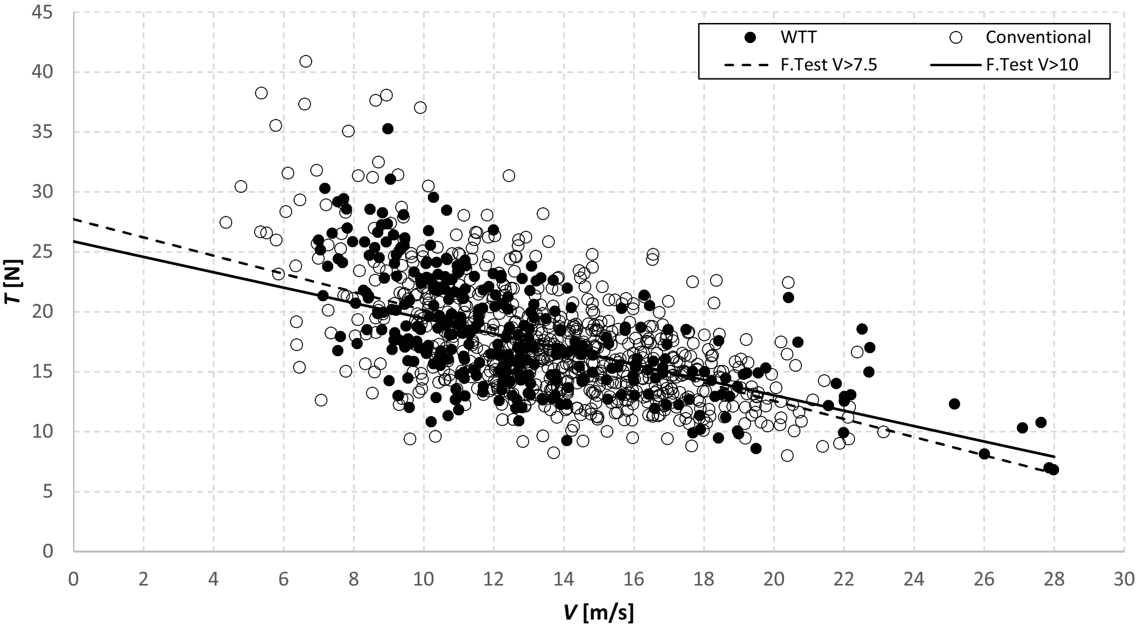

Figure 4.30: Experimental thrust against the velocity for both configurations with the linear regression for velocities above $7.5m/s$ and $10m/s$.

The thrust line obtained for velocities higher than $10m/s$, not only it has a more linear behavior, as there is not as much dispersion causing a high static thrust estimation as for the regression for velocities above $7.5m/s$. Comparing the ”F.Test V>10” line with the wind tunnel results from Zagreb, both have a similar static thrust value however the slope of thrust with the velocity is not as abrupt for Zagreb as the one obtained through the flight testing. Comparing with the Stuttgart wind tunnel test, the slope is similar, however, it appears that their result under predicted the real thrust for all the speed range. This should be expected as their tests were conducted with the electrical current limited to 42 $A$. During the flight tests, current values of 50 $A$ were achieved. Comparing with the PROPSELECTOR result from UBI, for velocities above $10m/s$ the thrust values are very close to one another. As the PROPSELECTOR result is not a straight line but a curve, for lower velocities the thrust is considerably lower when comparing to the flight tests results. Observing the differences between both wind tunnel tests for the same propulsive system and between the software prediction, the results from the flight testing, clearly show that this method is well suited to characterize the propulsive system, with the big advantage that, it does not require a large and expensive wind tunnel to obtain a reliable estimation of the propulsive thrust for a desired velocity range.

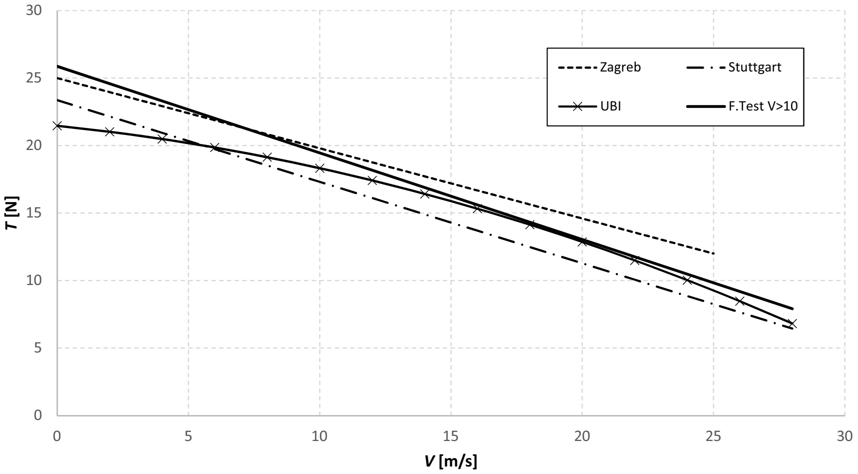

Figure 4.31: Thrust curves for the propulsive system from the experimental curve fit, UBI study, Zagreb study [76] and Stuttgart study [77].

With the measured electrical power and through the experimental thrust, it is possible to calculate the available power followed by the propulsive efficiency. In Figure 4.32, the propulsive efficiency for the systems used in these aircraft is represented. The maximum experimental propulsive efficiency is almost 60% for the higher velocities and around 40% for the lower velocities, these values are the expected ones for a propulsive system for UAVs of this size.

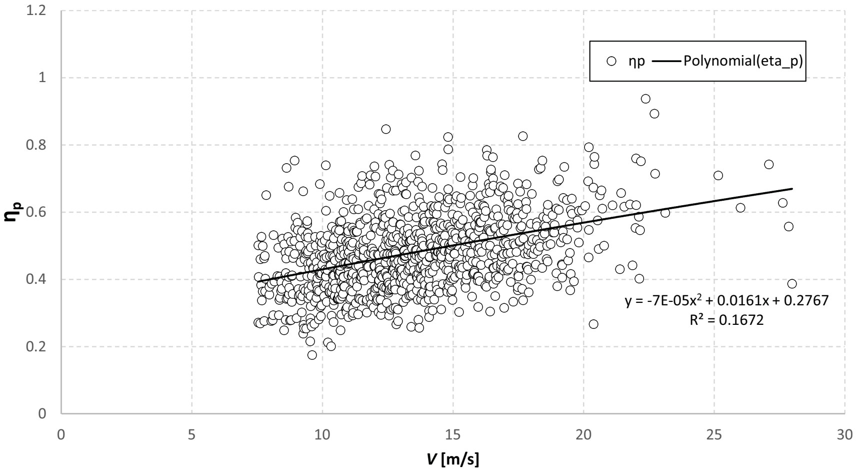

Figure 4.32: Experimental propulsive efficiency.

# Chapter 5

## WTT Configuration Parametric Study

Keeping in sight future developments of this configuration, an effort was made to increase the potential of this configuration recurring to this numerical study. First, small changes were tested, the tail surfaces are mounted $20mm$ above the trailing edge of the wing. Small changes in the vertical position, that is $20mm$ upward or downward, do not have a considerable effect in the glide ratio. Further changes from these points, the resultant glide ratio is decreased. Increasing the wing's incidence to small positive values and decreasing the tail surfaces incidence angle to small negative angles, result in a decrease of the glide ratio. To test bigger changes in the tail position, the flow around the wingtip, that is the vortex position, was observed to understand how the next changes should be done. From Figure 5.1, it is evident that the extended wingtips that were added to this configuration, push the vortex outboard and upward, increasing the distance between the vortex and the tail surfaces.

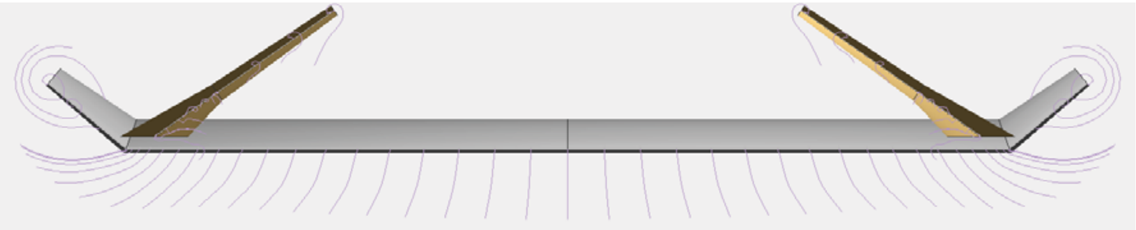

Figure 5.1: XFLR5 stream lines for the WTT configuration.

An obvious design change, would be placing the tail surfaces right behind the vortex, however, this would lead back to the 2003 design of the configuration, which had a dutch roll problem.

In the plot of Figure 5.2, a few different configurations are represented. The conventional baseline and original WTT configuration, lines with circle and triangle markers respectively, are still present. With a square marker, a configuration where the tail surfaces are further outboard, at $750mm$ of the $855mm$ semi wingspan with the dihedral angle inverted. With a diamond marker, a configuration that is close to the 2003 one and without markers, new configurations with the spanwise and wing distance changed. All these new configurations have a considerable higher glide ratio value than the baseline configuration, especially from a $C_L = 0.45$ value up to the higher $C_L$ values. The configuration represented by the dotted line has the tail surfaces at $720mm$ spanwise, comparing with the configuration that has a spanwise distance of $750mm$, large dash line. It is obvious that the result for the $720mm$ position is not real. By further increasing the spanwise distance to the $800mm$, for the same vertical position, the glide ratio starts to decrease. At the $800mm$ position, if the vertical distance is highly increased, up to $100mm$, the glide ratio increases, and the resultant configuration is similar to the 2003 configuration for the ACC competition. For the $750mm$ position, which is considered the most favorable configuration given the past experience, the tail distance from the wing was also changed. The tail moment arm was doubled and halved, accompanied by halving and doubling the tail surfaces, respectively, to keep the volume coefficients constant, Equations 3.1 and 3.2. For a tail position closer to the wing, the glide ratio was decreased and for the doubled distance, as present in the Figure 5.2, the glide ratio increases slightly.

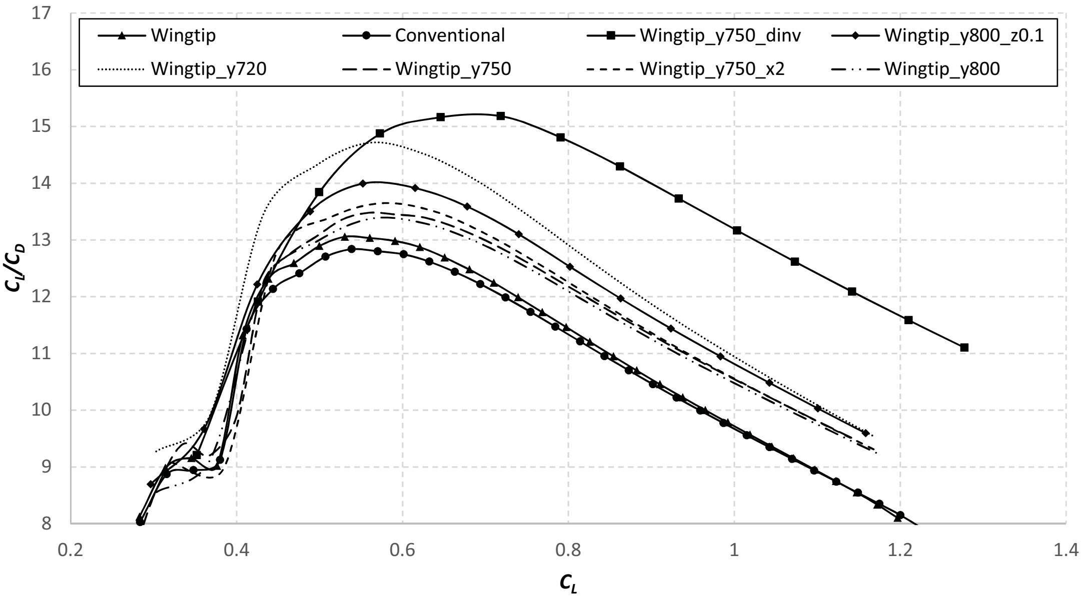

Figure 5.2: XFLR5 configuration optimization.

Even excluding the configuration similar to the 2003 one, undoubtedly that the configuration with the inverted tail dihedral angle has the best glide ratio and higher efficiency increase from the conventional configuration. However, with this change, this configuration has not anymore the same aerodynamic concept of this study. The tail surface is in the wings' vortex path, but in the wings' upwash, the increase in the glide ratio comes not only from the drag decrease, but also from an increase in the total airplane lift. The tail surfaces have now a local positive angle of attack, producing lift instead of downforce, as in an outboard horizontal stabilizers configuration. More than increasing the glide ratio, this configuration also increases the longitudinal static stability, but with the negative (nose down) pitching moment, that is created by the tail, it becomes extremely difficult to achieve a zero pitching moment value with a conventional center of gravity position.

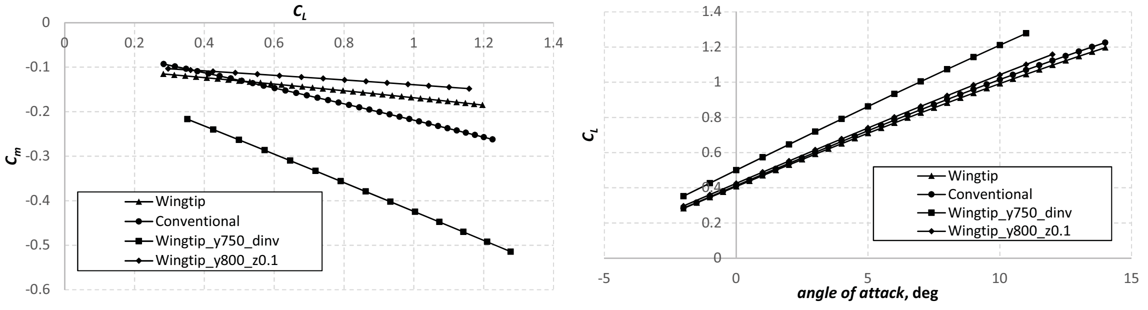

Figure 5.3: XFLR5 curves for $C_L$ and $C_m$.

The lift coefficient and pitching moment curves for the conventional, WTT configuration, the configuration similar to the 2003 one and the inverted dihedral angle (similar to an OHS configuration), are present in Figure 5.3. From the pitching moment coefficient plot, it can be concluded that neither configuration has a zero pitching moment coefficient value, that is, a trimmed point to fly, even with elevator or deflecting the entire surface. However, both the conventional and WTT configurations were successfully flown with a stable flying point over a wide $C_L$ range. This is seen as another limitation in the software used to obtain the numerical results, the XFLR5 software.

# Chapter 6

# Conclusions

## 6.1 Achievements

The concept WTT configuration that uses the wingtip vortices to generate a forward force and decreases the induced drag, was successfully and extensively flown across the entire flight envelope, gathering flight data and experience with this non-conventional airplane configuration.

Several flight tests were conducted with this configuration and with a baseline conventional configuration. The flight testing methodology, based in the energy of the airplane and in the changes between the potential and kinetic energy, allowed not only the characterization of the drag polar of both aircraft, but also the characterization of the propulsive system without other facilities as wind tunnels.

Through the flight testing of both configurations, it was confirmed the efficiency increase of the WTT configuration for the intermediate range of lift coefficient values, as was also expected from the numerical analysis with the XFLR5 software.

A low weight, small and low cost data acquisition equipment, based in the open source microcontroller Arduino, was developed. The system proved its capability to gather the flight data and its reliability, working flawlessly during the flight testing campaign.

## 6.2 Future Work

As already discussed throughout the document, there are some limitations and possible improvements to the work. This thesis focused not only in completing the initial objectives, but also in leaving already a few ways to improve the flight testing of aircraft and improve this new configuration.

Concerning the WTT configuration:

- The presented work in Chapter 5, includes a series of different tail options for the studied aircraft with a higher efficiency increase than the one used in the present study. Exactly the same airplane, might be modified and the entire study repeated, this time having already these results as a comparison;

- Develop this concept through CFD simulations, optimize a new aircraft with this tail configuration, and repeat the flight tests to document a substantial efficiency increase from this innovative concept and tail configuration.

Concerning the flight testing:

- As stated with the uncertainty analysis, the major uncertainty and results dispersion comes from the airspeed sensor. Changing the current analog sensor for the more precise digital one ([75]), should be done before carrying more flight tests with the developed data acquisition equipment;
- Developing a library to communicate with the GPS module, brings the possibility to improve the data acquisition equipment in several ways, it would allow a higher data rate and, if the developed library uses less memory, which is possible by removing some functions that are not crucial, the microcontroller board could be changed by a lighter, smaller and cheaper one.

# Bibliography

[1] S. F. Hoerner, *Fluid Dynamic Drag*, 1965. 5, 8, 13, 14

[2] How to calculate drag on an airfoil from momentum equation. Last visited at: 8th May 2018. [Online]. Available: https://aviation.stackexchange.com/questions/40858/how-to-calculate-the-drag-on-an-airfoil-from-momentum-equation-fundamental-of-a 5

[3] D. P. Raymer, *Aircraft Design: A Conceptual Approach*. American Institute of Aeronautics and Astronautics, Inc., 1992. 7, 37

[4] J. D. Anderson, *Fundamentals of Aerodynamics*. McGraw-Hill, Inc., 2011. 7, 11

[5] J. Katz and A. Plotkin, *Low-Speed Aerodynamics: From Wing Theory to Panel Methods*. McGraw-Hill, Inc., 1991. 8, 31

[6] R. E. Mineck, K. W. Mortara, D. M. Straussfogel, and M. D. Maughmer, "Analysis and Design of Planar and Non-Planar Wings for Induced Drag Minimization," Tech. Rep. NASA CR-191274, 1992. 8

[7] U. La Roche and S. Palffy, "Wing-Grid, a Novel Device for Reduction of Induced Drag on Wings," in *AIAA\ICAS International Air and Space Symposium and Exposition*, 1996, pp. 2303–2309. 9, 17, 18

[8] M. Munk, "Elements of the Wing Section Theory and of the Wing Theory," National Advisory Committee for Aeronautics, Tech. Rep. NACA No. 191, 1925. 9, 14

[9] I. Kroo, "Drag Due To Lift: Concepts for Prediction and Reduction," *Annual Review of Fluid Mechanics*, no. 33, pp. 587–617, 2001. 10, 15, 16

[10] S. C. Smith and I. M. Kroo, "Computation of Induced Drag for Elliptical and Crescent-Shaped Wings," *Journal of Aircraft*, vol. 30, no. 4, pp. 446–452, 1993. 10, 14, 15

[11] J. D. Anderson, *Aircraft Performance and Design*. McGraw-Hill, Inc., 1999. 12, 21

[12] J. E. Yates and C. Donaldson, "A Fundamental Study of Drag and an Assessment of Conventional Drag-Due-to-Lift Reduction Devices," Tech. Rep. NASA CR-4004, 1986. 12

[13] S. Hoerner, "Aerodynamic Shape of the Wing Tips," Wright-Patterson Air Force Base, Tech. Rep. AF Technical Report 5752, 1949. 13

[14] B. E. Tinling and W. R. Kolk, "The Effects of Centrally Mounted Wing-Tip Tanks on the Subsonic Aerodynamic Characteristics of a Wing of Aspect Ratio 10 with 35° of Sweepback," Tech. Rep. NASA RM-A50K15, 1951. 14

[15] C. VanDam, "Induced-Drag Characteristics of Crescent-Moon-Shaped Wings," *Journal of Aircraft*, vol. 24, no. 2, pp. 115–119, 1987. 14

[16] M. V. Lowson, "Minimum Induced Drag for Wings with Spanwise Camber," *Journal of Aircraft*, vol. 27, no. 7, pp. 627–631, 1990. 15

[17] H. Zimmer, "The Aerodynamic Optimization of Wings at Subsonic Speeds and the Influence of Wingtip Design," Tech. Rep. NASA TM-88534, 1987. 15, 16, 17

[18] P. S. Kirk and R. Whitcomb, “System for Increasing Airplane Fuel Mileage and Airplane Wing Modification Kit,” 1995, uS005407153A. 15

[19] J. E. Hackett, “Vortex Diffuser,” 1980, united States, 4190219. 15

[20] C. D. Cone, “The Theory of Induced Lift and Minimum Induced Drag of Nonplanar Lifting Systems,” Tech. Rep. NASA TR-R-139, 1962. 16, 17

[21] J. J. Spillman, “The Use of Wing Tip Sails to Reduce Vortex Drag,” *Aeronautical Journal*, no. 618, pp. 387–395, 1978. 16

[22] L. L. Herrick, B. Bays-Muchmore, M. S. Hoffman, L. LeGrand, S. S. Ogg, B. P. J. Paul, K. D. Visser, and S. L. Wells, “Blunt-Leading-Edge Raked Wingtips,” 2000, uS006089502A. 17

[23] J. F. Halpert, D. H. Prescott, T. R. Yechout, and M. Arndt, “Aerodynamic Optimization and Evaluation of KC-135R Winglets , Raked Wingtips , and a Wingspan Extension,” *AIAA Journal*, vol. 48, no. January, p. 2010, 2010. 17

[24] L. B. Gratzer, “Spiroid-Tipped Wing,” 1992, uS005102068. 17

[25] K. G. Heffernan, “Trailing Vortex Attenuation Devices,” Master’s Thesis, Naval Postgraduate School Monterey, California, 1985. 18

[26] H. D. Céron-Muñoz, R. Cosin, R. F. F. Coimbra, L. G. N. Correa, and F. M. Catalano, “Experimental Investigation of Wing-Tip Devices on the Reduction of Induced Drag,” *Journal of Aircraft*, vol. 50, no. 2, pp. 441–449, 2013. 18, 19

[27] J. C. J. Patterson and G. R. Bartlett, “Evaluation of Installed Performance of a Wing-Tip-Mounted Pusher Turboprop on a Semispan Wing,” Tech. Rep. NASA TP-2739, 1987. 18, 19

[28] J. A. Kentfield, “Aircraft with outboard horizontal stabilizers, history, current status, development potential,” *Progress in Aerospace Sciences*, vol. 45, no. 6-8, pp. 169–202, 2009. 19

[29] J. W. McGinnis, “Efficient Control and Stall Prevention in Advanced Configuration Aircraft,” 2015, uS20150048215. 19, 20

[30] J. A. Kentfield, “Upwash Flowfields at the Tails of Aircraft with Outboard Horizontal Stabilizers,” *AIAA*, vol. 98, no. 0757, pp. 1–10, 1998. 19

[31] A. H. Bowers, O. J. Murillo, R. R. Jensen, B. Eslinger, and C. Gelzer, “On Wings of the Minimum Induced Drag : Spanload Implications for Aircraft and Birds,” Tech. Rep. NASA/TP-2016-219072, 2016. 20

[32] Flying Wing-Shaped Experimental Airplane Validating New Wing Design Method. Last visited at: 13th March 2018. [Online]. Available: https://www.nasa.gov/centers/armstrong/features/Prandtl-D{_}validating{_}new{_}wing{_}design.html 21

[33] R. D. Kimberlin, *Flight testing of fixed-wing aircraft*. American Institute of Aeronautics and Astronautics, Inc., 2003. 21, 25

[34] E. S. Rutowski, “Energy Approach to the General Aircraft Performance Problem,” *Journal of the Aeronautical Sciences*, vol. 21, no. 3, pp. 187–195, 1954. 25

[35] J. R. Chambers, *Modeling flight: the role of dynamically scaled free-flight models in support of NASA’s aerospace programs*, 2010. 26

[36] G. D. Budd, R. L. Gilman, and D. Eichstedt, “Operational and Research Aspects of a Radio Controlled Model Flight Test Program,” Tech. Rep. NASA TM-104266, 1993. 27

[37] W. Williams and M. Harris, “The Challenges of Flight-Testing Unmanned Air Vehicles,” *Systems Engineering, Test & Evaluation Conference*, 2002. 27, 45

[38] M. W. Green, “Determination of the Lift And Drag Characteristics of an Airplane in Flight,” Tech. Rep. NACA No. 223, 1925. 27

[39] F. M. A. Silva and P. H. I. A. Oliveira, “Development of a Data Acquisition System for Light Airplanes Flight Tests,” in *18th International Congress of Mechanical Engineering*, 2005. 27

[40] A. G. DeAnda, “Standard Airspeed Calibration Procedures,” Edwards AFB, California, Tech. Rep. Air Force Flight Test Center-TIH-81-5, 1981. 28

[41] R. D. Kimberlin and J. P. Sims, “Airspeed Calibration Using GPS,” in *6th AIAA Biennial Flight Test Conference*, Hilton Head Island, SC, 1992. 28

[42] R. T. Marshall and W. G. Schweikhard, “Modeling of Airplane Performance from Flight-Test Results and Validation with an F-104G Airplane,” Tech. Rep. NASA TN D-7137, 1973. 28

[43] J. Norris and A. B. Bauerf, “Zero-Thrust Glide Testing for Drag and Propulsive Efficiency of Propeller Aircraft,” *Journal of Aircraft*, vol. 30, no. 4, pp. 505–511, 1993. 28

[44] T. M. Foster and W. J. Bowman, “Dynamic Stability and Handling Qualities of Small Unmanned-Aerial-Vehicles,” in *43rd AIAA Aerospace Sciences Meeting and Exhibit*, 2005, pp. 1–12. 28

[45] U.-l. Ly and S.-i. Higashino, “Development of a UAV Flight-Test Vehicle at the University of Washington,” in *2nd AIAA ”Unmanned Unlimited” Systems, Technologies, and Operations — Aerospace*, San Diego, California, 2003, pp. 1–13. 28

[46] M. Ramšak, “Radio Controlled Sailplane Flight: Experimental and Numerical Analysis,” *Strojniski Vestnik/Journal of Mechanical Engineering*, vol. 58, no. 3, pp. 147–155, 2012. 29

[47] B. S. Hiller, “Estimation of Drag Characteristics of a Fixed Wing Unmanned Aerial Vehicle,” in *AIAA’s 1st Technical Conference and Workshop on Unmanned Aerospace Vehicles*, Portsmouth, Virginia, 2002, pp. 1–5. 29

[48] W.-j. Jin and Y.-g. Lee, “In-Flight and Numerical Drag Prediction of a Small Electric Aerial Vehicle,” in *Proceeding of the 2011 Korean Society for Aeronautical & Space Sciences (KSAS) Spring Conference*, 2015, pp. 51–56. 29, 42

[49] J. N. Ostler, W. J. Bowman, D. O. Snyder, and T. W. McLain, “Performance Flight Testing of Small Electric Powered Unmanned Aerial Vehicles,” *International Journal of Micro Air Vehicles*, vol. 1, no. 3, pp. 155–171, 2009. 29, 42, 69

[50] Xflr5: Analysis tool for airfoils, wings and planes operating at low reynolds numbers. Last visited at: 5th February 2018. [Online]. Available: http://www.xflr5.com/xflr5.htm 31

[51] M. Drela. XFOIL: Subsonic Airfoil Development System. Last visited at: 24th April 2018. [Online]. Available: http://web.mit.edu/drela/Public/web/xfoil/ 31

[52] XFLR5, "Software Documentation: Analysis of foils and wings operating at low Reynolds numbers," Tech. Rep., 2013. 31

[53] B. Maskew, "A Quadrilateral Vortex Method Applied to Configurations with High Circulation," Tech. Rep. NASA N76-28173, 1976. 31

[54] A. C. Challenge, "Requirements, Rules and Evaluation for the Air Cargo Challenge 2017," 2016. 33

[55] Axi Gold electric motor specifications. Last visited at: 16th March 2018. [Online]. Available: https://www.modelmotors.cz/product/detail/231/ 34

[56] Castle Creations ESC specifications. Last visited at: 16th March 2018. [Online]. Available: http://www.castlecreations.com/en/phoenix-edge-lite-100-esc-010-0111-00 34

[57] SLS APL battery specifications. Last visited at: 23rd March 2018. [Online]. Available: https://www.stefansliposhop.de/en/Batteries/SLS-Multirotor-high-Capacity/SLS-APL/SLS-APL-10000mAh-3S1P-11-1V-25C-40C::1095.html 34

[58] Basher battery specifications. Last visited at: 23rd March 2018. [Online]. Available: https://hobbyking.com/en_us/basher-4000mah-6s-65c-hardcase-pack.html?___store=en_us 34

[59] APC propeller specifications. Last visited at: 23rd March 2018. [Online]. Available: https://www.apcprop.com/product/13x7/ 34

[60] Arduino mega specifications. Last visited at: 23rd March 2018. [Online]. Available: https://store.arduino.cc/arduino-mega-2560-rev3 46, 47

[61] Arduino mega. Last visited at: 08th May 2018. [Online]. Available: https://www.indiamart.com/proddetail/arduino-mega-2560-with-usb-cable-14768163197.html 47

[62] Adafruit GPS specifications. Last visited at: 23rd March 2018. [Online]. Available: https://www.adafruit.com/product/746 47, 48

[63] BMP180 pressure sensor datasheet. Last visited at: 23rd March 2018. [Online]. Available: https://cdn-shop.adafruit.com/datasheets/BST-BMP180-DS000-09.pdf 48

[64] BMP 180 pressure sensor. Last visited at: 08th May 2018. [Online]. Available: http://bdspeedytech.com/index.php?route=product/product&product_id=2314 48

[65] MPXV7002 differential pressure sensor datasheet. Last visited at: 23rd March 2018. [Online]. Available: https://www.nxp.com/docs/en/data-sheet/MPXV7002.pdf 48, 49, 62

[66] MPXV7002dp differential pressure sensor. Last visited at: 08th May 2018. [Online]. Available: https://www.openimpulse.com/blog/products-page/product-category/mpxv7002dp-pressure-sensor-module/ 49

[67] ACS770 current sensor datasheet. Last visited at: 23rd March 2018. [Online]. Available: goo.gl/AtKHVH 49, 50

[68] ACS770 current sensor. Last visited at: 08th May 2018. [Online]. Available: goo.gl/Z3M4Ry 50

[69] SC card read-writer information. Last visited at: 23rd March 2018. [Online]. Available: http://henrysbench.capnfatz.com/henrys-bench/arduino-output-devices/arduino-lc-studio-sd-card-tutorial/ 50

[70] Level shifter datasheet. Last visited at: 23rd March 2018. [Online]. Available: https://www.nxp.com/docs/en/data-sheet/74HC4050.pdf 50

[71] Level shifter. Last visited at: 08th May 2018. [Online]. Available: https://uk.rs-online.com/web/p/buffer-line-driver-combinations/4836544/ 51

[72] Introduction to Theoretical Computer Science — Boaz Barak. Last visited at: 08th May 2018. [Online]. Available: http://www.introtcs.org/public/lec_15_probability.html 56

[73] W. J. Devenport and A. Borgoltz. Basic Concepts in Experiments. Last visited at: 21st July 2018. [Online]. Available: http://www.dept.aoe.vt.edu/~aborgolt/aoe3054/manual/ch2/index.html 59

[74] Ardupilot: Using an Airspeed Sensor. Last visited at: 09th May 2018. [Online]. Available: http://ardupilot.org/plane/docs/airspeed.html 62

[75] Digital differential pressure sensor datasheet. Last visited at: 30th April 2018. [Online]. Available: goo.gl/BmR7di 62, 86

[76] J. Andrašec, M. Balaško, J. Čulina, and I. Knezović, “Projekt letjelice HUSZ Tern,” Fakultet Strojarstva i Brodogradnje, Tech. Rep., 2016. 79, 80

[77] A. Stuttgart, “Air Cargo Challenge 2013 Project Report,” 2013. 79, 80

[78] Propeller selector software. Last visited at: 09th May 2018. [Online]. Available: http://www.hoppenbrouwer-home.nl/ikarus/software/propselector.htm 79

# Appendix A

# Appendix

Figure A.1: Wing tip tail tube before the creation of the interface.

Figure A.2: Tail surface tube with female interface and 3D printed clamp for wing attachment.

Figure A.3: Wing tip tail tube with hard point to receive the tail surface clamp.

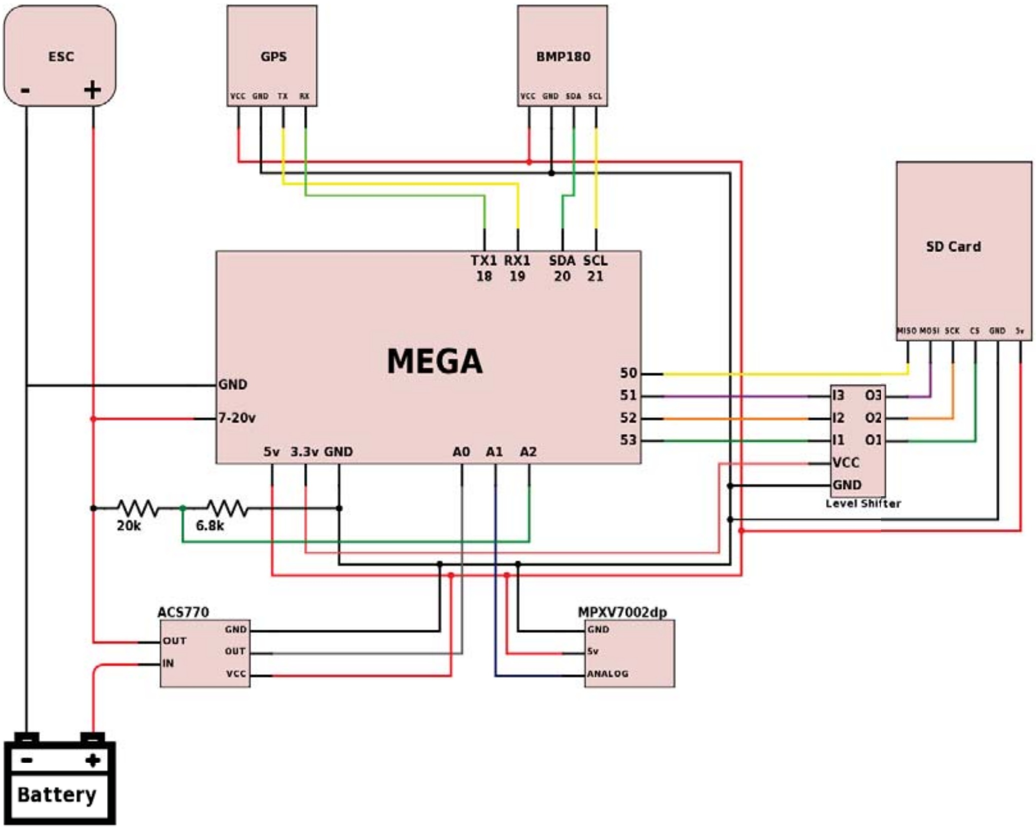

Figure A.4: Data Acquisition System Schematic.